THE HONG KONG
POLYTECHNIC UNIVERSITY
香港理工大學
Pao Yue-kong Library
包玉剛圖書館

Copyright Undertaking

This thesis is protected by copyright, with all rights reserved.

By reading and using the thesis, the reader understands and agrees to the following terms:

1. The reader will abide by the rules and legal ordinances governing copyright regarding the use of the thesis.
2. The reader will use the thesis for the purpose of research or private study only and not for distribution or further reproduction or any other purpose.
3. The reader agrees to indemnify and hold the University harmless from and against any loss, damage, cost, liability or expenses arising from copyright infringement or unauthorized usage.

IMPORTANT

If you have reasons to believe that any materials in this thesis are deemed not suitable to be distributed in this form, or a copyright owner having difficulty with the material being included in our database, please contact lbsys@polyu.edu.hk providing details. The Library will look into your claim and consider taking remedial action upon receipt of the written requests.

Pao Yue-kong Library, The Hong Kong Polytechnic University, Hung Hom, Kowloon, Hong Kong

http://www.lib.polyu.edu.hk

NUMERICAL METHODS FOR TOPOLOGY OPTIMIZATION OF ELECTROMAGNETIC DEVICES

YANG WENJIA

PhD

The Hong Kong Polytechnic University

2021

The Hong Kong Polytechnic University
Department of Electrical Engineering

Numerical Methods for Topology Optimization of Electromagnetic Devices

Yang Wenjia

A thesis submitted in partial fulfillment of the requirements for the degree of Doctor of Philosophy

March 2021

CERTIFICATE OF ORIGINALITY

I hereby declare that this thesis is my own work and that, to the best of my knowledge and belief, it reproduces no material previously published or written, nor material that has been accepted for the award of any other degree or diploma, except where due acknowledgement has been made in the text.

Name: YANG Wenjia

Dated: 01/05/2021

Abstract of dissertation entitled:

Numerical Methods for Topology Optimization of Electromagnetic Devices

submitted

by YANG Wenjia

for the degree of Doctor of Philosophy in

Electrical Engineering

at The Hong Kong Polytechnic University in (05/2021)

Abstract

Topology optimization of a device is the process of determining the material distribution within the device. Compared with the conventional shape and seize optimizations, topology optimization offers more degrees of freedom, and has the potential to produce more possible and promising designs but with a cost of a longer optimization time. Based on the requirement of the design and the nature of the problems involved, different topology optimization algorithms have been developed and applied in fellow disciplines. In the area of electromagnetic device designs, the development of applicable methods and strategies for topology optimization is still very demanding, and topology optimization remains a difficult and challenging problem due to the inherent complex natures of an electromagnetic inverse problem in terms of the geometry and involved multiple types of materials. In this respect, some typical problems and challenges encountered in a topology optimization process of electromagnetic device designs are addressed in this thesis.

To deal with the uncertainties in the engineering manufacturing of a device, a direct search methodology for robust topology optimizations is developed based on the quantum evolutionary algorithm, and numerically proved to be efficient when compared with other conventional robust optimizers, such as robust oriented genetic algorithms. Via using a quantum bit or *Q*-bit to represent the design parameters and an adaptive incremental angle for updating positions, the proposed algorithm is able to extensively exploit the neighbor of the searched space. Via using the stochastic

approximation method to compute gradient information, the proposed algorithm realizes computational savings of *n* (the dimension seize) times, and hence is able to be developed into an extremely fast convergent algorithm. Followed by the development of the algorithm, an engineering robust optimization problem related to the *RLC* ratio of a metamaterial unit cell for wireless power transmission efficiency enhancement is investigated. As the robustness and the averaged transmission efficiency are two distinctive objectives in this case study, a two-step or phase algorithm is further developed for the corresponding robust multi-objective optimization. At the first phase, the performance of different unit cells is evaluated separately, and at the second stage a regression model is constructed to replace the finite element analysis to reduce the computational time. The best candidate thus would be the one having a balance performance with a strong robustness and a high-power transmission enhancement.

To combat the extremely computationally expensive problem of a topology optimization procedure, a design-of-experiment (DOE) assisted surrogate model for an improved TABU search based refinement optimal method is introduced. By using the Latin-Hypercube sampling scheme to sample the design space, a Kriging model to interpolate the objective function, and a multi-start technique to reduce the design space; the proposed method is able to accurately predict the objective function of the optimization problem with a much shorter computational time, when compared to that of the conventional finite element method. The proposed algorithm is further investigated and applied to the design optimization of the metamaterial slab in wireless power transmission applications to develop an automatic optimization procedure for a hybrid metamaterial slab. The numerical simulation results agree well with the experimental ones, indicating the accuracy of the proposed algorithm. As a topology optimization problem in electromagnetic applications often contains multiple requirements and objectives, a vector wind driven optimization algorithm for multi-objective topology optimizations is also developed. By removing the inertia terms and adding an adaptive mutation term to the position updating equations, the proposed algorithm can extensively explore the entire design domain; and rather than using the

non-dominance method, the proposed method employs a gauging metrics to measure the improvement/reduction of various objective functions for every candidate and chooses the most effective one as the optimum. Numerical results indicate that the proposed algorithm has a faster converge rate when compared with the multi-objective counterparts of the conventional heuristic methods.

To address the multi-material issue in a topology optimization, a multiscale TO methodology by combining the sequential element rejection-admission (SERA) and boundary element evolvement is presented. As it is well known, the basic formulation of topology optimization only deals with two types of materials, and hence dealing with problems involving more than two types of materials becomes an obstacle on many occasions. In the proposed SERA approach, only the sensitivities of the boundary elements need to be computed and used, and an adaptive parameter updating strategy is introduced to balance the requirements on both the convergence and the quality performance of the solutions. To eliminate the dependence of the final solution on the initial topology, a new hole generating mechanism is proposed. In addition, a sensitivity filter is designed to remove the checkerboard patterns as well as to further eliminate the mesh-dependent problem. Also, a multi-level meshing method is introduced to help to reduce the design domain at the early stage of the optimization without sacrificing the resolution of the resultant topology. The numerical experiments demonstrate that for both di/tri-material problems, the proposed algorithm has a faster optimization speed. Lastly, in the optimization process of complex structure like electrical motors, the conventional modeling methods require too many control parameters to describe the topology of the device and hence have a complicated optimization procedure. To tackle this problem, a radial-basis function based shuffled frog leaping algorithm (SFLA) is developed and applied to the rotor topology optimization of an interior permanent magnet motor. The Gaussian radial-basis function significantly reduces the number of design parameters, and the modified shuffle frog leaping algorithm is able to efficiently explore and exploit the design apace. The performance of the proposed algorithm is compared with the conventional SFLA method, and the hybrid GA method; and the results indicate that the proposed

algorithm has a high efficiency with a good accuracy, when compared to the GA (low efficiency, good accuracy) and conventional SFLA (high efficiency, poor accuracy).

List of Publications

Journal Papers:

[1] **W. Yang,** S. L. Ho and S. Yang, "An efficient direct search methodology for robust optimization of electromagnetic devices", *IEEE Transactions on Magnetics*, vol. 54, no. 3, Art no. 7001004, 2018.

[2] **W. Yang,** S. L. Ho and W. N. Fu, "A multiscale topology optimization methodology based on sequential element rejection-admission and boundary element evolvement", *IEEE Transactions on Magnetics*, vol. 55, no. 6, Art no. 7201304, 2019.

[3] **W. Yang,** S. L. Ho and W. N. Fu, "Numerical and experimental study on design optimization of hybrid metamaterial slab for wireless power transmission" *IEEE Access*, vol. 8, pp. 82700-82708, 2020.

[4] **W. Yang,** S. L. Ho and W. N. Fu, "A modified shuffled frog leaping algorithm for the topology optimization of electromagnet devices", *Appl. Sci.*, vol.10, pp. 6186, 2020.

[5] **W. Yang,** S. L. Ho, and S. Yang, "A vector wind driven optimization algorithm for multi-objective optimizations of electromagnetic devices", *Intl. J. of Appl. Elec. and Mech.*, vol. 59, pp. 55 – 62, 2019.

[6] **W. Yang**, S. L. Ho, W. N. Fu, and S. Yang, "Design and analysis of metamaterials for wireless power transfer with same resonance frequency but different L/C combinations", *International Journal of Applied Electromagnetics and Mechanics* vol. 64, pp. 377–384, 2020.

Acknowledgements

I would like to express my heartfelt gratitude to my supervisors, Prof. Siu-lau Ho and Prof. Weinong Fu, for their continuous guidance, generous encouragement, and endless support in the past three years. I have learnt a lot from my supervisors, endeavor in career, devotion to research, attitude towards life, and the experience will benefit me for my whole life. I am forever grateful to both of them.

Secondly, I would like to thank all the group members in Applied Electromagnetic Laboratory, Dr. Shuangxia NIU, Dr. Xing Zhao, Dr. Xiaoyu Liu, Dr. Yiduan Chen, Dr Yunpeng Zhang, Sigao Wang, Yuanxi Chen for their valuable inspirations and suggestions. My thanks are extended the Department of Electrical Engineering.

Finally, I want to convey my deepest thanks to my family: thank you so much for your understanding and supports for my academic pursuit. I would like to thank my parents for bring me to life, raising me up, and endless love. I also would like to thank my girlfriend for being supportive.

This study was supported by the Research Grant Council of the Hong Kong SAR Government under projects PolyU-Q53A.

Table of Contents

Abstract 4

List of Publications 8

Acknowledgements 9

List of Figures 13

List of Tables 16

Abbreviation and Nomenclature 18

Chapter 1 Introduction 1

1.1 Background and Motivation of the Thesis 1

1.2 Research Objectives and Contributions 4

1.3 Thesis Organization 5

1.4 References-Part A 5

Chapter 2 Literature Review 12

2.1 Modelling Methods for Topology Optimization 13

2.1.1 Homogenization Method 13

2.1.2 Density-based Method 14

2.1.3 ON/OFF Method 16

2.1.4 Boundary Variation Method 17

2.1.5 Surrogate Model and Metamodel 24

2.2 Optimization Algorithms and Methods for Topology Optimization 28

2.2.1 Gradient-based Algorithms 28

2.2.2 Direct Search Methods 30

2.2.3 Genetic Algorithms 31

2.2.4 Particle Swarm Optimization Algorithms 33

2.2.5 Evolutionary Structural Optimization Algorithms 38

2.2.6 Other Stochastic Search Algorithms 40

2.3 Metamaterial and Its Applications in Wireless Power Transmission 51

2.4 Summary 60

2.5 Reference-Part B 62

Chapter 3 Robust Optimization of 2-D and 3-D electromagnetic problems 84

3.1 Introduction to Robust Optimization 84
3.2 A Direct Search Methodology for Robust Optimizations 86
3.2.1 New Formulation of a Robust Design Optimization 86
3.2.2 A Robust Oriented Quantum-Inspired Evolutionary Algorithm 87
3.2.3 Validation and Applications of the Proposed Robust Search Methodology .. 90
3.3 Robust Design Optimization of Metamaterials in Wireless Power Transmission Applications 94
3.3.1 Introduction 94
3.3.2 Formulations of the MM Optimization Problem 96
3.3.3 A Surrogate-model-based Robust Optimization Methodology 99
3.3.4 Numerical Results and Experimental Validations of the Proposed Methodology in MM Design Optimization 101
3.4 Summary 105
3.5 References-Part C 106
Chapter 4 Numerical Methods and Algori-thms for Wireless Power Transmission and Multi-Objective Topology Optimization 109
4.1 A DOE Assisted Surrogate Model for an Improved TABU Search Based Refinement Optimal Method in MM Slab optimizations 109
4.1.1 Metamaterial Slabs in Wireless Power Transmission Applications 109
4.1.2 A DOE Assisted Surrogate Model and Improved TABU Search Based Refinement Optimal Method 113
4.1.3 Numerical Results and Experimental Validation of the Proposed Method in HMM Design 119
4.1.4 Further Step: Derivation of the Analytical Model for the MM Structure in WPT System 127
4.2 A Vector Wind Driven Optimization Algorithm for Multi-Objective Topology Optimizations 136
4.2.1 Multi-Objective Design Optimization and Wind Driven Optimization Algorithm 136
4.2.2 A Vector Wind Driven Optimization Algorithm 137

4.2.3 Numerical Applications of the Proposed vector WDO Algorithm 140
4.3 Summary 144
4.4 Reference-Part D 146
Chapter 5 Evolutionary Algorithms for Multi-Material Topology Optimization and Radial Function based Optimization 150
5.1 A Multiscale Topology Optimization Methodology Based on Sequential Element Rejection–Admission and Boundary Element Evolvement 150
5.1.1 Sequential Element Rejection and Admission Method..... 150
5.1.2 Sequential Element Rejection and Admission in Multi-material Optimizations 151
5.1.3 Boundary Element Evolvement 152
5.1.4 Multiscale Optimization Procedures..... 153
5.1.5 The Proposed Multiscale SERA-BEE Methodology 154
5.2 Application of the Proposed Multiscale Topology Optimization Methodology..... 156
5.2.1 Optimization of Iron/Air in a Magnetic Actuator 157
5.2.2 Optimization of a PCB Substrate with Three Materials 158
5.3 A Modified Shuffled Frog Leaping Algorithm for Topology Optimizations of Electromagnet Devices..... 160
5.3.1 Shuffled Frog Leaping Algorithm..... 160
5.3.2 Normalized Gaussian Radial Basis Function Formulation 166
5.3.3 Problem Formulation and Numerical Application of the Proposed SFLA Method..... 167
5.4 Summary 174
5.5 Reference-Part E..... 175
Chapter 6 Conclusions and Future Works 179
6.1 Conclusion..... 179
6.2 Future Works 181

List of Figures

Chapter 2:

Fig. 2.1. Unit cell with void in the homogenization method.....14

Fig. 2.2. Schematic representation of the ON/OFF method.....16

Fig. 2.3. Schematic representation of the level-set function and method.....18

Fig. 2.4. Schematic representation of (a) conforming discretization mapping and (b) immersed boundary technique.....20

Fig. 2.5. Schematic representation of (a) 2D phase field representation of domain and (b) 1D phase field function.....23

Fig. 2.6. Workflow of surrogate model construction.....24

Fig. 2.7. Example of LHS sampling with two parameters and 1/4 sample ratio.....25

Fig. 2.8. Workflow of GA.....31

Fig. 2.9. Graphical representation of PSO……...35

Fig. 2.10. Workflow of the bi-directional-ESO.....38

Fig. 2.11. Workflow of SA.....42

Fig. 2.12. Workflow of advanced TS.....44

Fig. 2.13. Workflow of three-phase ABC.....46

Fig. 2.14. Workflow of three-phase ACO.....48

Fig. 2.15. Workflow of firefly algorithm.....50

Fig. 2.16. Refraction of conventional material and MM.....52

Fig. 2.17. Existing MM structures and relative positions in WPT system.....55

Fig. 2.18. Equivalent circuit of magnetic resonance based WPT system.....56

Fig. 2.19. Plot of against of resonance based WPT system.....57

Chapter 3:

Fig. 3.1. The TEAM workshop 22 SMES configuration.....90

Fig. 3.2 The equivalent circuit of a MM unit cell.....97

Fig. 3.3. (a) MM unit cell and (b) the MM slab structure.....101

Fig. 3.4. Four coil WPT system with a metamaterial slab in the numerical

application.....102

Chapter 4:

Fig. 4.1. Refractive principle of MM with zero and MM with negative μ_r.....110

Fig. 4.2. Identification of the classification of different types of unit cells.....114

Fig. 4.3. Design domain and four subdomains of the two capacitors.....115

Fig. 4.4. Flow chart of the proposed methodology.....118

Fig. 4.5. The prototype R-WPT system under optimization.....120

Fig. 4.6. Comparison of a full FEM simulation and the proposed Kriging model on the objective function values of the best candidates in the five iterative cycles.....122

Fig. 4.7. Propagation of B field in HMM assisted WPT system.....124

Fig. 4.8. *B*-field distributions for (a) proposed HMM slab, (b) HMM slab with only one defect at centre, and (c) Homogenous slab.....124

Fig. 4.9. (a) Experimental setup (side view). (b) Actual HMM slab.....125

Fig. 4.10. C-shape electromagnet with an MM structure.....126

Fig. 4.11. (a) Plot of real and imaginary part of $\frac{\dot{I}_m}{\dot{I}_s}$ vs input current frequency; (b) Polar plot of $\frac{\dot{I}_m}{\dot{I}_s}$ 130

Fig. 4.12. The Plot of (a) Capacitance vs Relative permeability; and (b) Capacitance vs Reluctance; of the proposed NEMR structure.....132

Fig. 4.13. The Plot of (a) Frequency vs Relative permeability; and (b) Frequency vs Reluctance; of the proposed NEMR structure.....133

Fig. 4.14. The configuration of M-element linear arrays placed on the z-axis.....139

Fig. 4.15. The design variables of the multi-sectional pole shoes.....141

Chapter 5:

Fig. 5.1. Examples of the (i) initial mesh, (ii) intermediate mesh, (iii) final mesh....152

Fig. 5.2. The block diagram of the proposed methodology.....154

Fig. 5.3. Schematic diagram of the prototype actuator.....155

Fig. 5.4. Resultant topology of (i) ON/OFF; (ii) BESO; (iii) Proposed.....155

Fig. 5.5. The PCB substrate design problem.....157
Fig. 5.6. Optimized Topology of (i) the original in [E11]; (ii) the proposed method with (iii) without, an adaptive admission/rejection ratio.....157
Fig. 5.7. Flowchart of the Shuffled Frog-Leaping algorithm.....160
Fig. 5.8. The initial discretized design domain and RBFs used (in red).....166
Fig. 5.9. The conventional design of IPM used for comparison (a) cross-section; and (b) torque plot.....167
Fig. 5.10. The Optimized design of IPM obtained by the conventional SFLA (a) cross-section; and (b) torque plot.....169
Fig. 5.11. The Optimized design of IPM obtained by the LS-GA (a) cross-section; and (b) torque plot.....169
Fig. 5.12. The Optimized design of IPM obtained by the proposed algorithm (a) cross-section; and (b) torque plot.....170

List of Tables

Chapter 2:

Table 2.1. summary of the current study in MM based WPT.....58

Table 2.2. Summary of the modelling method in topology optimization.....59

Table 2.3. Summary of the optimization algorithms in topology optimization.....60

Chapter 3:

Table 3.1 Performance of different algorithms on the benchmark function.....90

Table 3.2 The physical parameters of the metamaterial structure.....101

Table 3.2 PTE and its degradation under different turn unit cell MM slabs.....102

Chapter 4:

Table 4.1 Circuit parameters of two experiments.....120

Table 4.2 Comparison of different surrogate models.....121

Table 4.3 Experiment results.....125

Table 4.4 The trial values of the parameters in the equation 4.15.....129

Table. 4.5 The values of all parameters for numerical experiment.....132

Table 4.6 Electromagnetic properties of the proposed NEMR structure at different number of turns 133

Table 4.7 Performance Comparison of Different Algorithms on Case Study Two.....142

Chapter 5:

Table 5.1 Performance comparison of three algorithms.....156

Table 5.2 Material properties of the three types of materials.....157

Table 5.3 Performance comparison of the proposed method.....158

Table 5.4 PM fixed parameter values.....165

Table 5.5 Algorithm parameters used, and the results obtained for two test runs of SFLA.....168

Table 5.6 Summary of optimization performance of all three EAs.....169

Abbreviations and Nomenclature

TO	Topology Optimization
FEM	Finite Element Method
RSM	Response Surface Model
GA	Genetic Algorithm
PSO	Particle Swarm Optimization
NSGA-II	Non-dominate sorted GA-II
DOE	Design-of-experiment
SFLA	Shuffled-Frog-Leap Algorithm
SERA	Sequential Element Rejection and Admission
SIMP	Solid Isotropic Material Penalization
RAMP	Rational Approximation of Material Properties
LSF	Level-set Function
LSM	Level-set Method
XFEM	Extended Finite Element Method
H-J	Hamilton-Jacobi
LHS	Latin-Hypercube-Sampling
DOE	Design-of-experiment
RBF	Radial-Basis-Function
SPSA	Simultaneous Perturbation Stochastic Approximation
SPEA2	Strength Pareto Evolutionary Algorithm
ESO	Evolutionary Structural Optimization
BESO	Binary Evolutionary Structural Optimization
DEA	Differential Evolution Algorithm
IPM	Interior Permanent-Magnet
SA	Simulated Annealing
PM	Permanent-Magnet
TS	Tabu Search
ABC	Artificial Bee Colony
ACO	Ant Colony Optimization
MM	Metamaterial
EM	Electromagnetic
WPT	Wireless Power Transmission
PTE	Power Transmission Efficiency
QEA	Quantum-inspired Evolutionary Algorithm
SA	Stochastic Approximation
GA^S/RS^3	Genetic Algorithms with Robust Solution Searching Scheme
MEM	Multiple Evaluation Model
SMES	Superconducting Magnetic Energy Storage
PCEA	Polynomial Chaos Evolutionary Algorithm
R-WPT	Resonance coupled Wireless Power Transmission

PCB	Printed Circuit Board
HMM	Hybrid Metamaterial
LI	Linear Interpolation
WDO	Wind Driven Optimization
MSLL	Maximum Side-Lobe Level
SCR	Short Circuit Ratio
THF	Telephone Harmonic Factor
BEE	Boundary Element Evolvement
MTO	Multiscale Topology Optimization
LS-GA	Local Search assisted Genetic Algorithm

Chapter 1 Introduction

1.1 Background and Motivation of the Thesis

Design and optimization of a device is the process of determining the physical structure of the devices that yields the best performances under certain pre-defined criteria. Based on the level of complexity, optimization process can be divided into three levels, namely the parameter or seize optimization, shape optimization and topology optimization [A1]. The topology of a structure describes the connectivity of materials within the structure [A2], whereas optimizing the topology of a structure is the process that determines the distribution of different materials within the structure under some predefined criteria. Compared to the other two types of optimization processes, topology optimization imposes no restriction on the geometry of the structure, and hence enjoys the merit of having more degrees of freedom during optimization process and possibility of obtaining innovative structures that could not be obtained from shape or parameter optimizations [A3]. Therefore, topology optimization has been extensively studied and proved to be efficient for device designs in the past few decades in various disciplines. The idea of applying topology optimization procedures to mechanical engineering problems was first introduced in 1989 by Bendsoe [A4] and has soon been extended to applications in aerospace design, fluid mechanics, medications, mechanical engineering, and electrical engineering [A5-A11]. However, as the degree of freedom of the design increases, the number of design parameters, as well as the level of complexity of the optimization process increase accordingly as well, making the topology optimization a time-consuming process that requires numerous mathematical operations and heavy computational resources. Despite the huge amount of related researches, the development of appropriate topology optimization methods and algorithms is still in urgent needs and requires continuous efforts.

In the current study of the topology optimization problems, generally there are two major obstacles. The first one is the transformation from the actual engineering design requirement to a mathematical problem that can be solved with the aid of computers. This transformation process includes creating appropriate mathematical formulations to represent the constraints and goals of the optimization problem, as well as generating an appropriate numerical model that can represent the topology of the devices under optimization using a set of controllable design parameters, and also able to undergo performance evaluation using numerical methods such as the finite-element method (FEM). A number of numerical modelling methods, such as the solid isotropic material with penalization method [A12-A14], the level set method [A15-A18], the ON/OFF method [A19-A20], are proposed to accurately reconstruct the topology of the devices. Based on the descripted methods, these modelling methods can be categorized as the density-based methods and the boundary-based methods. Moreover, to reduce the design parameters involved, the surrogate models that employ some basis functions to reconstruct different topologies, such as the response surface methods (RSM) [A21, A22], the Kriging methods [A23, A24] and radial-basis function methods [A25], are employed in association with the aforementioned numerical modelling methods and evaluation methods in the topology optimization process and have been proved to have a faster optimization speed. However, imposing the surrogate model in the reconstruction process for the topology of the device will certainly impose constraints to the shape and topology of the device, leading to losing certain degrees of freedoms. Hence, there is a need to find a balance between the accuracy and the complexity of the modelling method employed in topology optimization.

The second important issue in the study of the topology optimization is the choice of an appropriate optimization algorithm. The nature of the algorithm employed in the optimization process will significantly affect the performances of the optimization. Based on the search methodology, optimization algorithms can be divided into two categories as well: the deterministic algorithms, where the search process during the optimization is generally guided by the gradient information of the objective function; and the stochastic algorithms, where the search process is conducted in a random

manner [A26]. The former ones, such as the Newton's method, Optimality criteria method, and mathematical programming method, have been extensively studied for last few decades, and are relatively mature [A27-A30]. Because the entire search process is guided by the sensitivity information of the system, the deterministic algorithms have a fast convergence speed. However, due to the requirement of the gradient information or derivative information to guide the search process, the deterministic algorithm can lead to tedious calculation procedures in solving black-box problems, where the system equations governing the devices are not directly available [A31], and also inappropriate for multi-objective problems. On the other hand, stochastic algorithms employ random search procedures and hence requires no preliminary information related to the system. These algorithms often imitate nature evolving processes or nature procedures, and apply them into the optimization process, and due to the reason that no gradient information is required, the stochastic algorithms can be easily applied to black-box problems [A32]. The most well-studied stochastic algorithms are the evolutionary algorithm family. These algorithms include genetic algorithm (GA) [A33-A35], particle swarm optimization algorithm (PSO) [A36-A38], evolutionary structural optimization [A39-A40], differential evolution [A41-A43], and other algorithms. All algorithms are developed based on a population of possible topologies and a natural searching phenomenon that guides the evolution of the population. Moreover, because of the ease of application and high flexibility, evolutionary algorithms have showed great potentials in multi-objective optimization, and their multi-objective counterpart such as the non-dominate sorted GA-II (NSGA-II) have been proposed and applied to many circumstances [A44-A46]. However, despite their unique flexibility, the stochastic algorithms sometimes associate issues such as low convergence speed, fluctuation at local optima, and premature convergence [A47], and hence their applications always require careful calibrations.

In the field of electrical engineering, despite the fact that the study of topology optimization slightly lags behind that of other disciplines, a lot of efforts have been put into its development in the past two decades. By using stochastic algorithms with FEM simulations, topology optimization has been successfully applied to devices such as

actuators [A48-A50], transformers [A51-A54], electrical motors [A55-A58], magnetic gears [A59-A61] and other devices. The device topologies obtained by using topology optimization techniques are more innovative, and hence performances of the electromagnetic devices can be further enhanced. However, the applications of topology optimization in the electromagnetic devices still face the problems of heavy time costs, large manufacturing difficulties, little repeatability and so on [A62].

In view of the need for the continuous efforts on the research of the topology optimization in the electromagnetic problems and devices, this thesis mainly focuses on the study and development of appropriate modelling techniques, optimization methodologies and algorithms that are suitable for electromagnetic device topology optimizations, especially for devices converting magnetic energy to other forms. The thesis will try to address the issues in both academic studies and actual applications of topology optimization techniques, including the adaption from single-objective optimization to multi-objective optimization, the reduction of optimization time using surrogate model and other related techniques, and the development of newly proposed algorithms.

1.2 Research Objectives and Contributions

This study strives to address typical problems and challenges encountered in a topology optimization process of electromagnetic device designs. The challenging problems and issues include the uncertainties in the manufacturing process of a topology optimized device, the extremely computationally expensive procedure of a topology optimization, the multi-criteria and multi-material natures of a topology optimization problem, and the deficiency in mathematical modeling and definition of topologies for complex three dimensional topology optimization problem. The contributions of this study are:

1) To deal with the uncertainties in the engineering manufacturing of a device, a direct search methodology for robust topology optimizations is developed based on the quantum evolutionary algorithm, and numerically proved to be efficient when compared with other conventional robust optimizers.

2) To combat the extremely computationally expensive problem of a topology optimization procedure, a design-of-experiment (DOE) assisted surrogate model for an improved TABU search based refinement optimal method is proposed. To provide a vector optimizer for multi-objective topology optimization problems, a vector wind driven optimization algorithm for multi-objective topology optimizations is also developed.
3) To address the multi-material issue in a topology optimization, a multiscale topology optimization methodology by combining the sequential element rejection-admission (SERA) and boundary element evolvement is presented. To eliminate the deficiency in modelling a complex structure like electrical motors, a radial-basis function based shuffled frog leaping algorithm (SFLA) is developed and applied to the rotor topology optimization of an interior permanent magnet motor.

1.3 Thesis Organization

The remainder of this thesis is organized in the following manner. Chapter 2 reviews the development of topology optimization techniques and the related application scenarios of the thesis. Various topology optimization algorithms and mathematical modelling methods, as well as their pros and cons are explained and analyzed. Moreover, the applications of topology optimization, especially in the field of electromagnetic engineering are presented. In Chapter 3, numerical methodologies and algorithms developed for robust topology optimizations are presented. In Chapter 4, the surrogate model-based optimization methodologies and algorithms for complex 3-D electromagnetic problem are developed. In Chapter 5, a memetic algorithm that is crafted to solve complex electromagnetic black-box problem with the aid of radial-basis function is presented. Lastly, Chapter 6 gives conclusion of this thesis and scope for future work.

1.4 References-Part A

[A1] Eschenauer HA, Olhoff N, “Topology optimization of continuum structures: a

review," *Appl Mech Rev*, vol. 54, pp.331-390, 2001.

[A2] G. Rozvany, "A critical review of established methods of structural topology optimization," *Struct Multidisc Optim*, vol. 37, pp. 217-237, 2009.

[A3] Joshua D. Deaton, Ramana V. Grandhi, "A survey of structural and multidisciplinary continuum topology optimization: post 2000," *Struct Multidisc Optim*, vol. 49, pp.1-38, 2014.

[A4] M. Bendsøe, "Optimal shape design as a material distribution problem." *Structural and Multidisciplinary Optimization*, vol.1, issue. 4, pp.193-202, 1989.

[A5] Y. Luo, J. Bao, "A material-field series-expansion method for topology optimization of continuum structures," *J. Computers and Structures*, vol. 225, Article no. 106122, 2019.

[A6] C. Chen, D. Chrzan, and G. Gu, "Nano-topology optimization for materials design with atom-by-atom control," *Nature Communications*, vol. 11, no. 1, pp.1-9, 2020.

[A7] J. Groen and O. Sigmund, "Homogenization‐based topology optimization for high‐resolution manufacturable microstructures," *International Journal for Numerical Methods in Engineering*, vol. 113, no. 8, pp.1148-1163, 2018.

[A8] B. Dühring, J. Jensen, and O. Sigmund, "Acoustic design by topology optimization," *Journal of Sound and Vibration*, vol. 317, pp.557-575, 2008.

[A9] H. Kollmann, and et al., "Deep learning for topology optimization of 2-D metamaterials," *Materials and Design*, vol. 196, Article no. 109098, 2020.

[A10] L. Cheng, J. Bai, and C. Albert, "Functionally graded lattice structure topology optimization for the design of additive manufactured components with stress constraints," *Computer Methods in Applied Mechanics and Engineering*, vol. 344, pp.334-359, 2019.

[A11] W. Zhang, and et al., "Explicit three-dimensional topology optimization via Moving Morphable Void (MMV) approach," *Computer Methods in Applied Mechanics and Engineering*, vol. 322, pp.590-614, 2017.

[A12] M. Bendsøe, and O. Sigmund, "Material interpolation schemes in topology optimization," *Arch Appl Mech*, vol. 69, pp.635-654, 1999.

[A13] O. Sigmund, andJ. Jensen, “Systematic design of phononic band-gapmaterials and structures by topology optimization,” *Philos Trans Royal Soc London Ser A: Math Phys Eng Sci*, vol. 361, pp.1001-1019, 2003.

[A14] S. Halkjær, O. Sigmund, and J. Jensen JS, “Inverse design of phononic crystals by topology optimization,” *Z Krist*, vol. 220, pp.895-905, 2005.

[A15] J. Sethian, A. Wiegmann, “Structural boundary design via level-set and immersed interface methods,” *J Comput Phys*, vol. 163, no. 2, pp.489- 528, 2000.

[A16] M. De Ruiter, and F. Keulen, “Topology optimization using a topology description function,” *Struct Multidisc Optim*, vol. 26, no. 6, pp.406-416, 2004.

[A17] G. Allaire, F. Jouve, A. Toader, “A level-set method for shape optimization,” *CR Math*, vol. 334, no. 12, pp.1125-1130, 2002.

[A18] G. Allaire, F. Jouve F, A. Toader, “Structural optimization using sensitivity analysis and a level-set method,” *J Comput Phys*, vol. 194, no. 1, pp.363-393, 2004.

[A19] K. Watanabe, T. Suga and S. Kitabatake, “Topology optimization based on the ON/OFF method for synchronous motor,” *IEEE Transactions on Magnetics*, vol. 54, no. 3, Art no. 7201104, 2018.

[A20] H. Mirahki, M. Moallem, M. Ebrahimi, and B. Fahimi, B, “Combined ON/OFF and conformal mapping method for magnet shape optimisation of SPMSM,” *IET Electric Power Applications*, vol. 12, no. 9, pp.1365-1370, 2018.

[A21] Z. Li, M. Gerdroodbary, P. Valipour, P., Moradi, and H. Babazadeh, “The optimization via response surface method for micro hydrogen gas actuator,” *International Journal of Hydrogen Energy*, vol. 44, no. 59, pp.31633-31643, 2019.

[A22] O. Rezaifar, M. Hasanzadeh, and M. Gholhaki, “Concrete made with hybrid blends of crumb rubber and metakaolin: optimization using response surface method,” *Construction and Building Materials*, vol. 123, pp.59-68, 2016.

[A23] M. Bouhlel, and et al., “Efficient global optimization for high-dimensional constrained problems by using the Kriging models combined with the partial least squares method,” *Engineering Optimization*, vol. 50, no. 12, pp.2038-2053,

2018.

[A24] J. Qian, and et al., “A sequential constraints updating approach for Kriging surrogate model-assisted engineering optimization design problem,” *Engineering with Computers*, pp.1-17, 2019.

[A25] A. Alexandridis, E. Chondrodima, and H. Sarimveis, “Cooperative learning for radial basis function networks using particle swarm optimization” *Applied Soft Computing*, vol. 49, pp.485-497, 2016.

[A26] S. Zargham, T. Ward, R. Ramli, and I. Badruddin, “Topology optimization: a review for structural designs under vibration problems,” *Structural and Multidisciplinary Optimization*, vol. 53, no. 6, pp.1157-1177, 2016.

[A27] Arora JS, “Sequential linearization and quadratic programming techniques,” *Prog Astronaut Aeronaut*, vol. 150, pp.71–71, 1993.

[A28] W. Prager, and J. Taylor, “Problems of optimal structural design,” *J Appl Mech*, vol. 35, no. 1, pp.102–106, 1968.

[A29] C. Fleury, “Structural weight optimization by dual methods for convex programming,” *Int J Numer Methods Eng*, vol. 14, no. 12, pp.1761–1783, 1979.

[A30] D. Agarwal, P. Singh, P., X. Li, and S. Kumari, “Optimality criteria for fuzzy-valued fractional multi-objective optimization problem,” *Soft Computing*, vol. 23, no. 19, pp.9049-9067, 2019.

[A31] M. Vasileios, T. Aris, and A. Kleo, “Algorithms for optimization of building design: A review,” *Renewable and Sustainable Energy Reviews*, vol. 31, pp.101-112, 2014.

[A32] M. Niu, C. Wan and Z. Xu, “A review on applications of heuristic optimization algorithms for optimal power flow in modern power systems,” *Journal of Modern Power Systems and Clean Energy*, vol. 2, no. 4, pp.289-297, 2014.

[A33] Y. Tominaga, Y. Okamoto, S. Wakao and S. Sato, “Binary-based topology optimization of magnetostatic shielding by a hybrid evolutionary algorithm combining genetic algorithm and extended compact genetic algorithm,” *IEEE Transactions on Magnetics*, vol. 49, no. 5, pp.2093-2096, 2013.

[A34] K. Choi, and et al., “Hybrid algorithm combing genetic algorithm with

evolution strategy for antenna design," *IEEE Transactions on Magnetics*, vol. 52, no. 3, Article no. 7209004, 2016.

[A35] J. Rayno, M. Iskander and M. Kobayashi, "Hybrid genetic programming with accelerating genetic algorithm optimizer for 3-D metamaterial design," *IEEE Antennas and Wireless Propagation Letters*, vol. 15, pp.1743-1746, 2016.

[A36] J. Seo, and et al., "Multimodal function optimization based on particle swarm optimization," *IEEE Transactions on Magnetics*, vol. 42, no. 4, pp.1095-1098, 2006.

[A37] J. Seo, C. Im, S. Kwak, C. Lee and H. Jung, "An improved particle swarm optimization algorithm mimicking territorial dispute between groups for multimodal function optimization problems," *IEEE Transactions on Magnetics*, vol. 44, no. 6, pp.1046-1049, 2008.

[A38] M. Pham, D. Zhang and C. Koh, "Multi-guider and cross-searching approach in multi-objective particle swarm optimization for electromagnetic problems," *IEEE Transactions on Magnetics*, vol. 48, no. 2, pp.539-542, 2012.

[A39] Q. Liang, G. Steven GP, "A performance-based optimization method for topology design of continuum structures with mean compliance," *Comput Methods Appl Mech Eng*, vol. 191, pp.1471-1489, 2002.

[A40] X. Huang, Y. Xie, "Convergent and mesh-independent solutions for the bi-directional evolutionary structural optimization method," *Finite Elem Anal Des*, vol. 43, no. 14, pp.1039-1049, 2007.

[A41] Q. Fan and X. Yan, "Self-adaptive differential evolution algorithm with zoning evolution of control parameters and adaptive mutation strategies," *IEEE Transactions on Cybernetics*, vol. 46, no. 1, pp.219-232, 2016

[A42] L. Huang, L. Liao and C. Wu, "Evolutionary model selection and parameter estimation for protein-protein interaction network based on differential evolution algorithm," *IEEE Transactions on Computational Biology and Bioinformatics*, vol. 12, no. 3, pp.622-631, 2015.

[A43] S. Sotiroudis, and et al., "Application of a composite differential evolution algorithm in optimal neural network design for propagation path-loss prediction

in mobile communication systems," *IEEE Antennas and Wireless Propagation Letters*, vol. 12, pp.364-367, 2013.

[A44] P. Murugan, S. Kannan and S. Baskar, "Application of NSGA-II algorithm to single-objective transmission constrained generation expansion planning," *IEEE Transactions on Power Systems*, vol. 24, no. 4, pp.1790-1797, 2009.

[A45] J. Yang, and et al., "Synthesis of conformal phased array with improved NSGA-II algorithm," *IEEE Transactions on Antennas and Propagation*, vol. 57, no. 12, pp.4006-4009, 2009.

[A46] L. Zhang, and et al., "Multi-objective optimization design of a notch filter based on improved NSGA-II for conducted emissions," *IEEE Access*, vol. 8, pp.83213-83223, 2020.

[A47] M. Pastorino, "Stochastic optimization methods applied to microwave imaging: A review," *IEEE Transactions on Antennas and Propagation*, vol. 55, no. 3, pp.538-548, 2007.

[A48] S. Lim, S. Jeong and S. Min, "Multi-component layout optimization method for the design of a permanent magnet actuator," *IEEE Transactions on Magnetics*, vol. 52, no. 3, Article no. 7205304, 2016.

[A49] S. Park, and et al., "Magnetic actuator design using level-set based topology optimization," *IEEE Transactions on Magnetics*, vol. 44, no. 11, pp.4037-4040, 2008.

[A50] S. Jeong, S. Lim and S. Min, "Level-set-based topology optimization using remeshing techniques for magnetic actuator design," *IEEE Transactions on Magnetics*, vol. 52, no. 3, Article no. 7205504, 2016.

[A51] M. Tsili, and et al., "Geometry optimization of magnetic shunts in power transformers based on a particular hybrid finite-element boundary-element model and sensitivity analysis," *IEEE Transactions on Magnetics*, vol. 41, no. 5, pp.1776-1779, 2005.

[A52] A. Berbecea, and et al., "Comparison of efficient global optimization and output space mapping on the bi-objective optimization of a safety isolating transformer," *IEEE Transactions on Magnetics*, vol. 48, no. 2, pp.791-794, 2012.

[A53] E. Amoiralis, and et al., “A parallel mixed integer programming-finite element method technique for global design optimization of power transformers,” *IEEE Transactions on Magnetics*, vol. 44, no. 6, pp.1022-1025, 2008.

[A54] K. Dawood, A. Köseoğlu and G. Kömürgöz, “Design optimisation for distance between additional and tap winding in high-voltage transformers,” *High Voltage*, vol. 5, no. 6, pp.716-723, 2020.

[A55] M. Onsal, et al., “Rotor design optimization of a new flux-assisted consequent pole spoke-type permanent magnet torque motor for low-speed applications,” *IEEE Transactions on Magnetics*, vol. 54, no. 11, Article no. 8206005, 2018.

[A56] W. Han, and et al., “Global-simplex optimization algorithm applied to FEM-based optimal design of electric machine,” *IEEE Transactions on Magnetics*, vol. 53, no. 6, Article no. 8106904, 2017.

[A57] W. Han, and et al., “Mass ionized particle optimization algorithm applied to optimal FEA-based design of electric machine,” *IEEE Transactions on Magnetics*, vol. 52, no. 3, Article no. 8200404, 2016.

[A58] Y. Ma, T. Ching, W. N. Fu and S. Niu, “Multi-objective optimization of a direct-drive dual-structure permanent magnet machine,” *IEEE Transactions on Magnetics*, vol. 55, no. 10, Article no. 7501704, 2019.

[A59] S. Niu, N. Chen, S. Ho and W. Fu, “Design optimization of magnetic gears using mesh adjustable finite-element algorithm for improved torque,” *IEEE Transactions on Magnetics*, vol. 48, no. 11, pp.4156-4159, 2012.

[A60] E. Göbl, G. Jungmayr, E. Marth and W. Amrhein, “Optimization and comparison of coaxial magnetic gears with and without back iron,” *IEEE Transactions on Magnetics*, vol. 54, no. 11, Article no. 8001604, 2018.

[A61] W. Fu and L. Li, “Optimal design of magnetic gears with a general pattern of permanent magnet arrangement,” *IEEE Transactions on Applied Supercond.*, vol. 26, no. 7, Article no. 0606705, 2016.

[A62] D. Guirguis, and et al., “Evolutionary black-box topology optimization: challenges and promises,” *IEEE Transactions on Evolutionary Computation*, vol. 24, no. 4, pp.613-633, 2020.

Chapter 2 Literature Review

Topology optimization is originated from a two-state or two-phase material optimization. Generally, a two-state (solid/air) topology optimization problem can be described as finding the material distribution that minimizes (or maximizes) the objective function F. The constraints of the design include the volume constraint, G_0, and all other possible constraint G_i. The density of the material, or the material state, at location x in the design domain, Ω, is represented by $\rho(x)$, with value of either 0 (air) or 1 (solid). The topology optimization problem can thus be formulated as [B1]:

$$\begin{aligned}
&\min_{\rho} : F = F(\mathrm{u}(\rho),\rho) = \int_{\Omega} f(\mathrm{u}(\rho),\rho)dV \\
&\text{s.t.} \quad : G_0(\rho) = \int_{\Omega} \rho(x)dV \le V_0 \\
&\qquad : G_i(\mathrm{u}(\rho),\rho) = 0, i = 1,2,3,...,N \\
&\qquad : G_j(\mathrm{u}(\rho),\rho) < 0, j = 1,2,3,...,M \\
&\qquad : \rho(x) = 0 \text{ or } 1, \forall x \in \Omega
\end{aligned} \tag{2.1}$$

In the formulation it is assumed that the objective function F can be evaluated as an integral of certain local functions $u(\rho)$, for instance, the magnetic energy density in terms of the electromagnetic content. G_i and G_j are the equality and inequality constraints in the system. In the formulation here only two states of materials are considered; and for more than two states, the formulation is similar. As mentioned in the previous chapter, there are mainly two obstacles in the development of efficient topology optimization procedures, namely the modelling of the devices under optimization and the development of appropriate optimization algorithms. With the aid of modern computing devices, the complexity of the topology optimization problems has increased tremendously in the past few decades, and hence the optimization methods have also experienced vast developments accordingly. In this chapter the development of topology optimization methodologies is reviewed. The advantages and disadvantages of various methods are identified and elaborated in order to pinpoint the research gap existing in topology optimization, especially in the electromagnetic

applications.

2.1 Modelling Methods for Topology Optimization

Thanks to the advent of modern computers, nowadays the evaluation of the performance of the electromagnetic devices can be done using computer simulations. During the simulation, inevitably there is a need to transform the actual device topology to a mathematical model, and the accuracy and complexity of this transformation significantly influence the efficiency of the following up optimization process. Based on the principle of formulation, modelling methods can be divided as the discretization methods and boundary methods. Moreover, to further reduce the complexity of the numerical model, the hybridization of these two methods, and other replacement methods have been developed.

2.1.1 Homogenization Method

One of the earliest numerical modelling methods developed to model 2-D devices in computer simulations was the homogenization method [B1]. The method divides the design domain into small elements. Within each element, a void region with widths of a and b is created at the center of the element, as depicted in Figure 2.1. The topology of the device is then controlled by the values of a and b of each element, and the topology optimization problem can be formulated as [B2]:

$$\begin{aligned} &\min F(a_e, b_e, \theta_e) \\ &s.t. \sum_{e=1}^{N} (1 - a_e b_e) v_e - V \le 0 \\ &\quad 0 \le a_e, b_e \le 1 \end{aligned} \tag{2.2}$$

Here, F is the objective function; θ_e, a_e and b_e are the rotation angle and the two widths of the void of element e; V is the volume/area constraint of the problem. The number of the control parameters in the homogenization method is relatively large, as for each element there are three control parameters. This leads to the increment of the complexity of the modelling process and the optimization process. Moreover, the homogenization method is suitable in occasions where two materials are involved, and

the occasions where the void is located at the center of the material [B3-B6]. For topologies with more than two types of materials, using the homogenization method may not be sufficient to clearly represent the topologies. Moreover, the existence of void region at the center of solid element leads to the existence of checkerboard patterns at the solid region, and uneven boundaries at the material interface which makes the obtained topology hard to be manufactured.

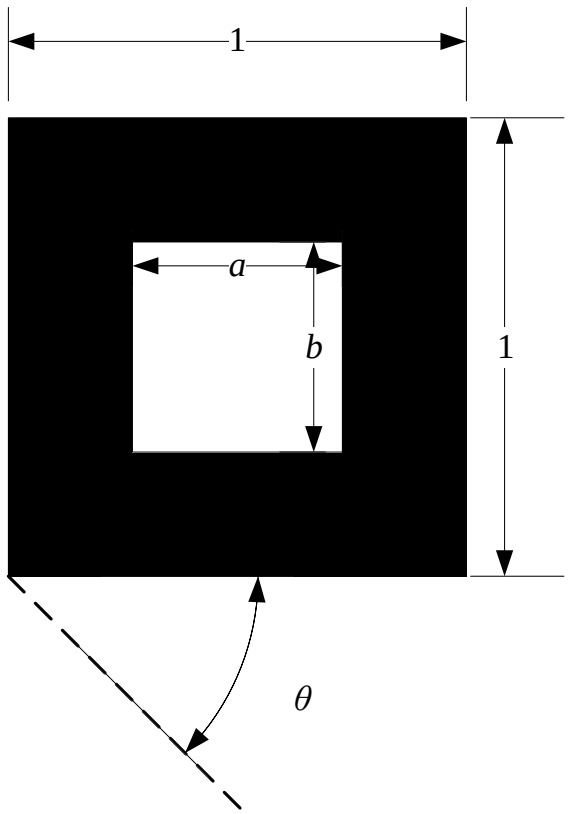

Fig. 2.1. Unit cell with void in the homogenization method.

2.1.2 Density-based Method

The density-based modelling method can be viewed as an improved version of the homogenization method. Both methods discretize the design domain into small unit cell, and the main difference between the two methods is the way to represent the material type for each unit cell. Unlike the homogenization method, the density-based method represents the material type for each unit cell in a continuous manner. The most well-adopted density-based method is the solid isotropic material penalization method (SIMP) proposed by Rozvany and Zhou [B7]. In their original paper, to model

the topology of a beam structure, the design domain, which is a rectangle, is divided into finite numbers of small rectangle unit cells of equal size. Each unit cell has its own function to represent its material type and material distribution. Taking the elasticity problem as an example, the Young's modulus of a unit cell in SIMP method can be described as [B8]:

$$E(x_e) = \rho(x_e)^p E_0 \tag{2.3}$$

where E_0 is the Young's modulus of the solid material, $\rho(x)$ is the relative density function of element x_e in the design domain, and p is the penalty factor. As the density of the material becomes a continuous function, rather than a binary representation in the homogenization method, the topology of the device becomes a smooth distribution of different materials, and this significantly reduces the possibility of checkerboard pattern. However, intermediate density may occur in a density-based method, and its meaning is unclear during the optimization process. Some researchers regard the intermediate density as a partial filled unit cell with the filling direction defined by the user, but in this regard one material function can represents more than one topology, which further increases the complexity of the optimization process [B9]. Nevertheless, when dealing with truss or beam structures, SIMP is still one of the most commonly employed and efficient methods [B10-B15]. Certain extensions of SIMP have been made to make the method more appropriate for more complex problems. For instance, in [B16-B19], the value of density function is divided into multiple intervals within [0,1], each interval represents one type of material and hence multi-material modeling can be realized by using the modified SIMP method. In [B20-B21], a continuum SIMP that allows the penalty factor p to vary is proposed. This adaption significantly increases the optimization speed in the follow up numerical experiments. Similar to the SIMP, other density-based methods, such as the rational approximation of material properties (RAMP), employ similar idea of representing the material property of unit cell with penalty functions. For instance, the permeability of material in each unit cell can be represented by [B22]:

$$\mu(x_e) = \frac{\rho(x_e)}{1 + p(1 - \rho(x_e))}\mu_0 \tag{2.3a}$$

Similar to the SIMP method, here μ represents the permeability of the material, $\rho(x)$ is the relative density function of element x_e, and p is the penalty factor. While sharing the same modelling mechanism, the RAMP method also has the problem of intermediate density occurrence, and dependency of an initial topology during the optimization process as well.

2.1.3 ON/OFF Method

The ON/OFF method discretizes the design domain into finite numbers of small unit elements. Each element is associated with its own material state. In typical ON/OFF method, the unit element can be filled with only solid state (material) or void state (air), as depicted in Figure 2.2. The black boxes in Figure 2.2 represent solid elements, and the white boxes represent void elements.

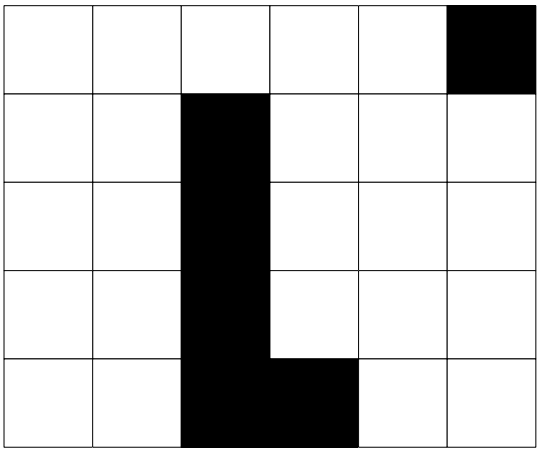

Fig. 2.2. Schematic representation of the ON/OFF method.

Compared to other types of discretized methods, the ON/OFF method is much straightforward and convenient in applications. The size of all elements can be identical [B23] or different [B24], rendering the method to work together easily with FEM, and also appropriate for complex problems with variable mesh element sizes. Moreover, unlike the other types of discretized methods that require the governing equation of the systems to solve for the material property and gradient information, the ON/OFF method can be used together with both direct search algorithms or stochastic algorithms, which further extend its scope of applications. In

electromagnetic applications, the ON/OFF method is often coupled with evolutionary algorithms to solve design and optimization problems for electrical motors [B25], actuators [B26], and other types of devices. One issue with the ON/OFF modelling method is the relatively large number of design parameters, as each unit element has its own design parameter controlling the material state. Hence, researches combining ON/OFF method together with the level-set method, which is a boundary tracking method and will be introduced in the next section, have been proposed and have been proved to be more efficient than the conventional ON/OFF method [B27]. In this application, the level-set method tracks the changes of material boundary during the optimization, while the material distribution in the design domain is modelled by the ON/OFF method. Another issue with the ON/OFF method is how to calculate the sensitivity of the objective function. Because the topology function of each unit element is a binary function that only contains two states, the derivative of the function is hard to be evaluated, and hence in actual applications finite difference method is often used to derive the sensitivity of unit elements [B27]. However, applying finite difference method leads to a longer evaluation process and hence results in a longer optimization time.

2.1.4 Boundary Variation Method

Beside the discretized methods discussed in the previous parts of this section, the topology of the devices can also be modelled in a continuous manner. To do so, the boundaries of different types of material are tracked during the optimization process, using the positions of the nodes on the boundaries, and shape functions that describe those positions. Compared to the discretization methods, often a smaller number of design parameters is required to represent the topology in the boundary variation methods, as the number of boundary elements is less than the number of elements in the entire design domain. Hence, in recent years more and more researches have been carried out on the study and development of suitable boundary variation methods in topology optimizations [B28-B29]. Generally, there are two well-practiced boundary variation methods, namely the level-set methods, and the phase field methods. The

former one has a wider scope of applications and has been utilized to optimize actual problems in the fields of mechanical engineering, electromagnetics engineering, civil engineering and so on, while the latter one mainly focuses on fluidic problems.

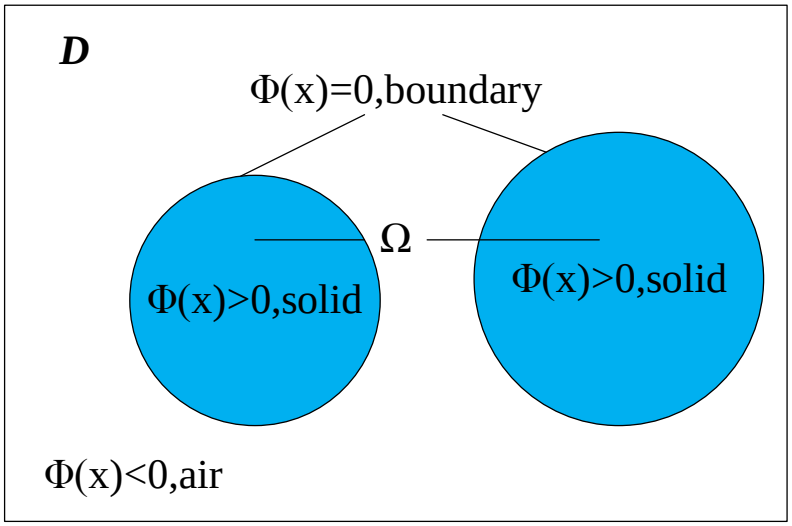

Fig. 2.3. Schematic representation of the level-set function and method.

In the level-set modelling method for a two-state problem, a scalar function, Φ, called the zero-level contour, or the level-set function, is used to model the contour of a solid material, as depicted in Figure 2.3. The overall design domain is denoted by D, where the topology of the device lies. The material domain is denoted by Ω, and its boundary is represented by $\partial\Omega$. The reason the boundary, $\partial\Omega$, is called a zero-level contour is due to that if we have a material distribution function, $\Phi(x)$, the solid region, void region and the contour can then be represented as:

$$\begin{aligned} &\Phi(x) > 0, x = solid; \\ &\Phi(x) = 0, x = boundary; \\ &\Phi(x) < 0, x = air;\ \forall x \in D \end{aligned} \tag{2.4}$$

By tracking the change of the contour where $\Phi(x) = 0$, the change of the topology of the solid region within the design domain, as well as the merge of different solid region and the creation of void region can be described. Because the evaluation of the objective function in most of the applications still heavily relies on the FEM with the aid of computers, and the topology is often discretized into small mesh elements, in the actual applications of the level-set method, the eventual boundary

obtained from the optimization process is likely unsmooth [B29], as the edge elements may not form smooth boundaries. For instance, in the early part of the section the combination of the level-set method and the ON/OFF method is described, and the boundary obtained required further smoothing process [B27]. The most important function in the level-set method is the level-set function. Generally, with the design parameter represented by s, this function can be defined as [B30]:

$$\Phi = \Phi(x, \Psi(x, s)), \forall x \in D \tag{2.5}$$

Here the function $\Psi(x, s)$ is an auxiliary function or basis function that is used to model the topology, and controlled by the design parameters s. Hence, the parameterization of the level-set methods depends on the choice of basis functions and the choice of the optimization variables. The simplest form of the level-set function discards the usage of the basis function, i.e., $\Psi(x, s)=1$, and then the level-set function reduces to $\Phi = \Phi(x, \mathrm{s}), \forall x \in D$, where the coordinate of the boundary nodes is used as the design parameters [B30]. Using this manner, the level-set method is straightforward, and however the number of design parameters may be high, and sometimes could be inconsistent when there is merging of region or creation of void. Employing basis function can reduce the influences from these problems, and the most well-practiced basis functions are the radial basis functions [B31-B32] and other spectral functions [B33]. The size of the basis function is often small, for instance in the radial basis function, the radius of each basis function is only few mesh elements, and hence via the summation operation, only small movements of the boundary of different types of materials can take place during the optimization process [B34-B36], ensuring a local effect of each design parameter and hence a more detailed exploration of the design space, as well as a finer boundary in the final topology obtained.

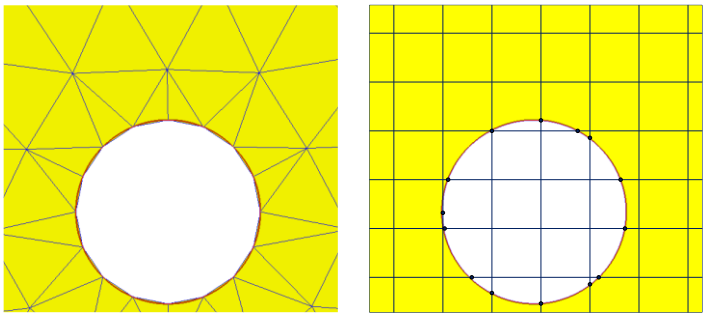

(a) (b)

Fig. 2.4. Schematic representation of (a) conforming discretization mapping and (b) immersed boundary technique [B30].

Another important procedure in the level-set method is the mapping from the numerical level-set function to the actual topologies and shapes in the FEM evaluation process. If the shape and size of the mesh elements in the FEM process are allowed to vary according to the boundaries evolvement in the level-set method, such as in the extended finite element method (XFEM), a good and accurate boundary can be represented using a method such as the conforming discretization [B37-B39], where only the material domain is modelled, or immersed boundary techniques [B40-B42], where boundary conditions are enforced locally at the interface between the solid material and the void region. The graphical representation of these two methods is given in Figure 2.4. However, applying changes to the mesh elements incurs extra computational costs and procedures and extends the optimization time, as well as increases the modelling difficulties, especially in 3-D modelling. Hence, fixed mesh is more preferred during the optimization process. Using a fixed mesh element, the most straightforward mapping method is the direct density approach, using a smooth Heaviside function with bandwidth h [B30]:

$$\rho_e = \varepsilon + (1-\varepsilon)\tilde{H}(\Phi(x_e))$$

$$\tilde{H}(\Phi(x_e)) = \begin{cases} 0 & \text{for } \Phi < -h \\ -\frac{1}{4}\left(\frac{\Phi}{h}\right)^3 + \frac{3}{4}\left(\frac{\Phi}{h}\right) + \frac{1}{2} & \text{for } -h \le \Phi \le h \\ 1 & \text{for } \Phi > h \end{cases} \tag{2.6}$$

Here, ρ_e represents the density of each element and ε is an arbitrary constant that is close to zero and used to avoid a numerical singularity [B30]. Similar to a discretized

modelling method, in the density-based mapping of the level-set method, the topology of the device is discretized into small elements, and the level-set function is element-wise mapped into the topology of the device with different material density. This approach is easy to be implemented, and the continuity in the material density in the topology makes the derivation of gradient information more convenient [B43-B46]. However, the grayscale problems and crispy boundaries that occur in the SIMP method occurs in here as well. Exact Heaviside function has been used to replace its smoothed counterpart in [B47-B48], and one drawback is that the derivation of the gradient information is hard to be implemented. Other than that, trigonometric functions [B49-B50], other types of smoothed Heaviside functions have also been applied in [B51-B54], and similar performances are obtained.

The updating of the level-set function during iterations decides the direction of evolvement of the material boundaries. This evolvement is often governed by the Hamilton-Jacobi (H-J) equation, which is written as:

$$\frac{\partial \Phi}{\partial \tau} + \nabla \Phi \bullet v = 0 \tag{2.7}$$

In the H-J equation, τ denotes the pseudo time step, for instance the iterations in the optimization process, and v denotes the virtual velocity of the evolvement. Because the evolvement of the boundary always lies in the normal direction, using the normal velocity, $v_n = v \bullet \mathrm{n}$, and outward norm, $\mathrm{n} = \frac{-\nabla \Phi}{\|\nabla \Phi\|}$, of the boundary or nodes on the boundary, equation 2.7 can be simplified into [B30]:

$$\frac{\partial \Phi}{\partial \tau} - v_n \|\nabla \Phi\| = 0 \tag{2.7a}$$

The virtual velocity of the boundary evolvement is determined by the topology sensitivity. For a density mapped level-set function method, consider a variation in the boundary $\delta\Omega$ caused by change in the design parameter δs_i , let the level-set function be $\Phi = \sum_i N_i \delta s_i$, which is the most common form of level-set function parameterization [B55], for the material boundary where $\Phi = 0$, the following equation can be obtained:

$$\sum_i N_i \delta s_i + \nabla\Phi \bullet \delta\Omega = 0 \tag{2.8}$$

Solve the normal component boundary variation, $\delta\Omega_n$:

$$\delta\Omega_n = \sum_i \frac{N_i \delta s_i}{\|\nabla\Phi\|} \tag{2.8a}$$

Hence, integrating over the entire boundary, Γ, of the material domain and using $d_S R$ to denote the gradient of shape [B56], the discrete shape sensitivity can be formulated as:

$$\frac{\partial F}{\partial s_i} = \int_\Gamma d_S R \frac{N_i}{\|\nabla\Phi\|} dS \tag{2.9}$$

If the boundary is not explicitly represented, the above equation is hard to measure, and hence the chain-rule is applied to solve the elementwise sensitivity. The sensitivity is analyzed as the derivative of the objective function to the control variable, s_i for each element [B57]:

$$\frac{\partial F}{\partial s_i} = \sum_e \frac{\partial F}{\partial \rho_e} \frac{\partial \rho_e}{\partial s_i} \tag{2.10}$$

Here ρ_e denotes the material density which is controlled by s_i of each element e. The sensitivities are zero for non-boundary elements, and *vice versa* [B58]. The obtained sensitivity information is then used to update the virtual velocity of the boundary, v in the equation [B55]. To smooth the level-set function, reduce the dependency of the obtained topology with discretization of the level-set function, and regularize the level-set function so that the level-set function values in the solid region are unique, a second-order diffusive term, which can be both isotropic and anisotropic, is added to the H-J equation [B59-B60]. Moreover, one issue with the H-J equation is the lack of void creation mechanism, and hence a reaction term [B61-B63] that can fit this problem or term derived from the topological derivative method [B64-B66] is added to the original H-J equation, the topological derivative is defined as the change of the objective function subject to the addition of an infinitesimal void, $B(r)$ [B63]:

$$d_\Gamma F = \lim_{r \downarrow 0} \frac{F(\Omega \setminus B(r)) - F(\Omega)}{|B(r)|} \tag{2.11}$$

From the formulation and derivation of the level-set method, it can be seen that because the update of the level-set function is highly dependent on the sensitivity or gradient information, the level-set method can naturally work well with gradient-based optimization algorithms, for instance, the optimality criteria methods [B67], the sequential quadratic programming method [B68], and the method of moving asymptotes [B69]. When applied together with gradient-free methods, the evaluations of the gradient information are based on the discretization of level-set function and the finite difference method [B70], and hence heavy computation time is required which limits the usage of the level-set method in gradient-free optimization algorithms.

Another type of continuous modelling method is the phase field method, which is developed originally to describe solid-liquid phase transition in liquid fluidics [B30]. Very similar to the level-set method, the phase field method uses the phase field function to describe the topology of the device for a two-state problem, as depicted in Figure 2.5. The phase transition region is represented by the gridded area with a width of ξ, and the two phase-constant regions are marked by A and B, with a constant phase field function value of α and β.

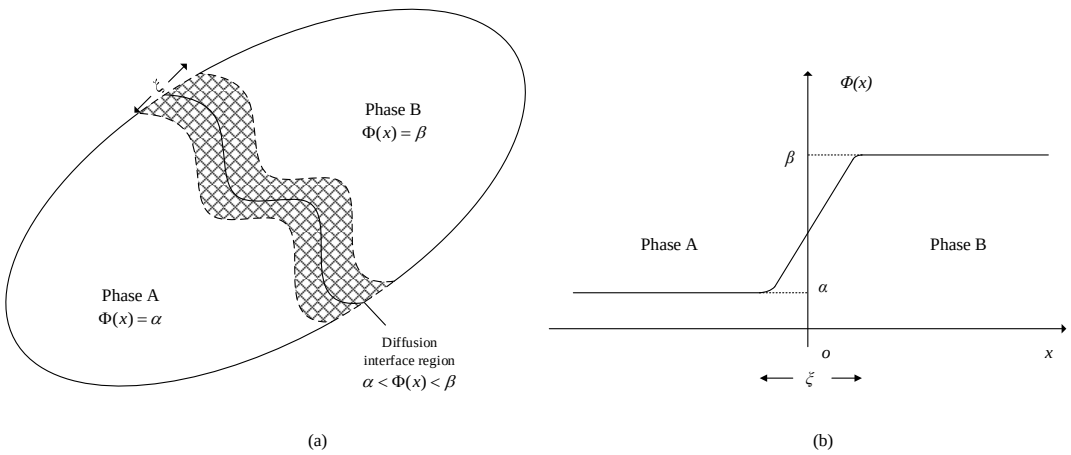

Fig. 2.5. Schematic representation of (a) 2-D phase field representation of domain and (b) 1D phase field function [B30].

The first application of the phase-field method in topology optimization is in 2003 [B71] and has been adopted in structural optimizations afterwards [B71-B73], using the van der Waals-Cahn-Hilliard phase transition theory and generalized Cahn-Hillard equations. The main difference between the phase-field method and the level-set

method is that the entire design domain, rather than solely the boundary interface between phases, is tracked during the optimization process in the phase-field method. Instead of the material boundary, Γ, the governing equation is solved for the entire design domain Ω. Hence, there is no requirement of *a prior* knowledge related to the location of the boundary between the two phases. However, as the governing equation is solved for the entire design domain, the computation process might take a longer time when compared with the level-set method.

2.1.5 Surrogate Model and Metamodel

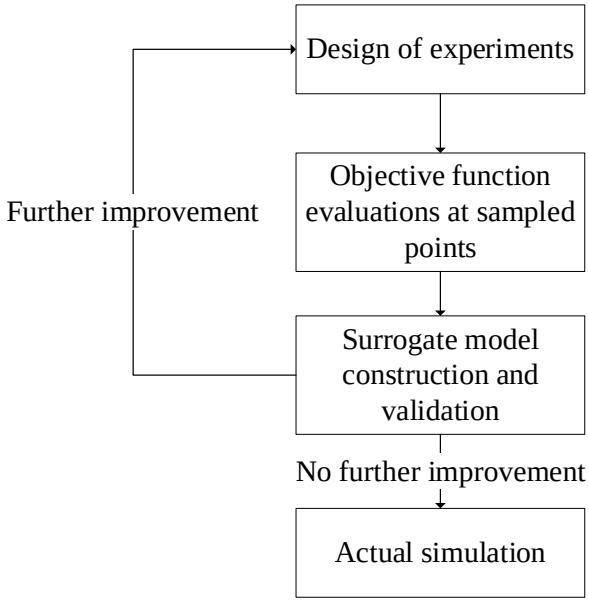

Fig. 2.6. Workflow of surrogate model construction [B76].

In the optimization process, the evaluation of the objective function values always takes the longest time. In certain engineering problems, especially in multi-physics problems with 3-D structure, the FEM simulations can be extremely time consuming, or the evaluations of the derivative are tedious, the optimizations might require excessive computational resources and hence become infeasible. To speed up the objective function evaluation process, surrogate models that can estimate the objective function with much shorter time have been developed to assist the conventional numerical evaluation process such as the FEM process [B74-B75].

To construct a surrogate model for the optimization problem, first a number of

numerical experiments are conducted. Based on the design parameters and the objective values obtained, using certain interpolation functions, the surrogate model $\hat{f}(x_e)$ of the original objective function $f(x_e)$ can be constructed and be used to estimate the objective function values in the following optimization process. The workflow of the construction of surrogate model is given in Figure 2.6 [B76].

The design of experiment process constructs an initial connection between the object function values and the design variables. The design parameter space is sampled with several sample points, and the objective function values of these sample points are evaluated. The surrogate model is then constructed based on an interpolation of these sampled design points and their corresponding objective values. Hence, the sampling plan strongly affects the accuracy of the surrogate model obtained. The most well-practiced sampling plan is the Latin-hypercube sampling method (LHS). The method was originally proposed in 1979 [B75], and soon found its applications in design-of-experiments. Considering an optimization problem with K design variables, each input vector of design variables can be represented by x_k, $k = 1, 2, 3, \ldots, K$. To sample N_s sampling points, the range of each design variable is evenly sectioned into N_s strata with marginal probability of $\frac{1}{N_s}$, each stratum is sampled once randomly and hence a total of N_s samples are chosen from the design domain. Figure 2.7 depicted the sampled points chosen by LHS method when $K = 2$ and $N_s = 4$. One issue with the LHS is that the difference between two sample results from the same design domain could be highly different, and there is a lack of uniformity in the sampling patterns [B77]. To address this issue, methods such as the orthogonal array based LHS have been proposed [B78-B80].

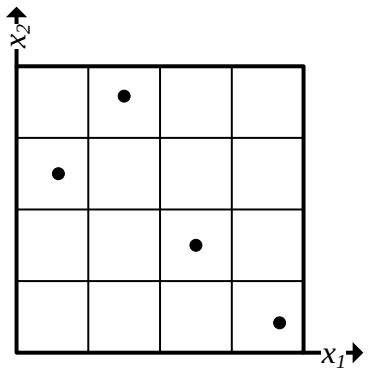

Fig. 2.7. Example of LHS sampling with two parameters and 1/4 sample ratio.

After the DoE process, based on the objective function values and the sampled points, certain interpolation methods are applied to obtain the surrogate model. The interpolation method can be either in global scale, such as the polynomial regression model, or in local scale such as the compactly supported radial basis function (RBF) method with eventual summation, with each having its own *pros* and *cons*.

The polynomial regression model can be described as [B81]:

$$f_i(z) = \sum_{j=1}^{N_{PRG}} \beta_j z_j^{(i)} + \varepsilon_i, \quad E(\varepsilon_i) = 0, \quad V(\varepsilon_i) = \sigma^2 \tag{2.12}$$

Here, N_{PRG} stands for the number of basis-functions, z_j stands for the particular basis function in that order, i represents the order of the basis-functions, β represents the coefficient and ε_i represents the error term. Polynomial regression can be regarded as the most straightforward form of interpolation techniques and is relatively easy to implement. However, to construct an accurate surrogate model often a high order polynomial regression model is necessary. With many design parameters, the complexity of the model may be too high to be realized.

The Kriging method, which is named after the South African mining engineer D. G. Krige, was formally formulated by Matheron [B77]. The ordinary Kriging predictions contain two parts: the linear model and the error term representing the fluctuation. For a simple Kriging with n sample points and m linear basis-functions, the model can be written as [B81]:

$$\hat{f}(x) = \sum_{i=1}^{m} w_i f_i(x) + \varepsilon(x), \quad E(\varepsilon(x)) = 0 \tag{2.13}$$

where w_i stands for the weight coefficients, $f_i(x)$ s are the m predefined basis-functions, and $\varepsilon(x)$ represents the error function with mean of zero. The Kriging predictor can be written as [B81]:

$$\hat{f}(x) = f(x)^T \beta^* + r(x)^T \gamma^* \tag{2.14}$$

Here, $f(x) = [f_1(x), f_2(x), f_3(x), ..., f_m(x)]^T$ and β^* is the generalized least-square estimate of $\beta = [\beta_1, \beta_2, \beta_3, ..., \beta_m]$, $r(x)^T$ is the correlation vector of size $n \times 1$ between $\varepsilon(x)$ and $\varepsilon(x^{(i)})$. β^* and γ^* are:

$$\begin{aligned} \beta^* &= (F^T R^{-1} F)^{-1} F^T R^{-1} y \\ \gamma^* &= R^{-1}(y - F\beta^*) \end{aligned} \tag{2.15}$$

where R represents the covariance matrix ($n \times n$) of all error correlations and y represents the objective function values of all sampled points. Based on different regression models $f(x)^T \beta^*$ and correlation models R, various types of Kriging, such as the ordinary Kriging [B82], blind Kriging [B83] and penalized likelihood Kriging [B84] have been proposed. In the comparison research of Jin et. al [B85], they revealed that the addition of high order complex terms in the regression model would increase the complexity, as multimodal maximum-likelihood function would occur, though not significantly affecting the accuracy of the Kriging predictor. Furthermore, as the computation of the inversion of the covariance matrix is highly related to the number of samples, constructing a Kriging model from a large amount sample points is numerically difficult. To solve this problem, methods of breaking down the covariance matrix into smaller matrices [B86-B87] or using the sparse matrix [B88] have been proposed and proved to be efficient.

The radial basis function method (RBF) uses a weightage sum of simple functions to represent and reconstruct the complicated device topologies. Numerically, the RBF with N_{RBF} radial symmetric functions $h_i(x)$, normally based on the Euclidean distance between the centre and the points in space, and can be formulated as:

$$f_P(x) = \sum_{i=1}^{N_{RBF}} w_i h_i(\|x - c^{(i)}\|) + \varepsilon_i \tag{2.16}$$

where w represents the weighting factor, $c^{(i)}$ represents the center of the ith basis function, and ε_i represents the independent error terms. The basis-functions can be directly simple functions, such as linear, quadratic, or cubic functions, or complicated functions such as the Gaussian RBF and multi-quadratic functions [B79]. There is no solid conclusion about how the complexity of the basis-function can affect the accuracy of the model constructed. Also, the RBF methods have been extensively used in the design and optimization processes for acceleration purposes [B89-B90], due to their good flexibility.

2.2 Optimization Algorithms and Methods for Topology Optimization

The choice of the optimal algorithm is another key factor determining the optimization speed. Based on the complexity of the problem and the availability of the derivative information, either the gradient-based or the gradient-free algorithms can be employed to optimize the problem. The gradient-based algorithms have been developed for more than one hundred years and have been proved to have a fast convergence speed with the aid of the gradient information of the objective functions. However, as the design and optimization problems nowadays become more and more complicated, and there are problems that the analytical expressions of the governing equations of the system are hard to be derived, the gradient-free algorithms which based on heuristic searching have also played significant role in optimizations, especially topology optimizations in various engineering disciplines.

2.2.1 Gradient-based Algorithms

The gradient-based algorithms employ the calculated or estimated gradient information to guide the evolvement directions of the device topology. The commonly practiced gradient calculation methods include [B91]: (1) Perturbation Analysis, (2)

Likelihood Ratio/Score Function, (3) Frequency Domain Analysis. The gradient method developed using these methods can be applied together with classical optimization algorithms such as the Newton's method or the steepest descent methods to search for the local optimum. However, the applications of these methods always couple with certain pre-requisite in the problems involved and certain application difficulties [B92], and hence do not find a wide application in engineering.

To estimate the gradient information rather than directly evaluate it, the most widely adopted method is the finite difference method, as the method naturally works well with the FEM in simulations. The forward finite difference derivative of the objective function with respect to the ith design parameter can be described as:

$$f'(x_{(i)}) \approx \frac{f(x_{(i)} + \Delta x_{(i)}) - f(x_{(i)})}{\Delta x_{(i)}} \tag{2.17}$$

A small perturbation $\Delta x_{(i)}$ is added to each design parameter to evaluate the change in the objective value and the corresponding gradient, and total $n+1$ evaluations are required for n design parameters, which can be computationally expensive when the dimension of the problem is large. To solve this issue, the simultaneous perturbation stochastic approximation algorithm (SPSA) that utilizes a vector of random perturbations has been proposed [B93]. For an iterative optimization problem with solution vector x of n design parameters, the gain of a_k and the directional vector of $g(x_k)$, the optimization problem can be formulated as [B93]:

$$\begin{aligned} &\min_{x \in R^n} F(x) \\ &x_{k+1} = x_k - a_k g(x_k), a \in R_+, g(x_k) \in R^n \end{aligned} \tag{2.18}$$

The vector perturbation is used to calculate the search direction $g(x_k)$:

$$g(x_k) = \frac{F(x_k + c_k r_k) - F(x_k - c_k r_k)}{2c_k} r_k^{(-1)} \tag{2.18a}$$

Here, c_k and r_k are the positive coefficient and unit random vector added to simulate the perturbation in the system. The SPSA method is very similar to the center finite difference method, except the finite difference is no longer imposed to a single design

parameter, but to the entire input vector. To further improve the accuracy of the SPSA method, Monte Carlo sampling [B94], improved Jacobian and Hessian estimates [B95] have been injected to the SPSA.

2.2.2 Direct Search Methods

The direct search methods do not require the gradient information and hence are much more convenient to be implemented when compared with the gradient-based method. In the direct search methods, the objective values of selected candidates are compared, and the search direction is then determined. The most well-accepted direct search methods are the pattern search method and the Nelder-Mead simplex procedures [B91]. The pattern search method was proposed in 1961 by Hooke and Jeeves [B96] and has been proved to be always able to converge to an optimum [B91]. There are two main steps in the pattern search methods, namely the exploratory search step and the pattern move step. Consider a design space with *n* dimensions, in the exploratory step a perturbation vector, $P_0 = [\Delta x_1, \Delta x_2, \Delta x_3, ...\Delta x_n]$ is first generated in the initialization step with all elements in the vector are relatively small. For each design parameter in the current design $x^{(0)}$, increase its value by the perturbation value Δx_i one at a time, and evaluate the objective function value of the changed design, and a total of *n* times of objective function evaluations are required. Based on the evaluated values, the design parameter with the best objective function value improvement is identified, and the direction of improvement is then the corresponding to Δx_{best} value, $P_{direction} = [\Delta x_{best}, \Delta x_{best}, \Delta x_{best}, ...\Delta x_{best}]$. The design is then updated in the pattern move step. In the pattern move step, the current design $x^{(0)}$ is updated to $x^{(1)}$:

$$x^{(1)} = x^{(0)} + aP_{direction} \tag{2.19}$$

where *a* is a positive acceleration coefficient. The objective function value of the new point is then evaluated and compared with the old one. If there is an improvement, jump to the next iteration, otherwise repeat these two steps. The main drawback of the pattern search method is that for each step total *n+2* objective function evaluations are

needed, and hence the process has a low optimization speed [B91]. The Nelder–Mead simplex procedure developed by Olsson and Nelson [B97] is very similar to the pattern search method. For an n dimension problem, $n+1$ samples are chosen, and a simplex is formed. Then certain transformations are conducted to the simplex, for instance the averaging, centroid or shrink processes, and new points can be obtained. Based on the objective values of these points, then update the simplex in the direction of the best objective values until no more improvement. There is a limited usage of the direct search method [B91], mainly due to the reason of overwhelming computation burden and sometimes not able to converge globally.

2.2.3 Genetic Algorithms

Genetic algorithm (GA) is the most studied random search algorithm that based on the population evolution mechanism [B98]. The algorithm was first mathematically proved in 1975 and was proposed to imitate the natural evolution process of species in Darwin's evolution theory, as the name suggests. The flowchart of the conventional GA is depicted in Figure 2.8.

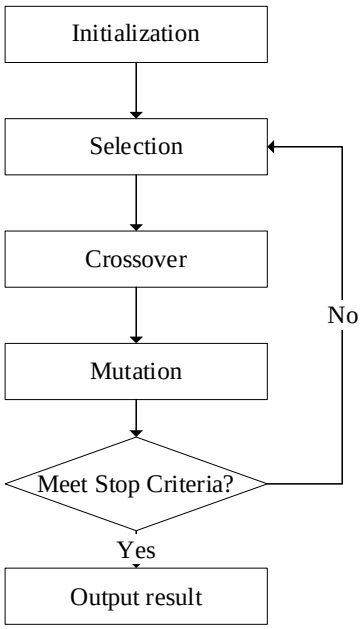

Fig. 2.8. Workflow of GA.

Each possible design is encoded by an array of genes that represent the design parameters of that design. The initialization step determines the algorithm parameters,

including the population size, N_s, the parents and children ratio in each iteration, the crossover mechanism, and the mutation probability. Moreover, an initial population is randomly generated. Followed by the initialization, the population is then sorted based on their objective values, and the first few candidates are chosen to be parents of the crossover process, and the number of parents is determined by $N_s \times P_p$, where P_p is the parents ratio. In the crossover process, to generate a child two parents are randomly chosen from all available parents based on certain predefined metric, such as the roulette wheel method [B98]. The two parents then reproduce one child based on the crossover mechanisms, such as weightage sum, string randomly concatenate or logical operation. This selection and crossover process repeats for $N_s \times P_c$ times, where P_c is the ratio of children in the population. Hence, the sum of the number of the parents and the children is equal to N_s and can be used as the population for the next generation. To avoid being trapped in a local optimum and add variations to the population, mutation takes place with probability of P_m, which is a relatively small number, in each iteration. The mutation can happen either in the crossover process, where a random gene is used to replace the gene in the child, or can happen in the population level, where a random candidate is added to the population to replace the one with low objective value. The crossover and mutation repeat until the stop criteria are met. The main drawback of the original GA was the large time consumptions of the algorithm. Because in each iteration the entire population is evaluated using FEM, and some of the individuals in the population have relatively low objective values that do not contribute to the searching process, certain computation resources are actually wasted. To solve this problem, a fast GA, where the initial design space is narrowed down by considering the minimum and maximum errors of each individual, has been proposed [B99]. Adaptive algorithm parameters are employed as well to further remove the redundant FEM evaluation processes and accelerate the optimization speed. These include the self-adaptive model GA where all algorithm parameters vary as the optimization progress [B100], the self-organizing GA where a periodical mutation rate is employed [B101], the adaptive selection and crossover mechanism [B102-B103].

Furthermore, because of the advent of parallel computing technologies, the population can be divided into different sub-groups for parallel computing purposes and to make the adaptive parameters easier to evolve as well [B104-B106]. Furthermore, the genes in conventional GAs are binary coded into only 2 states, which imposes a big restriction to the application of GA. Hence the quantum GA and immune GA have been proposed [B107-B108] and been proved to be more efficient than other types of GAs and other population-based algorithms. GA can also be applied to solve multi-objective optimization problems, with the aid of certain improvements to the algorithms. The traditional multi-objective GA uses a weightage sum to aggregate the multiple objective function values into one value, and then treat the problem as a simple single objective function problem. However, in certain occasions the objective functions may be contradictory, and the results obtained by this method may not be meaningful, and hence the non-dominated GA (NSGA-II), a multi-objective optimization algorithm, has been proposed in 2002 and has been widely applied to solve multi-objective problems [B109]. In NSGA-II, all the individuals that have at least one objective value not worse than all other candidates, which is also regarded as non-dominated, are listed out as the final solutions, and hence a non-dominate front can be obtained as the optimization results. Due to their nature of easy implementation, both GA and NSGA-II have been extensively applied in electromagnetic problems, with the aid of either discretization modelling [B110-B111], or the level-set method [B112].

2.2.4 Particle Swarm Optimization Algorithms

In a genetic algorithm, the searching information is only carried on from generation to generation via the crossover process, and the sharing of information only takes place between the parents and the children and relatively limited. To solve this problem, another type of evolutionary algorithms, namely the memetic algorithms are proposed and developed. In the memetic algorithms, the searching information, and searching directions, which are the memes in the population, are spread throughout the entire population, and hence the searching is more directed and effective when

compared with other types of evolutionary algorithms.

The particle swarm optimization algorithm (PSO) is one of the most studied memetic algorithms proposed in 1995 [B113]. Similar to all other evolutionary algorithms, PSO is also based on a large population of possible designs and their corresponding evolvements. Each design is associated with two parameters, its position and velocity. The position marks its current values of design parameters and the velocity determines its movement direction for the next iteration. Consider a *n*-dimensional optimization problem, at the kth iteration, the velocity and position of a design for the next iteration $k+1^{\text{th}}$ can be formulated as:

$$\begin{aligned} v_i^{k+1} &= wv_i^k + \text{rand}[0,1]\bullet c_1\bullet(p_i^k - x_i^k) + \text{rand}[0,1]\bullet c_2\bullet(p_g^k - x_i^k) \\ x_i^{k+1} &= x_i^k + c_3 v_i^{k+1} \end{aligned} \tag{2.20}$$

Here, v_i^n and x_i^n indicates the velocity and position of the ith candidate in the population in the kth iteration, w is called an inertia weight, c_1, c_2 and c_3 are the numeric coefficients, p_i^k is the best previously visited position of the ith candidate and p_g^k is the best previously visited position of the entire population. The inertia weight controls the balance between exploration and exploitation of the searching process. Numerically the inertia weight can be expressed as [B98]:

$$w^n = w_{\max} - \frac{(w_{\max} - w_{\min})n}{iter_{\max}} \tag{2.21}$$

where $w_{\max}$ and $w_{\min}$ are the maximum and minimum inertia weight, n is the iteration number and $iter_{\max}$ is the maximum iteration number defined before the optimization. The progress of PSO is illustrated in Figure 2.9. PSO imitates the process of swarm searching for food. The fitness value of a particle in the swarm indicates the amount of food available at that specific position, and hence the higher the fitness value, the more the food can be found. Because the fitness information is shared among the population, the individuals in the swarm tend to move towards the individual with the best fitness value, and hence the exploration of the entire design space can be conducted. Moreover, the addition of the best visited value of each particle allows the

searching to exploit information around promosing particle.

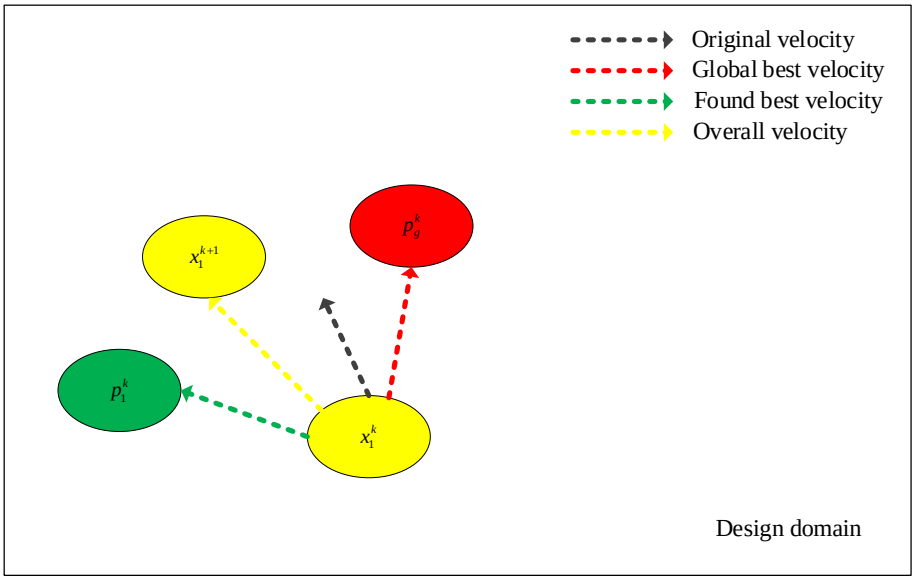

Fig. 2.9. Graphical representation of PSO.

The development and improvement of PSOs mainly focus on developing appropriate algorithm parameters, such as the weight inertia, the weight coefficient of the global best velocity and local best velocity, the step size etc. The inertia weight coefficient directly affects the balance between exploration and exploitation of the algorithm, and hence needs to be varied as the algorithm progress. To do so, linearly, and non-linearly decreasing inertia [B91, B114] have been proposed to sequentially change the inertia value. Moreover, a dynamically varying inertia weight based on the aggregation degree and evolution speed [B115], and time-varying decreasing inertia [B116], were introduced to further strengthen the exploitation of the design space at latter iterations of the optimization. In the conventional PSO algorithm, only the global best candidate can affect the entire population, for complex problems this may sometime weaken the exploitation ability of the algorithm and hence the optimization may take a long time. Hence in [B117] the γ best particles are used to calculate the speed of each candidate, rather than solely the best candidate, and γ gradually decreases as the optimization progress. Furthermore, the learning mechanism is changed from linear summation to an orthogonal learning strategy, which makes the searching process more efficient [B118]. To avoid being trapped in the local optima a

mutation operator is added to PSO as well [B119], and vibrational multi-frequency PSO that utilizes an artificial neural network to control the variety of the population [B120] have been developed. The PSO with varying an acceleration coefficient is one of the most efficient versions of PSO [B98] in terms of robustness, and all the algorithm parameters are adaptive, allowing exploration at early stage and exploitation at late stage. More algorithm parameters have been added to PSO, including novel tunning method [B121], sensitive parameters and social learning rates [B122], to foster a larger diversity in the swarm. The PSO was originally proposed to handle continuous problems [B91], and in engineering applications as the control parameters are however often discrete, a direct application of PSO may be difficult and inappropriate. Hence in [B123-B124], the discretized version of PSO has been proposed, where a binary representation of candidates was employed.

Similar to GA, PSO is also developed initially solely for single objective problems. Its multi-objective counterparts can be divided mainly into four types [B99]: methods treat each objective function separately; weightage sum methods; objective ranking method and lastly the Pareto optimal methods. If the objective functions are treated separately, the optimization results often contain multiple designs which are non-dominant. However, the time taken for such methods is quite long as the number of objective evaluations is large, and there is a need to pre-determine the relation between objective functions so that non-dominated solution can be converged [B91]. The objective function ranking method performs similar as well. Despite the fact that these two methods are convenient to use, they are inappropriate for complex black-box problems. Moreover, for objective ranking method the sensitivity of each objective function is evaluated, and hence enlarger the time taken for optimization. The weightage sum method cannot detect optima for concave problems [B125], and hence other types of weightage methods such as the dynamic weightage sum methods are proposed. The weightage coefficients, $w_1(t)$ and $w_2(t)$ of a binary objective function problem can be formulated as [B126]:

$$w_1(t) = \left|\sin(\frac{2\pi t}{a})\right|, \qquad w_2(t) = 1 - w_1(t) \tag{2.22}$$

where a is constant and t is the iteration number. Via adaptive weightage coefficients, the algorithms are able to converge to non-dominated front that obtained by other multi-objective algorithms such as NSGA-II, with a comparable performance [B126].

The Pareto-based PSO algorithms are the most extensively studied multi-objective PSO. The first Pareto-based PSO was proposed in 2002 [B126]. As multi objective functions occur, it is very hard to decide which candidate is the global best candidate. Hence, a repository of non-dominated solutions is formed at the end of each iteration during the optimization process, and the global best solutions for updating velocity is chosen from this repository. To decide which solution to be chosen, the roulette wheel method, the hypercube method [B126], the dominated tree method [B127] and the nearest neighbor density estimator that uses the non-dominated solution with the nearest Cartesian distance in the design space have been used [B128]. Moreover, using the number of neighbors, the *elite* solutions have been added and deleted from the archive of the Pareto solution respectively [B128]. Other than that, a sigma function based multi-objective PSO that utilize sigma function to decide from the archive of the *elite* has been proposed [B129]. For a bi-objective function problem, the sigma function can be defined as [B91]:

$$\sigma = \frac{(K_2 f_1)^2 - (K_1 f_2)^2}{(K_2 f_1)^2 + (K_1 f_2)^2} \tag{2.23}$$

where K_1 and K_2 are the maximum values of function f_1 and f_2. The method performs well for bi-objective problems by outperforming the benchmark strength Pareto evolutionary algorithm (SPEA2) but does badly for problems with more than two objective functions. In the sub-swarm techniques, the entire swarm is divided into subswarm based on initially estimated Pareto front [B130]. The method has fast convergence rate and ability to locate the final Pareto front [B91]. A survey of the effects of all algorithm parameters, such as the inertia weight, coefficients was given in [B130], and the conclusion revealed that large values of the inertia weight and the acceleration coefficient of the global best yields the best algorithm performance [B130].

2.2.5 Evolutionary Structural Optimization Algorithms

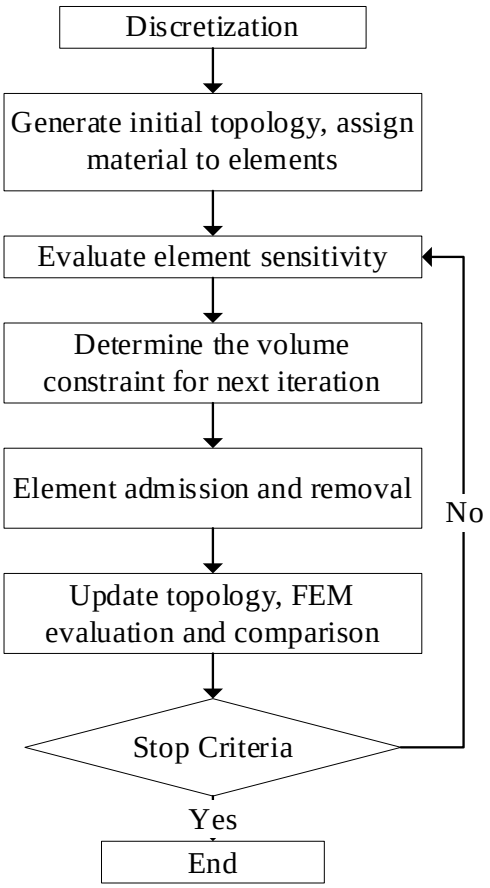

Fig. 2.10. Workflow of the bi-directional-ESO.

The Evolutionary structural optimization algorithm (ESO), bi-directional ESO, and the sequential element removal and admission (SERA) are the simplest and most efficient "hard-kill methods" that were developed for topology optimizations in 1993 [B29]. The design domain is discretized into small elements, similar to the ON/OFF method, and the elements in the solid region are sequentially inserted to or removed away from the current design until the stop criteria are met. Due to the discretization of the design space, the method naturally works well with FEM analysis and hence showed great number of applications in engineering problems. In the original ESO, only element removal can take place, and hence the obtained topology highly depends on the initial guess. In the SERA, which can be regarded as an extension of ESO, an admission process is included as well. The workflow of ESO/SERA is depicted in Figure 2.10. After the proper discretization of the design space via FEM, an initial

guess is generated as the root topology of the optimization process. The sensitivity of each element is then evaluated, either using an analytical method or using a finite difference method explained in the previous section. Based on the sensitivity, all the solid elements and void elements are sorted. Then based on the target volume of the next iteration, the solid elements with the lowest sensitivity is removed from, and the void elements with the highest sensitivity is added to the topology of the design [B29]:

$$\begin{aligned} &\alpha_i \le \alpha_{del}^{th},\ i^{th}\text{element removal} \\ &\alpha_i > \alpha_{adm}^{th},\ i^{th}\text{element admission} \end{aligned} \tag{2.24}$$

The threshold sensitivity, α_{del}^{th} and α_{adm}^{th}, are normally set to be equal to the median sensitivity value of the entire design domain. To reduce the computation time of the sensitivity values, in [B131] only the void elements next to the solid region are considered for sensitivity analysis, making the ESO method more like a boundary evolvement method with an ability to generate holes in solid regions. ESO, BESO and SERA have been widely applied in vibration problems, stress problems and rigidity problems and so on, where the governing equations are available [B132-B135]. In [B136], the solid material is replaced by orthotropic cellular microstructures to avoid artificial modes for dynamic problems; and in [B137], additional smoothing technique is employed to remove the checkerboard pattern. The multi-objective version of BESO have been proposed in [B137-B138], and it was proven that the multi-objective BESO performs better in compliance and frequency optimization problems.

Besides their ease in applications, ESO/BESO and SERA face several disadvantages [B139-B140]. The first is the difficulty in determining the stop criteria [B29]. The commonly practiced method is stopping the algorithm when the volume constraint is met or when there is no improvement in the objective values for several iterations. However, as there is a lack of a local optima escaping mechanism, there is no guarantee that the found optimum is the global one. Process such as mutation [B139] is added to the BESO algorithm, but this increases the computation cost. Another issue is the dependency on the initial guess, as the evolvement of the topology is always base on the initial topology, and hence with *prior* knowledge the algorithm converges fast, and *vice versa*. Moreover, the need to calculate sensitivity information requires

tremendous amount of FEM evaluations using the finite difference method, and the method becomes complicated for multi-material optimization problems. ESO/BESO mainly showed successful applications in the mechanical problems, where the analytical governing equations are available. In terms of electromagnetic optimization problems where multiple materials are involved, there is a limited application of ESO/BESO methods.

2.2.6 Other Stochastic Search Algorithms

There are numerous types of random search algorithms, either based on population evolvement or based on the single candidate, and some of them have been successfully applied to engineering problems. The working principles, application scope and *pros* and *cons* of these algorithms will be reviewed.

(1) Differential Evolution Algorithm

The differential evolution algorithm (DEA) is developed to tackle optimization problems that are non-linear, non-convex, multi-dimensional and non-differentiable [B141]. Very similar to other evolutionary algorithms, the conventional DEA contains three progresses: mutation, crossover, and selection. Assuming the initial population contains N_P possible designs evenly distributed in the design domain and each design is a vector of *m* elements, in the mutation process, a mutant/donor is generated as:

$$v_i^t = x_{r1}^t + F(x_{r2}^t - x_{r3}^t) \tag{2.25}$$

where v_i^t is the mutant, x_{r1}^t, x_{r1}^t and x_{r1}^t are three randomly selected designs, *t* is the iteration number and *F* is the scaling factor. After the generation of N_P mutants, the crossover of the mutants takes place between the mutants v_i^t and x_{r1}^t, and the trial solution, T_i^t, generated by crossover is:

$$T_{i,j}^t = \begin{cases} V_{i,j}^t & \text{if } j \in I_i \text{ or } rand(0,1) < CR \\ x_{r1,j}^t & \text{if } j \notin I_i \text{ or } rand(0,1) \geq CR \end{cases} \tag{2.26}$$

where, *j* represents the jth element in the design, *CR* is the predefined critical ratio, and I_i is an array of non-repeating numbers from 1 to *m*. The objective values of the trial

solutions are evaluated and compared with the original objective function values to decide which solution is added to the population in the next iteration:

$$x_i^{t+1} = \begin{cases} x_i^t & \text{if } F(x_i^t) > F(T_i^t) \\ T_i^t & \text{if } F(x_i^t) \le F(T_i^t) \end{cases} \tag{2.27}$$

The selection is then repeated for N_P times until a new population is generated. The development of DEA mainly focuses on developing appropriate mutation, crossover, and selection mechanisms. Beside the linear addition mutation method, other methods, such as the current-to-best method, have been proposed [B141]:

$$\begin{aligned} v_i^t &= x_{best}^t + F(x_{r1}^t - x_{r2}^t) \\ v_i^t &= x_{r1}^t + F(x_{best}^t - x_{r2}^t) \\ v_i^t &= x_{r1}^t + F(x_{r2}^t - x_{r3}^t) + F(x_{r4}^t - x_{r5}^t) \end{aligned} \tag{2.28}$$

The usage of the best candidate in each iteration is similar to PSOs and significantly increases the exploration ability of the algorithm. For the crossover schemes, the exponential crossover, where the mutant/donor contributes less to the trial solution, has been proposed and proved to be effective when neighbor decision parameters are linked together for large-scale problems [B141]. The DEA and its variants have been widely applied in electrical engineering. In motor modelling and optimization problems, DEA has been successfully applied in the design of brushless permanent motor [B141], interior permanent magnet (IPM) motor [B142], induction machine [B143] and AC servo motor design [B144]. In antenna array synthesis problems, DEA has been applied to aid to compensate the mutual coupling of linear arrays [B145-B146], planar array [B147], and microstrip antenna [B148-B149]. Comparative studies have been conducted to examine the performance of DEA, GA, PSO and other popular studied algorithms, and the results show that DEA required a large population to avoid premature problem of a medium size problem [B91].

(2) Simulated Annealing Algorithm and Tabu Search Method

Simulated annealing algorithm and tabu search method are two optimization methods with a relatively long history, and do not rely on the evolvement of population. Instead, both algorithms start with only one random point in the design space and search according to certain mechanisms [B91]. The simulated annealing (SA)

algorithm was inspired by the metal annealing procedures and was proposed in 1983 [B150]. The workflow of SA is given in Figure 2.11.

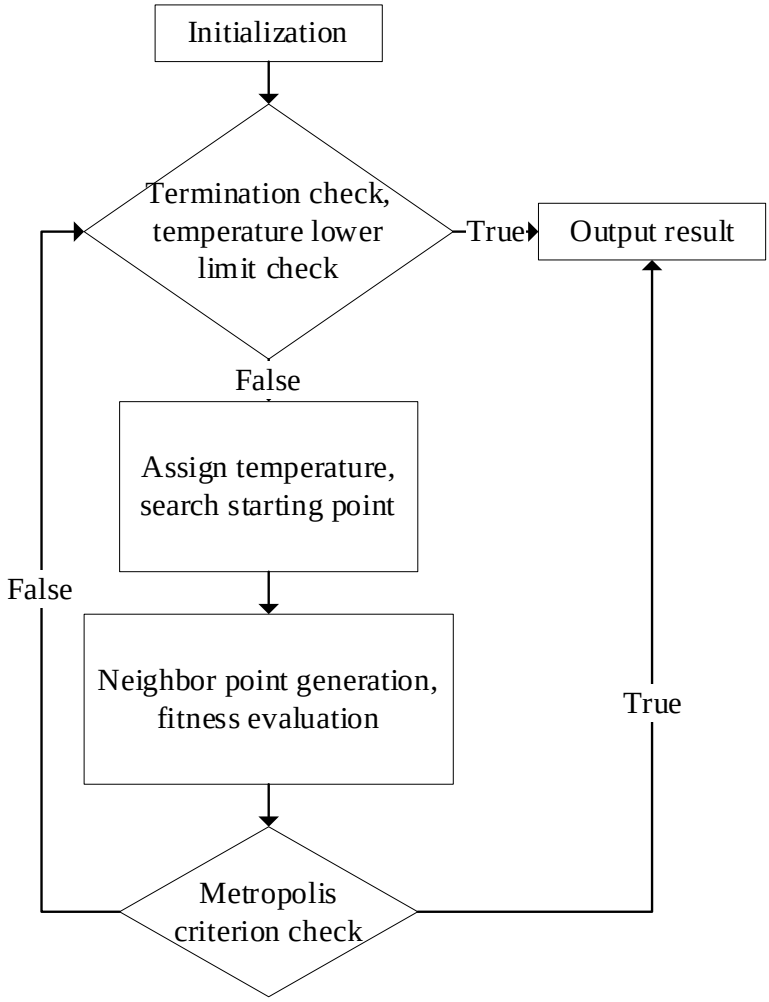

Fig. 2.11. Workflow of SA

In the initialization step, the initial point and temperature, constraints, design domain and objective functions are defined. One initial point in the design space is then generated from the neighbor of the selected point and its objective function value is evaluated. If the neighbor point has a better objective value, it is used as the starting point for the next iteration. Else, the metropolis criterion is executed. Assume the current temperature is T_c, the initial point is x_i and the generated neighbor point is x_{i+1}, define a virtual coefficient, w, and a random number, s to judge if the neighbor point should be accepted as new point [B151]:

$$w = e^{-(f(x_{i+1}) - f(x_i)/T_c)}$$
$$s = \text{rand}(0,1) \tag{2.29}$$
$$\text{if } w > s, \text{ accept } x_{i+1}, \text{ else reject.}$$

The usage of the metropolis criterion allows motions from the current best position to a worse one in its neighbor and hence gives the algorithm the ability to escape from the local optima. The applications of SA in electrical engineering have mainly been focused on electromagnetic devices design and optimization, for both single and multi-objective problems [B152-B154], outer rotor PM machine optimization [B155], electrical motor design [B156], and smart grid optimization [B157-B158]. Moreover, the method has been hybridized with the modern evolutionary algorithms such as GA and PSO [B159-B160] for performance enhancement. The addition of population to the algorithm also allowed a parallel computing and hence a faster optimization speed [B151].

Another well-explored neighbor searching optimization methodology is the tabu search (TS) method. TS method employs a tabu list to store the visited places and hence avoid repetitive searching. The workflow of an advanced TS is depicted in Figure 2.12. In the advanced version of TS, the intensification and diversification processes during the neighbor search are added to the algorithm to enable the algorithm to escape from local optima [B161].

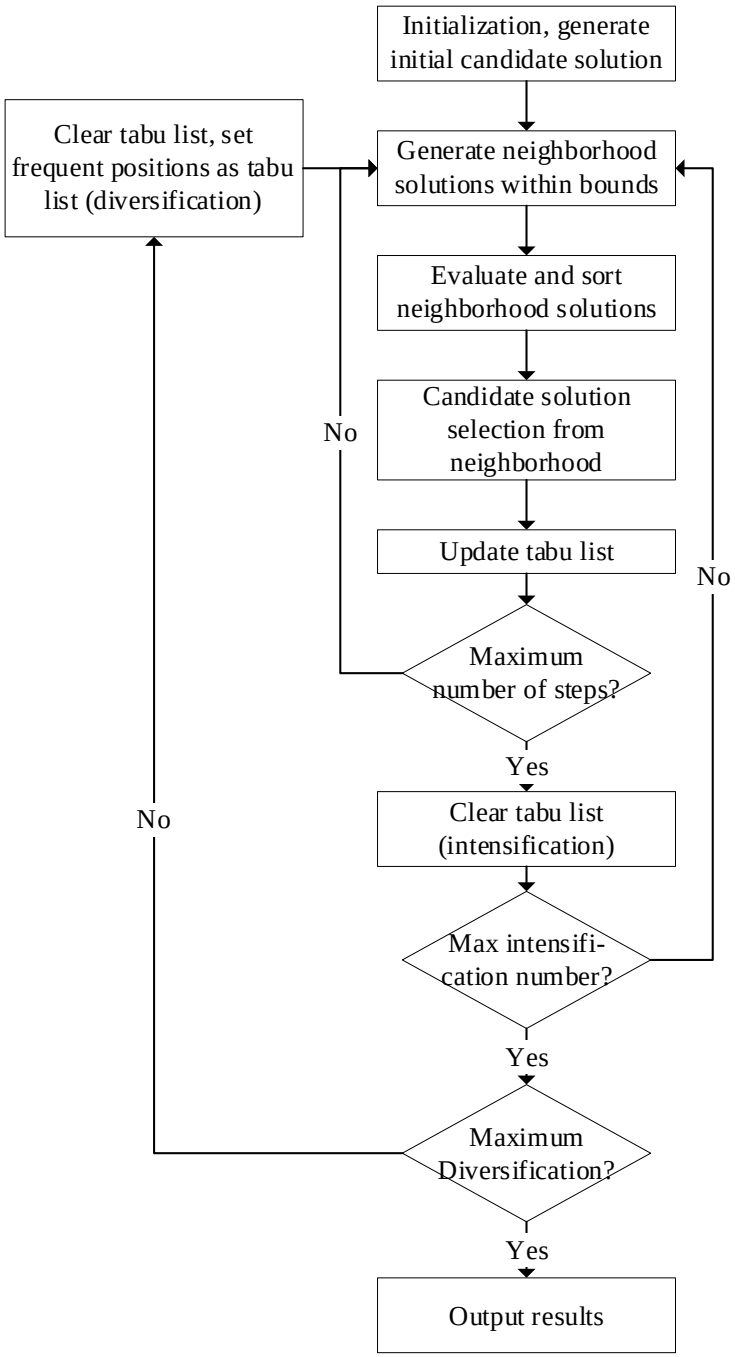

Fig. 2.12. Workflow of advanced TS

Considering a minimization problem, the initial solution, initial neighborhood radius, number of neighborhood solutions are defined in the initialization process. Followed by that, the neighborhood solutions are generated and sorted based on their objective values, and the solution with the lowest objective value is identified as the candidate solution. If the objective value of the candidate solution is lower than that of the initial solution and not in the tabu list, choose the candidate solution as the starting

solution for the next iteration and add it to the tabu list, then if the maximum number of initial searching steps is not reached, return to neighbor generation step, and repeat the initial searching process. If the maximum number of initial searching steps is reached, then clear the tabu list, return to the initial searching step, and search again the neighborhood of current best solution. This intensification step ensures the neighborhood can be extensively explored. If the maximum intensification is reached as well, then clear the tabu list and randomly select a new initial position and repeat the initial searching again. This diversification process ensures the algorithm is able to escape from local optima and serves similar purpose as in a mutation process. The TS method enjoys the merit of simple structure and convenience in terms of coding and applications [B161], and hence has been extensively applied in electrical engineering. In [B162-B165], TS methods have been employed in the optimization of placements of devices in electric distribution system, electrical motor, and electrical network. However, when facing problems with excessively large dimensions and complex structures, to ensure the neighborhood of the selected solution can be extensively explored, often a relatively large number of sampling points is necessary, which significantly increase the optimization time. To solve this issue, TS has been hybridized with PSO and ant colony optimization algorithms [B163, B166], and by adding population to TS method, the optimization speed increase significantly, and moreover parallel computing [B167-B168] can be done with multiple starting points in TS method.

(3) Artificial Bee Colony, Ant Colony Optimization and Firefly Algorithms

The artificial bee colony (ABC) algorithm, ant colony optimization (ACO) and firefly algorithm are all swarm-based algorithms which are proposed in the past 20 years and have also a shorter history. Similar to PSO algorithm, each of the aforementioned three algorithms imitates certain natural behavior of a swarm for searching purposes and are proved to be able to converge to optimum [B91].

The ABC algorithm is proposed in 2009 [B169]. The swarm is divided into three groups of bees: employ bees, onlookers, and scout bees. The flowchart of ABC is depicted in Figure. 2.13 [B91].

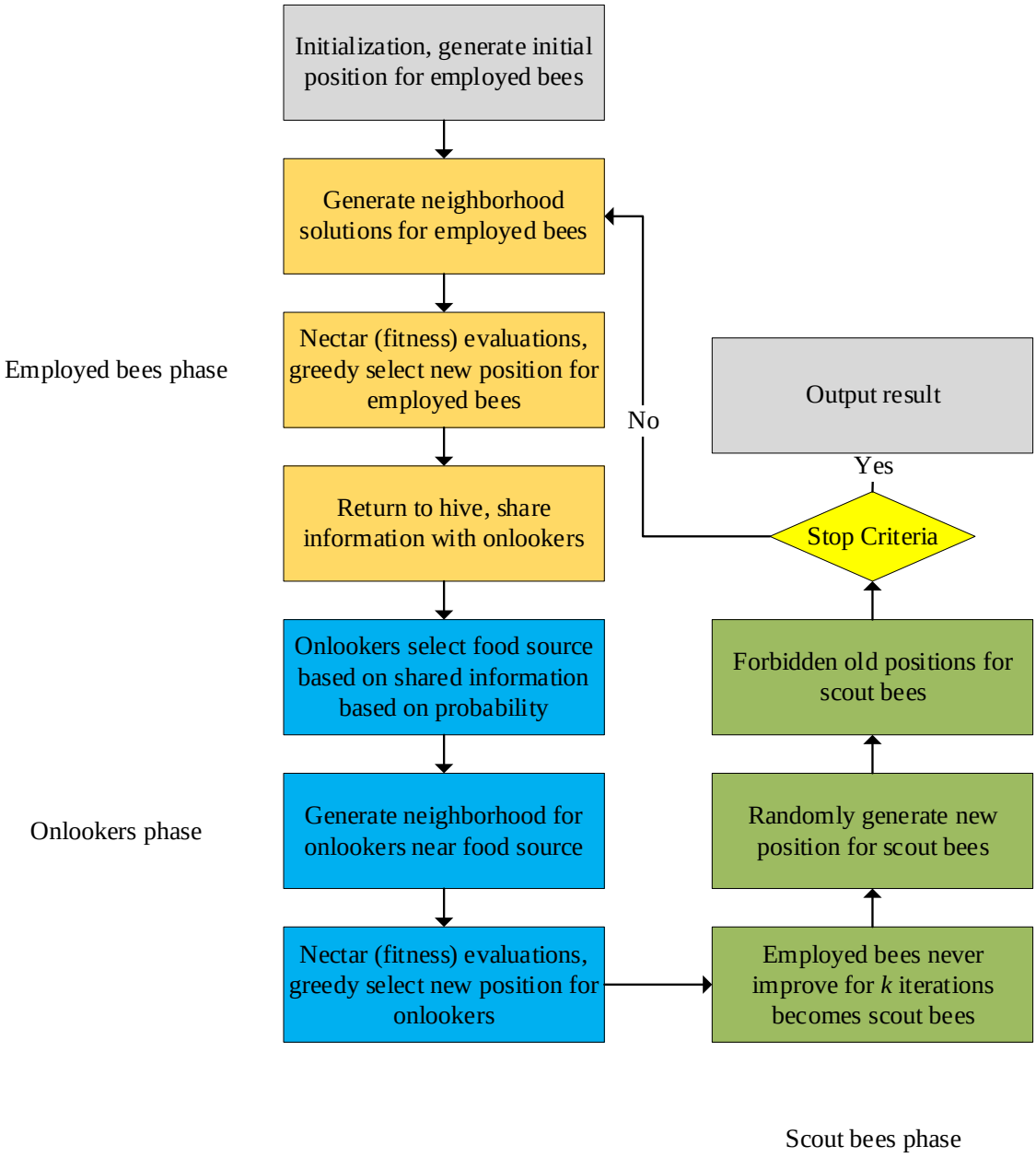

Fig. 2.13. Workflow of three-phase ABC [B91]

The improved ABC algorithms utilize the dancing behavior of the employ bees to share information within the swarm. In the initialization phase, for an n-dimensional problem, the initial positions of the m employ bees are generated via [B170]:

$$x_{m,i} = l_i + \text{rand}(0,1)(u_i - l_i),\ i = 1,2,3,...,n,\ m = 1,2,3,...,N_e \tag{2.30}$$

Here i denotes the ith element in the input vector, u_i and l_i are the upper and lower bounds in the ith element. In the employed bees phase, the neighborhood of the

employed bee x^m is generated as:

$$v_{m,i} = x_{m,i} + \phi_{m,i}(x_{m,i} - x_{k,i}) \tag{2.31}$$

where k is a randomly generated index and $\phi_{m,i}$ is a random number between $[-stepsize, stepsize]$. Followed by that the greedy selection is conducted between the original food source and the generated neighborhood food source, i.e., the solution with the best fitness value is chosen as the position for the employed bees. Then the algorithm enters the onlookers phase. Given the fitness value of each employed bee, the probability for an onlooker to select this specific employed bee is [B170]:

$$\begin{aligned} fit_m(x_m) &= \begin{pmatrix} \dfrac{1}{1+f_m(x_m)}, & f_m(x_m) > 0 \\ 1+|f_m(x_m)|, & f_m(x_m) \le 0 \end{pmatrix} \\ P_m &= \frac{fit_m(x_m)}{\sum_{m=1}^{N_e} fit_m(x_m)} \end{aligned} \tag{2.32}$$

where $f_m(x_m)$ is the objective value of the employed bee x_m, and $fit_m(x_m)$ is its fitness value. Employed bees with higher fitness values have a higher chance to be selected by the onlookers, and *vice versa*. Neighborhood search is then conducted for the onlookers as well using equation (2.31), and the greedy selection determines the position of each onlooker after the neighborhood search, and then the best solution found is stored in the memory. The last step in one iteration is the scout bees phase. In this phase, employed bees that have not updated their position for consecutive numbers of iteration is abandoned, their position is re-initialized using equation 2.30 and then is added back to the employed bees group. These three phases repeat until the stop criteria are met. Despite its short history, ABC algorithm has undergone extensive studies and has been successfully applied to electrical problems on many occasions. In [B171-B173] a chaotic ABC has been applied to the optimization of SVR modelling electrical load forecasting, AC-DC power flow model and parameter simulation of wireless power transmission systems. Moreover, ABC hybridized with GA has been used to tune the speed controller of PMSM drive [B174] and has been applied to train the artificial neural network and machine learning [B175-B178] for various

applications, such as signal processing and data set classifications.

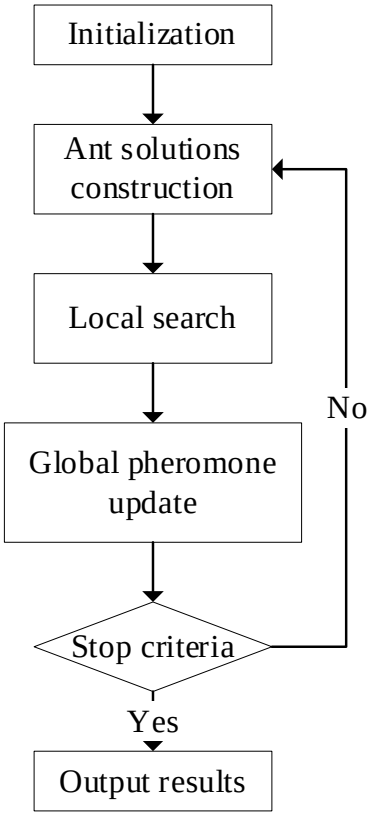

Fig. 2.14. Workflow of three-phase ACO

Ant colony optimization (ACO) algorithm is another population-based heuristic algorithm that imitate the food finding process of ant swarms, as there is a claim that a colony of ant is able to find the shortest path to a food source [B179]. The workflow of ACO is depicted in Figure 2.14.

In the initialization stage all the pheromone values are determined. Followed by that, the construction of each ant solution is based on random information and probability function. Assuming N_p ants are used, with each ant containing N design parameters, at iteration k, the possibility of the ant i selecting a partial solution X can be represented as [B179]:

$$P_X^i = \begin{cases} 0 & X \in Tabu_i(\mathrm{t}) \\ \dfrac{(\tau_X(t))^\alpha \cdot (\eta_X)^\beta}{\sum\limits_{j \notin Tabu_i(t);\, j \in N} (\tau_j(t))^\alpha \cdot (\eta_j)^\beta} & X \notin Tabu_i(\mathrm{t}) \end{cases} \tag{2.33}$$

Here, i is the index of the ant, X is the index for the possible partial solution that belongs to the entire design domain N. $\tau_X(t)$ represents the pheromone value of ant X, η_X is a heuristic pre-defined value, and the tabu list $Tabu_i$(t) represents the already selected partial solution by the ant i. When all ants select their partial solutions, their objective function values are evaluated to obtain their corresponding pheromone information. An optional local search is conducted to exploit the design domain when needed. At the end of each iteration the pheromone information of the partial solution X is updated via [B179]:

$$\begin{aligned} \tau_X(t+1) &= (1-\rho)\cdot\tau_X(t) + \Delta\tau_X(t) \\ \Delta\tau_X(t) &= \sum_{X\in S^j(t);\, j\in[1,N]} f(S^j(t)) \end{aligned} \tag{2.34}$$

Here ρ is the evaporation coefficient between [0,1], $\Delta\tau_X(t)$ represents the additional pheromone of the partial solution, j is the index of ants containing partial solution X, $S^j(t)$ is the full solution set of ant j, and $f(S^j(t))$ is the fitness value of the ant. After the updating of the pheromone information, the ant with the best fitness value is identified as the optimum of the iteration, and these processes repeat until the pre-defined stop criteria are met.

The nature of ACO is very similar to that of PSO, and hence their pros and cons are relatively similar. ACO can be easily implemented in a parallel computing manner, thereby significantly increase the optimization speed. However, because the positions of all ants are arbitrary, ACO is more appropriate in continuous problems with low number of design parameters. When the dimension of the problem is high, ACO algorithm often requires a large swarm size for a fast convergence and hence a huge amount of computational resources. Nevertheless, similar to PSO, ACO shows great potential in electrical engineering. In [B180], ACO has been applied to optimize the dispatch model in the microgrid systems and reported to outperform other similar group search methods. In [B181-B183], ACO has been used to optimize the power electronics design, wind energy optimization and electrical network reconfiguration. The results reveal ACO is more competitive to conventional population-based methods.

The firefly algorithm is one of the newest heuristic-search, swarm-based algorithms developed in the recent two decades [B184]. The algorithm was developed to solve multi-nodal problems with higher order of dimensions that are not easily solved by conventional algorithms like PSO and GA. In the firefly algorithm, each fly has its own light intensity, and the flies with a smaller intensity tend to move towards flies with a larger intensity. The attractiveness of the two flies determines the interaction of them. If the attractiveness is set to zero, a random walk governing by the pre-defined randomization parameters is conducted. On the other hand, when the attractiveness is high, the fly with a low intensity moves towards the fly with a high intensity [B91]. The workflow of a firefly algorithm is given in Figure 2.15.

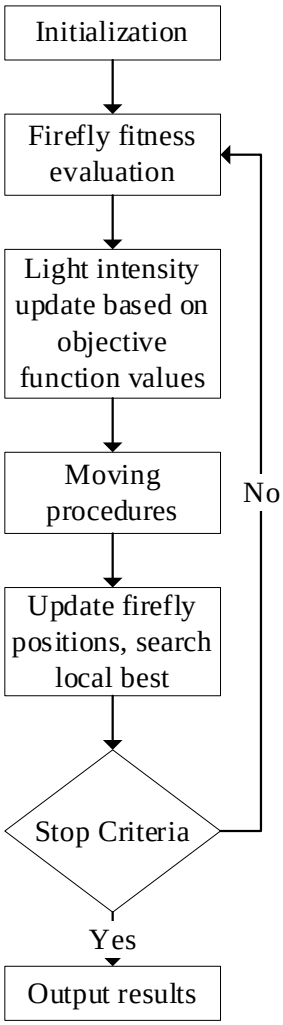

Fig. 2.15. Workflow of firefly algorithm [B184]

The light intensity of a firefly s can be formulated as:

$$I(r) = I_0 e^{-\gamma r^2}, I_0(s) \propto f(s) \tag{2.35}$$

Similarly, the attractiveness of the firefly s also reduces exponentially as the distance to the firefly increases, and hence can be formulated as:

$$\beta(r) = \beta_0 e^{-\gamma r^2}, r_{ij} = \left\| s_i - s_j \right\| \tag{2.36}$$

Here, r_{ij} denotes the Euclidean distance between the two fireflies. If the firefly s_i has a smaller intensity when compared with firefly s_j, it is attracted via [B184]:

$$s_i = s_i + \beta_0 e^{-\gamma r_{ij}^2}(s_j - s_i) + \varepsilon\alpha \tag{2.37}$$

where ε and α are two random numbers following a Gaussian distribution and the pre-defined randomization parameters. The movement of a firefly contains three portions, its inertia, the movement towards the better firefly and lastly a random factor. By adding the random factor, the algorithm is able to escape from local optima like other EAs. Firefly algorithm has received many attentions due to its prominent performance in complex engineering problems with high dimensions. In [B185], the firefly algorithm is used to optimize photovoltaic systems with a large number of maxima. It is claimed that the firefly algorithm was able to converge to the global optimum of the problem more effectively, when compared with that of the genetic programming. Moreover, similar to PSOs, a firefly algorithm is also used to train the artificial neural network in a photovoltaic system to determine the weight of each neuron [B186]. Firefly algorithm also finds its applications in wind-turbine optimizations [B187-B188], grid-optimizations [B189] and other hybridization applications [B190].

2.3 Metamaterial and Its Applications in Wireless Power Transmission

Metamaterials (MM) are artificial engineered materials exhibiting uncommon properties that cannot be found in naturally occurred materials, especially in terms of electromagnetic properties [B191]. The main electromagnetic properties of materials

are their magnetic permeability μ and electric permittivity ε, and hence the aim of the development of MMs is to develop artificial materials that can exhibit negative permittivity/permeability, or both at the selected frequencies. In conventional materials, both the permeability and permittivity are positive, the electromagnetic wave can therefore travel within the material with different speeds. Moreover, the directions of the electric vector, the magnetic vector and the wave vector of the incident EM wave follow the right-hand rule, and hence the conventional materials are named as right-handed material. The Poynting vector of the travelling wave inside materials indicates the flow of energy and is always parallel to and in the same direction of the wave vector in conventional material, and hence energy decays as the EM wave travels inside conventional materials. In contrast, when EM wave travels in the MM with negative permeability and permittivity, the electric vector, magnetic vector, and the wave vector follow the left-handed rule, and the Poynting vector is oppose to the wave vector inside the material [B191], and hence the MM is also regarded as backward-wave media.

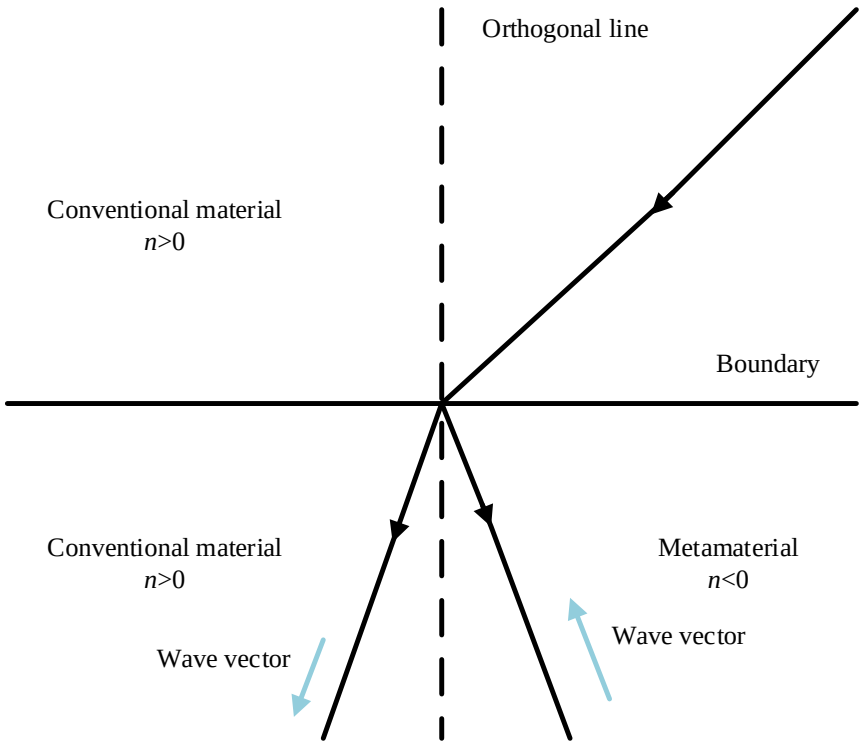

Fig. 2.16. Refraction of conventional material and MM [B192]

Furthermore, the optical property of the MM structure, which is described by the refractive index of the material, can be characterized as:

$$\begin{aligned} n &= \pm\sqrt{\mu\varepsilon} \\ n_1 \sin\theta_1 &= n_2 \sin\theta_2 \end{aligned} \tag{2.38}$$

where θ_1 and θ_1 are the incident and refractive angle when EM wave travels through the boundary between MM and conventional material, and n_1 , n_2 are the refractive indices of the MM and the conventional material. For the MM, due to the double negative property the refractive is negative as well, $n = -\sqrt{\mu\varepsilon}$ and hence the incident EM wave and the refractive wave are at the same side of the orthogonal line of the interface [B192]. This phenomenon is depicted in Figure 2.16. The MM has been actively studied in areas of super-lens, invisible cloak, and all other applications [B193] due to its ability to amplify the evanescent wave. In recent researches, it is found that when the MM is added to the near-field and mid-field wireless power transmission (WPT) system, the transfer efficiency can be improved [B193]. When the MM is placed between the transmission and receiving coils (Tx and Rx coils), the magnetic field is focused due to the negative refraction explained in the afore-part, and the coupling of the evanescent waves of the Tx and Rx coils is also enhanced due to the amplification property of the MM structure, thereby increasing the transmission efficiency of the WPT systems [B194]. If the size of the device is much smaller than the wavelength it works in, the device works in the deep sub-wavelength regime and the electrical and magnetic field are decoupled. In near-field WPT applications, the size of the device is always in centimeter level, which is significantly smaller than the working wavelength, so only negative magnetic permeability is required. The negative permeability structure can be constructed by periodic arrays of small *LC* resonators of the selected frequency [B193]. The repetition of resonators in the direction of the wave propagation led to the pass on of the magneto-induced wave and evanescent wave via the induction of current inside the resonators. The dispersion equation of 2-D array of MM resonator can be formulated as [B194]:

$$\frac{\omega_0}{\omega} = (1 + k_x \cos(\gamma_x a) + k_y \cos(\gamma_y a))^{\frac{1}{2}} \tag{2.39}$$

where a represents the periodicity of the MM 2-D array, k_x and k_y represent the coupling coefficients in the planar directions, γ_x and γ_y are the complex propagation coefficients, and often $|\gamma_x a|, |\gamma_y a| < 1$ in near-field WPT applications. The evanescent wave from the Tx coil coupled with the resonator in MM structure and passes energy to the resonator, and then the resonator amplifies the resultant magneto-induced wave, and hence the power-transmission efficiency can be significantly enhanced [B193]. By calibrating the structure of the unit cell, the addition values of the circuit component in the resonator, the placement of the MM structure and all other parameters, various studies have been conducted to investigate the effects of additions of MM structures in the WPT system in near-field applications.

Based on the coupling methods, the near-field WPT system can be constructed based on either the inductive coupling or the magnetic resonance coupling methodologies. The inductive coupling WPT requires the Tx and Rx coils to be in close proximity to each other and hence insertion of MM structure may be difficult in the inductive coupling WPT, also the increment in the traveling distance significantly reduce the transmission efficiency, which further reduce the scope of applications of inductive coupling based WPT. On the other hand, the magnetic resonance coupling WPT systems work based on the resonance of the Tx and Rx coils, and hence is suitable for mid-range applications. Various efforts to increase the power transfer efficiency (PTE) of the mid-range WPT systems, including coupling optimization [B195], multiple coils systems [B196-B197] and all other methods have been proposed in the past researches. One of the most effective methods to enhance the PTE in mid-range WPT is the insertion of MM structure in the WPT systems. The first application of MM structures in WPT system was proposed by Wang *et. al*. in 2010 [B198] and is still a relevant new topic attracting many attentions. The most common method to apply the MM structure is to design the MM structure as a slab and to insert it in between the Tx and Rx coils. The function of MM slab is similar to a zooming lens in

optical applications, the magnetic field from the Tx coil is focused to the receiver coil Rx and hence the PTE is enhanced. Figure 2.17 summarizes the existing structures and methodologies of MM applications in the WPT system in the past researches after the advance of MM-assisted WPT systems.

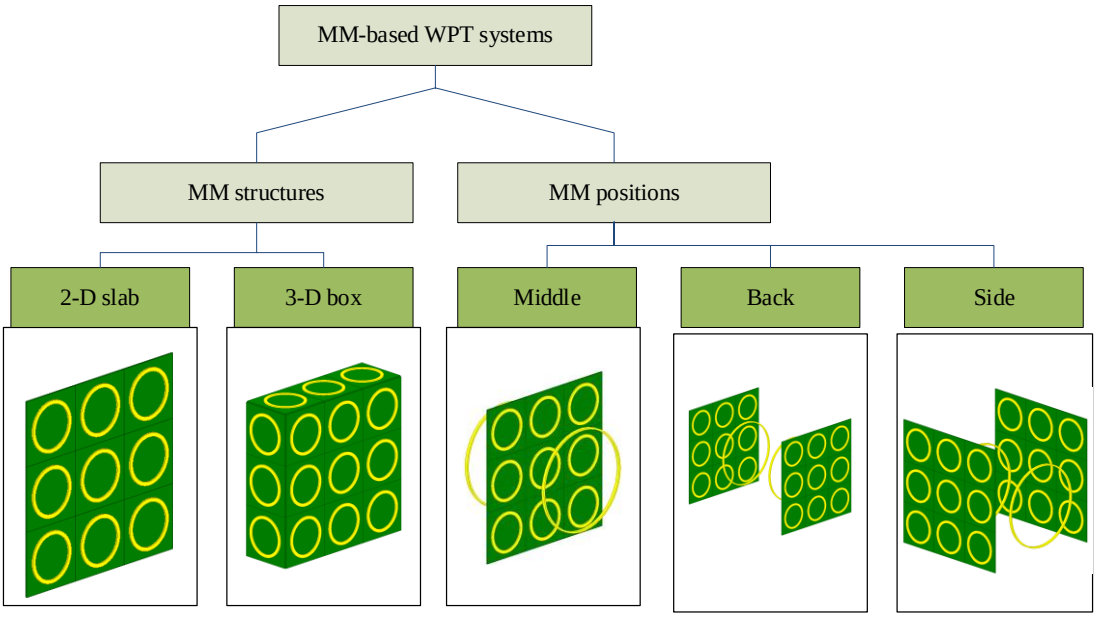

Fig. 2.17. Existing MM structures and relative positions in WPT system [B193].

The MM slab can be either in 2-D [B199-B214], where MM unit cells are arranged into a planar board, or in 3-D, forming square boxes [B215-B217]. The major difference between the two methods is that in 2-D applications there is no repetition of MM structures in the direction magnetic field travels, and hence no periodicity needs to be considered, while for the 3-D applications, the mutual inductance between the adjacent MM structure in the magnetic field travel direction significantly affects the resonance performance of the structure [B193]. Furthermore, the relative position of the MM can be quite different in various applications, and hence the MM slab can play different roles in the WPT system. The majority of the past researches [B200-B209] have placed the MM slab in between the Tx and Rx coils and used it as the intermediate station for the field propagation, either in single-layer pattern or double-layer pattern. Other than that, the MM slab has also been place at the back of the Tx and Rx coil [B213], or around the traveling path of the magnetic field [B214]. The

main purpose of these application is to use the MM slabs to guide the magnetic field that deviate from the main path field propagation and confine the magnetic field within the WPT systems. Other than that, the combination of different MM slabs with different purposes has been proposed [B199]. In this system, the MM slabs are designed to have different resonance frequencies and hence different equivalent magnetic permeabilities at the selected working frequency, and hence their roles in the WPT systems are completely different, with the middle MM slab with negative permeability serves as amplifier, and the side ones with zero permeability are used for total reflections.

For a typical mid-range magnetic-coupling-based WPT system, its circuit diagram can be described as Figure 2.18. The PTE of the system is [B193]:

$$\eta = \frac{P_S}{P_L} = \frac{4 \cdot \dfrac{\omega^2 M^2 R_S R_L}{R_S^2 R_2^2}}{\left((1+\dfrac{R_S}{R_1})(1+\dfrac{R_L}{R_2}) + \dfrac{\omega^2 M^2}{R_1 R_2} \right)^2} \tag{2.40}$$

Here, η represents the PTE of the WPT system, P_S and P_L are the source and load power, ω is the working frequency, M, R_S, R_L, R_1, R_2 are the mutual inductance between two resonators, resistance of source, load, resonator 1 and 2 (Tx and Rx coils) in Figure 2.18 respectively [B193].

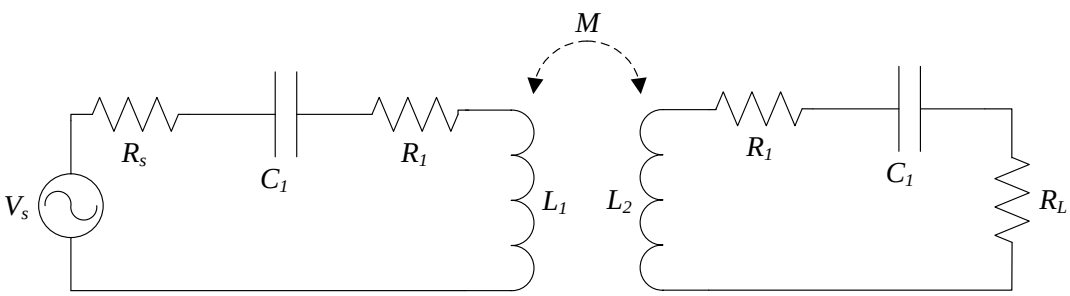

Fig. 2.18. Equivalent circuit of a magnetic resonance based WPT system

The maximum PTE is reached when [B193]:

$$\frac{R_S}{R_1} = \frac{R_L}{R_2} = \sqrt{1+\frac{\omega^2 M^2}{R_1 R_2}} \tag{2.41}$$

And the optimum PTE value is [B193]:

$$\eta_{opt} = \frac{k^2 Q_1 Q_2}{(1+\sqrt{1+k^2 Q_1 Q_2})} = \frac{U^2}{(1+\sqrt{1+U^2})^2} \tag{2.42}$$

where k represents the coupling coefficient between two resonator coils, Q_1, Q_2 are the quality factors of the two resonator coils, and $U = k\sqrt{Q_1 Q_2}$ is the figure-of -merit of the WPT system. With U larger than one the system is strongly coupled and *vice versa*. The plot of η_{opt} versus U is depicted in Figure 2.19. The higher the figure-of-merit of the two resonators, the higher the PTE for the WPT system. Hence, either the coupling of the two resonators, or the quality factors of the two resonator coils need to be high to obtain a high figure-of-merit and hence a high optimal PTE. The negative permeability MM structure can help to significantly enhance the coupling between the two resonator coils by collecting magnetic field that direct away from the two resonators and also enhance the evanescent waves travelling between the two resonator coils, thereby increasing the PTE of the WPT system [B193].

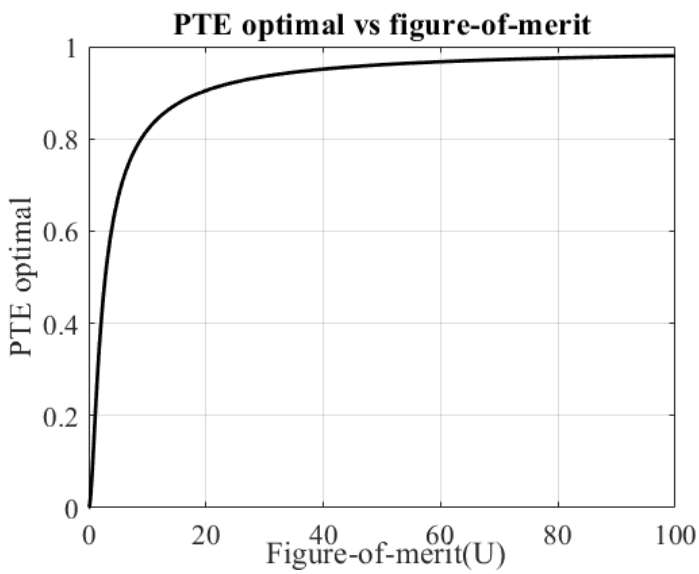

Fig. 2.19. Plot of η_{opt} against U of resonance based WPT system

In the high working frequency condition (GHz range), the equivalent permeability of a homogeneous MM unit cell can be calculated as [B218]:

$$
\begin{aligned}
z &= \pm\sqrt{\frac{(1+S_{11})^2 - S_{21}^2}{(1-S_{11})^2 - S_{21}^2}}; \\
n &= \frac{1}{k_0 d}\left[\left\{\left[\ln(e^{ink_0 d})\right]'' + 2m\pi\right\} - i\left[\ln(e^{ink_0 d})\right]'\right]; \\
\varepsilon &= \frac{n}{z}; \\
\mu &= nz.
\end{aligned}
\tag{2.43}
$$

where z is the equivalent impedance, n is the refractive index of the material, k_0 is the wavenumber, d is the maximum length of the unit cell, m is the branch due to the periodicity of the MM structure, and S_{11}, S_{21} are the scattering parameters for reflection and transmission [B218], and can be measured or simulated via comparing the power at the source and the receiver sides. This parameter extraction method is proved to be efficient for both homogeneous and inhomogeneous MMs working in GHz frequency range or above. When the working frequency drops to relative low values, such as in MHz range, this method is no longer valid, as the MM structure is no longer uniformly distributed. Hence, it can only be used as a qualitative analysis to determine zero point of the permeability of the MM structure [B193].

Table 2.1. Summary of the current study in MM based WPT [B193]

Ref.	Dim	Position	Working frequency (MHz)	Tx/Rx diameter (mm)	Transfer distance (mm)	PTE/ Increment (%)
[B199]	2-D	Middle and back	2600	66.5	25	70.64/10.49
[B200]	2-D	Middle	27.4	400	200	41.2/10.7
[B201]	2-D	Middle	58.8	60	200	13.6/10.2
[B194]	2-D	Middle	27	400	500	47/30
[B202]	2-D	Middle	13.56	100	300	52.3/41.7
[B203]	2-D	Middle	13.56	130	300	45.8/36.4
[B199]	2-D	Middle	13.56	200	400	48.3/12.1

[B204]	2-D	Middle	6.78	150	200	38/17
[B205]	2-D	Middle	6.78	500	600	36.7/20.7
[B206]	2-D	Middle	6.5	600	1000	57.9/32.6
[B207]	2-D	Middle	2.8	500	1600	50.9/18.6
[B208]	2-D	Double layer	472.6	18	30	60.8/8.6
[B209]	2-D	Double layer	6.78	300	350	50/27
[B210]	2-D	Double layer	7.43	150	200	18.6/7.9
[B211]	2-D	Front and back	24.1	170	400	72/24
[B212]	2-D	Side	7	140	225	16.2/15.7
[B213]	3-D	Middle	8.64	400	1000	53.3/24.5
[B214]	3-D	Middle	5.57	40	40	35/15
[B215]	3-D	Middle	6.5	600	1000	54/33
[B216]	3-D	Middle	13-16	20	80	1/0.9999
[B205]	3-D	Middle	6.78	500	600	40/24
[B217]	3-D	Double layer	1700	30	36	52/Nil

I

n table 2.1, the latest researches related to MM-based WPT systems in MHz range are summarized [B191]. It can be seen that in current MM-based WPT applications: 1. The PTE can be greatly enhanced by the MM slabs/structures; 2. The majority of the applications inserts the MM slab in between the transmission and receiver coils; 3. There is no analytical model that can connect the PTE value with other parameters such as the size of MM structure and WPT coils; 4. The minimum working frequency is still in MHz range; and 5. The transfer distance varies significantly.

2.4 Summary

In this chapter, the state-of-art of the modeling methodologies that are employed in topology optimization are reviewed. The available methods include the discretized methods, continuous boundary variation methods, and the surrogate methods. Among all three methods, the discretized method is the simplest and most convenient one to use, and also associates with problems such as checkerboard pattern, zigzag boundaries. The boundary variation methods could construct smooth boundary topology, with slightly higher programming complexities. The last method, the surrogate methods has the most efficient modeling speed with smallest number of parameters, and however the possible topology might also be limited as well. All three methods have their own *pros* and *cons*, as well as area of specialties.

Table 2.2. Summary of the modelling method in topology optimization

Method	Pros	Cons
Homogenization	Easy Implementation	Checkerboard pattern, large number of design parameters
SIMP	Easy Implementation, a smaller number of control parameters	Checkerboard pattern, uneven boundary, intermediate density
RAMP	Simpler density function	Checkerboard pattern, uneven boundary, intermediate density
ON/OFF	Straightforward implementation, binary representation	Checkerboard pattern, uneven boundary, oscillation
Level-set method	Less number of control parameters, smooth boundary	Relatively hard implementation, not able to create holes in solid
Phase-field	Similar to Level-set method	Large transition region
Surrogate Model	Less number of control parameters, faster simulations	Limited number of possible designs, accuracy highly related to designers

The optimization algorithms that are commonly employed in the engineering optimization problems including topology optimizations are introduced in detail as well. The evolutionary algorithms that imitate the behavior of naturally occurring phenomena have been widely applied in the past two decades and proved to be efficient and more flexible than the conventional optimization algorithms that based on the gradient information. More specially, the memetic algorithms that based on the spread of the optimum information within the entire population are the most recent algorithms with a high efficiency.

Table 2.3. Summary of the optimization algorithms in topology optimization

Method	Pros	Cons
Gradient-based	Fast searching speed	Tedious calculation and hard for complex problems
Direct search	Easy Implementation	Global optimum not guaranteed
GA	Easy Implementation，convergence guaranteed, widely adopted, great flexibility	No local search step, optimization speed could be further enhanced
PSO	Easy implementation, faster convergence speed	Global optimum not guaranteed
ABC	Similar to PSO	Less developed
SFLA	Similar to PSO	NO local search process
ESO/BESO/SERA	Naturally developed for topology optimization, works well with discretized method	Uneven boundary, checkerboard pattern, large number of control parameters

Lastly the metamaterial (MM) and its applications in the wireless-power-transmission (WPT) systems have been reviewed. The construction of MM structures mainly based on the principle of the magnetic resonance of the *RLC* circuit of the microscale resonators. Their applications in the WPT system significantly enhance the performance of the system, and however there is a lack in depth mathematical model

that can describe the effects of MM in the WPT system in current academia.

2.5 Reference-Part B

[B1] Sigmund, and K. Maute, K, "Topology optimization approaches," *Structural and Multidisciplinary Optimization*, vol. 48, no. 6, pp.1031-1055, 2013.

[B2] G. Allaire, and F. Jouve, and H. Maillot, "Topology optimization for minimum stress design with the homogenization method," *Structural and Multidisciplinary Optimization*, vol. 28, pp.87-98, 2004.

[B3] O. Sigmund, "Morphology-based black and white filters for topology optimization," *Structural and Multidisciplinary Optimization*, vol. 33, no. 4-5, pp.401-424, 2007.

[B4] G. Paulino and C. Le, "A modified Q4/Q4 element for topology optimization," *Structural and Multidisciplinary Optimization*, vol. 37, no. 3, pp.255-264, 2009.

[B5] T. Belytschko, S. Xiao, and C. Parimi, "Topology optimization with implicit functions and regularization," *International Journal for Numerical Methods in Engineering*, vol. 57, no. 8, pp.1177-1196, 2003.

[B6] T. Poulsen, "Topology optimization in wavelet space," *International Journal for Numerical Methods in Engineering*, vol. 53, no. 3, pp.567-582, 2002.

[B7] M. Zhou, and G. Rozvany, "The COC algorithm, part II: topological, geometry and generalized shape optimization," *Comput Methods Appl Mech Eng*, vol. 89, pp.309-336, 1991.

[B8] M. Bendsøe, and O. Sigmund, "Material interpolation schemes in topology optimization," *Arch Appl Mech*, vol. 69, no. 9-10, pp.635–654, 1999.

[B9] W. Zuo, and K. Saitou, "Multi-material topology optimization using ordered SIMP interpolation," *Structural and Multidisciplinary Optimization*, vol. 55, no. 2, pp.477-491, 2017.

[B10] F. Guo and I. P. Brown, "Simultaneous magnetic and structural topology optimization of synchronous reluctance machine rotors," *IEEE Transactions on Magnetics*, vol. 56, no. 10, Article no. 8101612, 2020.

[B11] S. Zhu, X. Yang, J. Wang, and B. Wang, “Design of MIMO antenna isolation structure based on a hybrid topology optimization method,” *IEEE Transactions on Antennas and Propagation*, vol. 67, no. 10, pp.6298-6307, 2019.

[B12] J. Blasques, “Multi-material topology optimization of laminated composite beams with eigenfrequency constraints,” *Compos Struct*, vol. 111, pp.45-55. 2014.

[B13] A. Rietz, “Sufficiency of a finite exponent in SIMP (power law) methods,” *Struct Multidiscip Optim*, vol. 21, no. 2, pp.159-163, 2001.

[B14] W. Zhang, W. Zhong, and X. Guo, X. “An explicit length scale control approach in SIMP-based topology optimization,” *Computer Methods in Applied Mechanics and Engineering*, vol. 282, pp.71-86, 2014.

[B15] G. Marck, and et al., “Topology optimization using the SIMP method for multiobjective conductive problems,” *Numerical Heat Transfer, Part B: Fundamentals*, vol. 61, no. 6, pp.439-470, 2012.

[B16] C. Le, and et al., “Stress-based topology optimization for continua,” *Structural and Multidisciplinary Optimization*, vol. 41, no. 4, pp.605-620, 2010.

[B17] Z. Xu, Q. Huang, and Z. Zhao, “Topology optimization of composite material plate with respect to sound radiation,” *Engineering Analysis with Boundary Elements*, vol. 35, no. 1, pp.61-67, 2011.

[B18] J. Martinez, “A note on the theoretical convergence properties of the SIMP method,” *Struct Multidiscip Optim*, vol. 29, no. 4, pp.319-232, 2005.

[B19] A. Dadalau, A. Hafla, and A. Verl, “A new adaptive penalization scheme for topology optimization,” *Prod Eng*, vol. 3, no. 4-5, pp.427-434, 2009.

[B20] M. Stolpe, K. Svanberg, “On the trajectories of penalization methods for topology optimization,” *Struct Multidiscip Optim*, vol. 21, no. 2, pp.128-139, 2001.

[B21] M. Stolpe, K. Svanberg, “An alternative interpolation scheme for minimum compliance topology optimization,” *Struct Multidiscip Optim*, vol. 22, no. 2, pp.116-124, 2001.

[B22] J. Byun, I. Park, and S. Hahn, “Topology optimization of electrostatic actuator using design sensitivity,” *IEEE Transactions on Magnetics*, vol. 38, no. 2, pp.1053-1056, 2002.

[B23] Y. Okamoto, K. Akiyama, and N. Takahashi, N, “3-D topology optimization of single-pole-type head by using design sensitivity analysis,” *IEEE Transactions on Magnetics*, vol. 42, no. 4, pp.1087-1090, 2006.

[B24] N. Takahashi, S. Nakazaki, and D. Miyagi, “Examination of optimal design method of electromagnetic shield using ON/OFF method,” *IEEE Transactions on Magnetics*, vol. 45, no. 3, pp.1546-1549, 2009.

[B25] N. Takahashi, S. Nakazaki, and D. Miyagi, “Optimization of electromagnetic and magnetic shielding using ON/OFF method,” *IEEE Transactions on Magnetics*, vol. 46, no. 8, pp.3153-3156, 2010.

[B26] N. Takahashi, T. Yamada, S. Shimose, and D. Miyagi, “Optimization of rotor of actual IPM motor using ON/OFF method,” *IEEE transactions on magnetics*, vol. 47, no. 5, pp.1262-1265, 2011.

[B27] Y. Hidaka, T. Sato and H. Igarashi, “Topology optimization method based on On-Off method and level set approach,” *IEEE Transactions on Magnetics*, vol. 50, no. 2, pp.617-620, Art no. 7015204, 2014.

[B28] N. Dijk, K. Maute, M. Langelaar, and F. Keulen, “Level-set methods for structural topology optimization: a review,” *Structural and Multidisciplinary Optimization*, vol. 48, no. 3, pp.437-472, 2013.

[B29] J. Deaton, and R. Grandhi, “A survey of structural and multidisciplinary continuum topology optimization: post 2000,” *Struct Multidisc Optim*, vol. 49, pp.1-38, 2014.

[B30] M. Wang, X. Wang, and D. Guo, “A level set method for structural topology optimization,” *Comput Methods Appl Mech Eng*, vol. 192, no. 1-2, pp.227-246, 2003.

[B31] S. Wang, and M. Wang, “Radial basis functions and level set method for structural topology optimization,” *Int J Numer Methods Eng*, vol. 65, no. 12, pp.2060-2090, 2006.

[B32] S. Wang, K. Lim, B. Khoo, and M. Wang, “An extended level set method for shape and topology optimization,” *J Comput Phys*, vol. 221, no. 1, pp.395-421, 2007.

[B33] A, Gomes A, and A. Suleman, “Topology optimization of a reinforced wing box for enhanced roll maneuvers,” *AIAA J*, vol. 46, no. 3, pp.548-556, 2008.

[B34] Z. Luo, L. Tong, M. Wang, and S. Wang, “Shape and topology optimization of compliant mechanisms using a parameterization level set method,” *J Comput Phys*, vol. 227, no. 1, pp.680-705, 2007.

[B35] Z. Luo, M. Wang, S. Wang, P. Wei, “A level set-based parameterization method for structural shape and topology optimization,” *Int J Numer Methods Eng*, vol. 76, no. 1, pp.1-26, 2008.

[B36] Z. Luo, L. Tong, and Z. Kang, “A level set method for structural shape and topology optimization using radial basis functions,” *Comput Struct*, vol. 87, no. 7-8, pp.425-434, 2009.

[B37] G. Allaire, and F. Jouve, “Minimum stress optimal design with the level set method,” *Eng Anal Bound Elem*, vol. 32, no. 11, pp.909-918, 2008.

[B38] X. Xing, P. Wei P, and M. Wang, “A finite element-based level set method for structural optimization,” *Int J Numer Methods Eng*, vol. 82, no. 7, pp.805-842, 2010.

[B39] D. Makhija, and K. Maute, “Numerical instabilities in level set topology optimization with the extended finite element method,” *Structural and Multidisciplinary Optimization*, vol. 49, no. 2, pp.185-197, 2014.

[B40] T. Fries, and T. Belytschko, “The extended/generalized finite element method: an overview of the method and its applications,” *Int J Numer Methods Eng*, vol. 84, no. 3, pp.253-304, 2010.

[B41] S. Kreissl, and K. Maute, “Level set based fluid topology optimization using the extended finite element method,” *Multidisc Optim*, vol. 46, no. 3, pp.311-326, 2012.

[B42] L. Miegroet, and P. Duysinx, “Stress concentration minimization of 2-D filets using X-FEM and level set description,” *Struct Multidisc Optim*, vol. 33, no. 4, pp.425-438, 2007.

[B43] M. Ruiter, and F. Keulen, “Topology optimization using a topology description function,” *Struct Multidisc Optim*, vol. 26, no. 6, pp406-416, 2004.

[B44] Z. Liu, J. Korvink, and R. Huang, “Structure topology optimization: fully coupled level set method via FEMLAB,” *Struct Multidisc Optim*, vol. 29, no. 6, pp.407-417, 2005.

[B45] S. Liu, and J. Korvink, “Adaptive moving mesh level set method for structure topology optimization,” *Eng Optim*, vol. 40, no. 6, pp.529-558, 2008.

[B46] N. Dijk, G. Yoon, F. Keulen, and M. Langelaar M, “A level set- based topology optimization using the element connectivity parameterization method,” *Struct Multidisc Optim*, vol. 42, no. 2, pp.269-282, 2010.

[B47] G. Pingen, M. Waidmann, A. Evgrafov, K. Maute, “A parametric level-set approach for topology optimization of flow domains,” *Struct Multidisc Optim*, vol. 41, no. 1, pp.117-131, 2010.

[B48] N. Dijk, M. Langelaar, and F. Keulen, “Explicit level-set based topology optimization using an exact Heaviside function and consistent sensitivity analysis,” *Int J Numer Methods Eng*, vol. 91, no. 1, pp.67-97, 2012.

[B49] T. Belytschko T, S. Xiao, and C. Parimi, “Topology optimization with implicit functions and regularization,” *Int J Numer Methods Eng*, vol. 57, no. 8, pp.1177-1196, 2003.

[B50] E. Haber, “A multilevel, level-set method for optimizing eigenvalues in shape design problems,” *J Comput Phys*, vol. 198, no. 2, pp.518-534, 2004.

[B51] J. Guest, J. Pr´evost, and T. Belytschko, “Achieving minimum length scale in topology optimization using nodal design variables and projection functions,” *Int J Numer Methods Eng*, vol. 61, no. 2, pp.238-254, 2004.

[B52] J. Guest, “Imposing maximum length scale in topology optimization,” *Struct Multidisc Optim*, vol. 37, no. 5, pp.463-473, 2009.

[B53] J. Guest, “Topology optimization with multiple phase projection,” *Comput Methods Appl Mech Eng*, vol. 199, no. 1-4, pp.123-135, 2009.

[B54] S. Zhou, and M. Wang, “Multi-material structural topology optimization with a generalized Cahn–Hilliard model of multiphase transition,” *Struct Multidisc Optim*, vol. 33, no. 2, pp.89-111, 2007.

[B55] G. Allaire, F. Jouve F, and A. Toader, “Structural optimization using sensitivity analysis and a level-set method,” *J Comput Phys*, vol. 194, no. 1, pp.363-393, 2004.

[B56] H. Ho, B. Lui, and M. Wang, “Parametric structural optimization with radial basis functions and partition of unity method,” *Optim Methods Softw*, vol. 26, no. 4-5, pp.533-553, 2011.

[B57] A. Kawamoto, and et al., “Heaviside projection-based topology optimization by a PDE-filtered scalar function,” *Struct Multidisc Optim* vol. 44, no. 1, pp.19-24, 2011.

[B58] S. Kreissl, G. Pingen, and K. Maute, “An explicit level set approach for generalized shape optimization of fluids with the lattice Boltzmann method,” *Int J Numer Methods Fluids*, vol. 65, no. 5, pp.496-519, 2011.

[B59] T. Yamada, K. Izui, S. Nishiwaki, A. Takezawa, “A topology optimization method based on the level set method incorporating a fictitious interface energy,” *Comput Methods Appl Mech Eng*, vol. 199, pp.2876-2891, 2010.

[B60] M. Otomori, T. Yamada, K. Izui, and S. Nishiwaki, “Level set-based topology optimization of a compliant mechanism design using mathematical programming,” *Mech Sci*, vol. 2, no. 1, pp.91-98, 2011.

[B61] V. Challis, and J. Guest, “Level set topology optimization of fluids in Stokes flow,” *Int J Numer Methods Eng*, vol. 79, no. 10, pp.1284-1308, 2009.

[B62] S. Lim, T. Yamada, S. Min, and S. Nishiwaki, “Topology optimization of a magnetic actuator based on a level set and phase-field approach,” *IEEE Trans Magn*, vol. 47, no. 5, pp.1318-1321, 2011.

[B63] L. He, C. Kao, and S. Osher, “Incorporating topological derivatives into shape derivatives-based level set methods,” *J Comput Phys*, vol. 225, no. 1, pp.891-909, 2007.

[B64] J. C´ea, S. Garreau, P. Guillaume, and M. Masmoudi, “The shape and topological optimizations connection,” *Comput Methods Appl Mech Eng*, vol. 188, no. 4, pp.713-726, 2000.

[B65] J. Sokołowski, and A. Zochowski, “On the topological derivative in shape optimization,” *SIAM J Control Optim*, vol. 37, no. 4, pp.1251-1272, 1999.

[B66] J. Sokołowski, and A. Zochowski, “Topological derivatives of shape functionals for elasticity systems,” *Mech Struct Mach*, vol. 29, no. 3, pp.331-349, 2001.

[B67] S. Garreau, P. Guillaume, and M. Masmoudi, “The topological asymptotic for PDE systems: the elasticity case,” *SIAM J Control Optim*, vol. 39, pp.1756, 2001.

[B68] A. Groenwold, and L. Etman, “A quadratic approximation for structural topology optimization,” *Int J Numer Methods Eng*, vol. 82, no. 4, pp.505-524, 2010.

[B69] M. Bruyneel, P. Duysinx, and C. Fleury, “A family of MMA approximations for structural optimization,” Struct Multidisc Optim, vol. 24, no. 4, pp.263-276, 2002.

[B70] J. Sethian, and A. Wiegmann, “Structural boundary design via level set and immersed interface methods,” *J Comput Phys*, vol. 163, no. 2, pp.489-528, 2000.

[B71] L. Chen, “Phase-field models for microstructure evolution,” Annu Rev Mater Res, vol. 32, no. 32, pp.113-140, 2002.

[B72] L. Blank, and et al., “Phase-field approaches to structural topology optimization,” Int Ser Numer Math, vol. 160, pp.245-256, 2010.

[B73] A. Gain, and G. Paulino, “Phase-field topology optimization with polygonal elements: a finite volume approach for the evolution equation,” Struct Multidiscip Optim, vol. 46, no. 3, pp.327-342, 2012.

[B74] R. Jin, X. Du, and W. Chen, “The use of metamodeling techniques for optimization under uncertainty,” Struct Multidiscip Optim, vol. 25, pp.99-116, 2003.

[B75] M. Asher, B. Croke, A. Jakeman, and L. Peeters, “A review of surrogate models and their application to groundwater modeling,” Water Resources Research, vol. 51, no. 8, pp.5957-5973, 2015.

[B76] A. Forrester, and A. Keane, “Recent advances in surrogate-based optimization,” Progress in aerospace sciences, vol. 45, no.1-3, pp.50-79, 2009.

[B77] N. Queipo, and et al., “Surrogate-based analysis and optimization,” Progress in aerospace sciences, vol. 41, no. 1, pp.1-28, 2005.

[B78] B. Tang, “Orthogonal array-based Latin hypercubes,” J Am Stat Assoc vol. 88, pp.1392-1398, 1993.

[B79] A. Owen, “Orthogonal Arrays for Computer Experiments, Integration, and Visualization,” Stat. Sin., vol. 2, pp.439-452, 1992.

[B80] S. Leary, A. Bhaskar, and A. Keane, ‘Optimal orthogonal-array-based Latin hypercubes,” Journal of Applied Statistics, vol. 30, no. 5, pp.585-598, 2003.

[B81] E. Ostertagová, “Modelling using polynomial regression,” Procedia Engineering, vol. 48, pp.500-506, 2012.

[B82] J. Sacks, J. Welch, T. Mitchell, and H. Wynn, “Design and analysis of computer experiments,” Statistical science, pp.409-423, 1989.

[B83] I. Couckuyt, and et al., “Blind Kriging: Implementation and performance analysis,” Advances in Engineering Software, vol. 49, pp.1-13, 2012.

[B84] Y. Zhang, W. Yao, X. Chen, and S. Ye, “A penalized blind likelihood Kriging method for surrogate modeling,” Structural and Multidisciplinary Optimization, vol. 61, no. 2, pp.457-474, 2020.

[B85] R. Jin, W. Chen, and T. Simpson, “Comparative studies of metamodeling techniques under multiple modelling criteria,” Struct Multidiscip Optim, vol. 23, no. 1, pp.1-13, 2001.

[B86] S. Sakata, F. Ashida, and M. Zako, “An efficient algorithm for Kriging approximation and optimization with large-scale sampling data,” Computer methods in applied mechanics and engineering, vol. 193, no. 3-5, pp.385-404, 2004.

[B87] M. Bouhlel, N. Bartoli, A. Otsmane, and J. Morlier, “Improving Kriging surrogates of high-dimensional design models by Partial Least Squares dimension reduction,” Structural and Multidisciplinary Optimization, vol. 53, no. 5, pp.935-952, 2016.

[B88] R. Barry, and R. Pace, “Kriging with large data sets using sparse matrix techniques,” *Communications in Statistics-Simulation and Computation*, vol. 26, no. 2, pp.619-629, 1997.

[B89] R. Regis, “Evolutionary programming for high-dimensional constrained expensive black-box optimization using radial basis functions,” *IEEE Transactions on Evolutionary Computation*, vol. 18, no. 3, pp.326-347, 2014.

[B90] G. Lei, and et al., “Electromagnetic device design based on RBF models and two new sequential optimization strategies,” *IEEE Transactions on Magnetics*, vol. 46, no. 8, pp.3181-3184, 2010.

[B91] S. Amaran, N. Sahinidis, B. Sharda, and S. Bury, “Simulation optimization: a review of algorithms and applications,” *Annals of Operations Research*, vol. 240, no. 1, pp.351-380, 2016.

[B92] M. Niu, C. Wan, and Z. Xu, “A review on applications of heuristic optimization algorithms for optimal power flow in modern power systems,” *Journal of Modern Power Systems and Clean Energy*, vol. 2, no. 4, pp.289-297, 2014.

[B93] O. Granichin, and N. Amelina, “Simultaneous perturbation stochastic approximation for tracking under unknown but bounded disturbances,” *IEEE Transactions on Automatic Control*, vol. 60, no. 6, pp.1653-1658, 2015.

[B94] J. Maryak, and D. Chin, “Global random optimization by simultaneous perturbation stochastic approximation,” *IEEE Transactions on Automatic Control*, vol. 53, pp.780-783, 2008.

[B95] J. Spall, “Feedback and weighting mechanisms for improving Jacobian estimates in the adaptive simultaneous perturbation algorithm,” *IEEE Transactions on Automatic Control*, vol. 54, no. 6, pp.1216-1229, 2009.

[B96] R. Hooke, and T. Jeeves, “Direct search solution of numerical and statistical problems,” *Journal of the Association for Computing Machinery*, vol. 8, pp.212-219, 1961.

[B97] D. Olsson, and L. Nelson, “The Nelder-Mead simplex procedure for function minimization,” *Technometrics*, vol. 17, no. 1, pp.45-51, 1975.

[B98] K. Choi, and et al., “Hybrid algorithm combing genetic algorithm with evolution strategy for antenna design,” *IEEE Transactions on Magnetics*, vol. 52, no. 3, Article no. 7209004, 2016.

[B99] M. Kumari, and M. Sydulu, “A fast computational genetic algorithm for economic load dispatch,” *Int J Recent Trends Eng*, vol. 1, no. 1, pp.349-356, 2009.

[B100] K. Srinivasa, K. Venugopal, and L. Patnaik, “A self-adaptive migration model genetic algorithm for data mining applications,” *Inf Sci*, vol. 177, no. 20, pp.4295-4313, 2007.

[B101] J. Zhang, J. Zhuang, H. Du, and S. Wang, “Self-organizing genetic algorithm-based tuning of PID controllers,” *Inf Sci*, vol. 179, no. 7, pp.1007-1018, 2009.

[B102] S. Tongchim, and P. Chongstitvatana P, “Parallel genetic algorithm with parameter adaptation,” *Inf Process Lett*, vol. 82, no. 1, pp.47-54, 2002.

[B103] B. Mahdad, K. Srairi, and T. Bouktir, “Optimal power flow for large-scale power system with shunt FACTS using efficient parallel GA,” *Electr Power Energy Syst*, vol. 32, no. 5, pp.507-517, 2010.

[B104] V. Togan, and A. Daloglu, “An improved genetic algorithm with initial population strategy and self-adaptive member grouping,” *Comput Struct*, vol. 86, no. 12, pp.1204-1218, 2008.

[B105] H. Alkhatib, J. Duveau, “Dynamic genetic algorithms for robust design of multimachine power system stabilizers,” *Electr Power Energy Syst*, vol. 45, pp.242-251, 2013.

[B106] S. Ahmed, “Automatic generation of basis test paths using variable length genetic algorithm,” *Inf Process Lett*, vol. 114, no. 6, pp.304-316, 2014.

[B107] A. Malossini, E. Blanzieri and T. Calarco, “Quantum genetic optimization,” *IEEE Transactions on Evolutionary Computation*, vol. 12, no. 2, pp.231-241, 2008.

[B108] Y. Wang, X. Geng, F. Zhang and J. Ruan, “An immune genetic algorithm for multi-echelon inventory cost control of IOT based supply chains,” *IEEE Access*, vol. 6, pp.8547-8555, 2018.

[B109] K. Deb, A. Pratap, S. Agarwal and T. Meyarivan, “A fast and elitist multiobjective genetic algorithm: NSGA-II,” *IEEE Transactions on Evolutionary Computation*, vol. 6, no. 2, pp.182-197, 2002.

[B110] Y. Tominaga, Y. Okamoto, S. Wakao and S. Sato, “Binary-based topology optimization of magnetostatic shielding by a hybrid evolutionary algorithm combining genetic algorithm and extended compact genetic algorithm,” *IEEE Transactions on Magnetics*, vol. 49, no. 5, pp.2093-2096, 2013.

[B111] K. Choi, and et al., “Hybrid algorithm combing genetic algorithm with evolution strategy for antenna design,” *IEEE Transactions on Magnetics*, vol. 52, no. 3, Article no. 7209004, 2016.

[B112] J. Luo, and et. al, “A new level set method for systematic design of hinge-free compliant mechanisms,” *Computer Methods in Applied Mechanics and Engineering*, vol. 198, no. 2, pp. 318-331, 2008.

[B113] J. Kennedy and R. Eberhart, “Particle swarm optimization,” *Proceedings of ICNN'95 - International Conference on Neural Networks*, Perth, WA, Australia, vol. 4, pp.1942-1948, 1995.

[B114] K. Parsopoulos, and M. Vrahatis, “On the computation of all global minimizers through particle swarm optimization,” *IEEE Trans Evol Comput*, vol. 8, no. 3, pp.211-224, 2004.

[B115] X. Yang, J. Yuan, J. Yuan, and H. Mao, “A modified particle swarm optimizer with dynamic adaptation,” *J Appl Math Comput*, vol. 189, pp.1205-1213, 2007.

[B116] Z. Zhan, J. Zhang, Y. Li, and Y. Shi, “Orthogonal learning particle swarm optimization,” *IEEE Trans Evolut Comput*, vol. 15, no. 6, pp.832-847, 2011.

[B117] T. Nikna, H. Mojarrad, and M. Nayeripour, “A new fuzzy adaptive particle swarm optimization for non-smooth economic dispatch,” *Energy*, vol. 35, pp.1764-1778, 2010.

[B118] B. Firouzia, E. Farjah, and R. Abarghooee, “An efficient scenario-based and fuzzy self-adaptive learning particle swarm optimization approach for dynamic economic emission dispatch considering load and wind power uncertainties,” *Energy*, vol. 50, no. 1, pp.232-244, 2013.

[B119] R. Akbari, and K. Ziarati, “A rank-based particle swarm optimization algorithm with dynamic adaptation,” *J Comput Appl Math*, vol. 235, pp.2694-2714, 2011.

[B120] Y. Pehlivanoglu, “A new particle swarm optimization method enhanced with a periodic mutation strategy and neural networks,” *IEEE Trans Evolut Comput*, vol. 17, no. 3, pp.436-452, 2013.

[B121] A. Safari, H. Shayanfar and A. Kazemi, “Robust PWMSC damping controller tuning on the augmented lagrangian PSO algorithm,” *IEEE Transactions on Power Systems*, vol. 28, no. 4, pp.4665-4673, 2013.

[B122] Y. Wang, and et al., “An improved self-adaptive PSO technique for short-term hydrothermal scheduling,” *Expert Systems with Applications*, vol. 39, no. 3, pp.2288-2295, 2012.

[B123] B. Tran, B. Xue, and M. Zhang, “A new representation in PSO for discretization-based feature selection,” *IEEE Transactions on Cybernetics*, vol. 48, no. 6, pp.1733-1746, 2017.

[B124] M. Gonzalez, A. López, and F. Jurado, “Optimization of distributed generation systems using a new discrete PSO and OPF,” *Electric power systems research*, vol. 84, no. 1, pp.174-180, 2012.

[B125] G. Zavala, A. Nebro, F. Luna, and C. Coello, “A survey of multi-objective metaheuristics applied to structural optimization,” *Structural and Multidisciplinary Optimization*, vol. 49, no. 4, pp. 537-558, 2014.

[B126] S. Lalwani, S. Singhal, R. Kumar, and N. Gupta, “A comprehensive survey: Applications of multi-objective particle swarm optimization (MOPSO) algorithm,” *Transactions on combinatorics*, vol. 2, no. 1, pp.39-101, 2013.

[B127] P. Tripathi, S. Bandyopadhyay, and S. Pal, “Multi-objective particle swarm optimization with time variant inertia and acceleration coefficients,” *Information sciences*, vol. 177, no. 22, pp.5033-5049, 2007.

[B128] Y. Zhang, D. Gong, and J. Zhang, “Robot path planning in uncertain environment using multi-objective particle swarm optimization,” *Neurocomputing*, vol. 103, pp.172-185, 2013.

[B129] C. Goh, and et al., “A competitive and cooperative co-evolutionary approach to multi-objective particle swarm optimization algorithm design,” *European Journal of Operational Research*, vol. 202, no. 1, pp.42-54, 2010.

[B130] B. Xue, M. Zhang, and W. Browne, “Particle swarm optimization for feature selection in classification: A multi-objective approach,” *IEEE transactions on cybernetics*, vol. 43, no. 6, pp.1656-1671, 2012.

[B131] Y. Xie, and G. Steven, “A simple evolutionary procedure for structural optimization,” *Computers and structures*, vol. 49, no. 5, pp.885-896, 1993.

[B132] X. Yang, and et al., “Bi-directional evolutionary method for stiffness optimization,” *AIAA journal*, vol. 37, no. 11, pp.1483-1488, 1999.

[B133] O. Querin, G. Steven, and Y. Xie, “Evolutionary structural optimization using an additive algorithm,” *Finite elements in Analysis and Design*, vol. 34, no. 3-4, pp.291-308, 2000.

[B134] V. Young, O. Querin, G. Steven, and Y. Xie, “3-D and multiple load case bi-directional evolutionary structural optimization (BESO),” *Structural optimization*, vol. 18, no. 2-3, pp.183-192, 1999.

[B135] Y. Tang, A. Kurtz, and Y. Zhao, “Bidirectional Evolutionary Structural Optimization (BESO) based design method for lattice structure to be fabricated by additive manufacturing,” *Computer-Aided Design*, vol. 69, pp.91-101, 2015.

[B136] X. Yang, X. Huang, J. Rong, and Y. Xie, “Design of 3-D orthotropic materials with prescribed ratios for effective Young’s moduli,” *Computational materials science*, vol. 67, pp.229-237, 2013.

[B137] S. Choi, S. Kim, J. Park, and S. Han, “Multi-objective optimization of the inner reinforcement for a vehicle’s hood considering static stiffness and natural frequency,” *International journal of automotive technology*, vol. 8, no. 3, pp.337-342. 2007.

[B138] N. Noilublao, and S. Bureerat, “Simultaneous topology, shape and sizing optimization of a three-dimensional slender truss tower using multi-objective evolutionary algorithms,” *Computers and Structures*, vol. 89, no. 23-24, pp.2531-2538, 2011.

[B139] P. Tanskanen, “The evolutionary structural optimization method: theoretical aspects,” *Computer methods in applied mechanics and engineering*, vol. 191, no. 47-48, pp. 5485-5498, 2002.

[B140] C. Edwards, H. Kim, and C. Budd, “An evaluative study on ESO and SIMP for optimizing a cantilever tie-beam,” *Structural and Multidisciplinary Optimization*, vol. 34, no. 5, pp.403-414, 2007.

[B141] S. Das, S. Mullick, and P. Suganthan, “Recent advances in differential evolution-an updated survey,” *Swarm and Evolutionary Computation*, vol. 27, pp.1-30, 2016.

[B142] T. Marcic, and et al., “Determining parameters of a line-start interior permanent magnet synchronous motor model by the differential evolution,” *IEEE Transactions on Magnetics*, vol. 44, no. 11, pp.4385-4388, 2008.

[B143] J. Malagoli, and et al., “Design of three-phase induction machine using differential evolution algorithm,” *IEEE Latin America Transactions*, vol. 13, no. 7, pp.2202-2208, 2015.

[B144] Z. Yin, and et al., “Integrated position and speed loops under sliding-mode control optimized by differential evolution algorithm for PMSM drives,” *IEEE Transactions on Power Electronics*, vol. 34, no. 9, pp.8994-9005, 2019.

[B145] P. Kuila, and P. Jana, “A novel differential evolution-based clustering algorithm for wireless sensor networks,” *Applied soft computing*, vol. 25, pp.414-425, 2014.

[B146] S. Gundry, and et al., “Differential evolution-based autonomous and disruption tolerant vehicular self-organization in MANETs,” *Ad Hoc Networks*, vol. 25, pp.454-471, 2015.

[B147] P. Rocca, G. Oliveri, and A. Massa, “Differential evolution as aApplied to electromagnetics,” *IEEE Antennas and Propagation Magazine*, vol. 53, no. 1, pp.38-49, 2011.

[B148] A. Deb, J. Roy, and B. Gupta, “Performance comparison of differential evolution, particle swarm optimization and genetic algorithm in the design of circularly polarized microstrip antennas,” *IEEE transactions on antennas and propagation*, vol. 62, no. 8, pp.3920-3928, 2014.

[B149] P. Mahouti, “Design optimization of a pattern reconfigurable microstrip antenna using differential evolution and 3-D EM simulation‐based neural network model,” *International Journal of RF and Microwave Computer‐Aided Engineering*, vol. 29, no. 8, Article no. 21796, 2019.

[B150] S. Kirkpatrick, C. Gelatt, and M. Vecchi, “Optimization by simulated annealing,” *Science*, vol. 220, no. 4598, pp.671-680, 1983.

[B151] S. Ho, S. Yang, H. Wong, and G. Ni, “A simulated annealing algorithm for multi-objective optimizations of electromagnetic devices,” *IEEE Transactions on Magnetics*, vol. 39, no. 3, pp.1285-1288, 2003.

[B152] S. Alfonzetti, E. Dilettoso, and N. Salerno, “Simulated annealing with restarts for the optimization of electromagnetic devices,” *IEEE Transactions on Magnetics*, vol. 42, no. 4, pp.1115-1118, 2006.

[B153] S. Li, S. Ho, and S. Ho, “A novel orthogonal simulated annealing algorithm for optimization of electromagnetic problems,” *IEEE Transactions on Magnetics*, vol. 40, no. 4, pp.1791-1795, 2004.

[B154] Z. Qin, K. Cai, and X. Zou, “A reduced-complexity iterative receiver based on simulated annealing for coded partial-response channels,” *IEEE Transactions on Magnetics*, vol. 43, no. 6, pp.2265-2267, 2007.

[B155] R. Tang, J. Sun, Y. Li, and X. Cui, “Optimization of electromagnetic devices by using intelligent simulated annealing algorithm,” *IEEE Transactions on Magnetics*, vol. 34, no. 5, pp.2992-2995, 1998.

[B156] D. Fodorean, and et al., “Simulated annealing algorithm for the optimization of an electrical machine,” *IET Electric Power Applications*, vol. 6, no. 9, pp.735-742, 2012.

[B157] Z. Cao, and et al., “Optimal cloud computing resource allocation for demand side management in smart grid,” *IEEE Transactions on Smart Grid*, vol. 8, no. 4, pp.1943-1955, 2017.

[B158] F. Dababneh, and L. Li, “Integrated electricity and natural gas demand response for manufacturers in the smart grid,” *IEEE Transactions on Smart Grid*, vol. 10, no. 4, pp.4164-4174, 2019.

[B159] A. Hedar, and M. Fukushima, “Heuristic pattern search and its hybridization with simulated annealing for nonlinear global optimization,” *Optimization Methods and Software*, vol. 19, no. 3-4, pp.291-308, 2004.

[B160] B. Wang, H. Xie, X. Xia, and X. Zhang, “A NSGA-II algorithm hybridizing local simulated-annealing operators for a bi-criteria robust job-shop scheduling problem under scenarios,” *IEEE Transactions on Fuzzy Systems*, vol. 27, no. 5, pp.1075-1084, 2019.

[B161] D. Fouskakis, and D. Draper, “Stochastic optimization: a review,” *International Statistical Review*, vol. 70, no. 3, pp.315-349, 2002.

[B162] S. Carcangiu, A. Fanni, and A. Montisci, “Multi-objective tabu search algorithms for optimal design of electromagnetic devices,” I*EEE Transactions on Magnetics*, vol. 44, no. 6, pp.970-973, 2008.

[B163] S. Ho, S. Yang, G. Ni, and K. Cheng, “An efficient tabu search algorithm for robust solutions of electromagnetic design problems,” *IEEE Transactions on Magnetics*, vol. 44, no. 6, pp.1042-1045, 2008.

[B164] T. Datta, N. Srinidhi, A. Chockalingam, and B. S. Rajan, "Random-restart reactive tabu search algorithm for detection in large-MIMO systems," *IEEE Communications Letters*, vol. 14, no. 12, pp.1107-1109, 2010.

[B165] S. Ho, and S. Yang, "Multi-objective synthesis of antenna arrays using a vector tabu search algorithm," *IEEE Antennas and Wireless Propagation Letters*, vol. 8, pp.947-950, 2009.

[B166] Z. Wang, and et al., "A modified ant colony optimization algorithm for network coding resource minimization," *IEEE Transactions on Evolutionary Computation*, vol. 20, no. 3, pp.325-342, 2016.

[B167] N. Taspinar, A. Kalinli, and M. Yildirim, "Partial transmit sequences for PAPR reduction using parallel tabu search algorithm in OFDM systems," *IEEE Communications Letters*, vol. 15, no. 9, pp.974-976, 2011.

[B168] Y. Wang, R. Zhang, J. Li, and F. Shu, "PAPR reduction based on parallel tabu search for tone reservation in OFDM systems," *IEEE Wireless Communications Letters*, vol. 8, no. 2, pp. 576-579, 2019.

[B169] D. Karaboga, and B. Akay, "A comparative study of artificial bee colony algorithm," *Applied mathematics and computation*, vol. 214, no. 1, pp.108-132, 2009.

[B170] D. Karaboga, B. Gorkemli, C. Ozturk, and N. Karaboga, "A comprehensive survey: artificial bee colony (ABC) algorithm and applications," *Artificial Intelligence Review*, vol. 42, no. 1, pp.21-57, 2014.

[B171] Y. Wang, and et al., "Remaining useful life prediction of lithium-ion batteries using support vector regression optimized by artificial bee colony," *IEEE Transactions on Vehicular Technology*, vol. 68, no. 10, pp.9543-9553, 2019.

[B172] M. De. and S. K. Goswami, "Optimal reactive power procurement with voltage stability consideration in deregulated power system," *IEEE Transactions on Power Systems*, vol. 29, no. 5, pp.2078-2086, 2014.

[B173] L. Wang, X. Zhang, and X. Zhang, "Antenna array design by artificial bee colony algorithm with similarity induced search method," *IEEE Transactions on Magnetics*, vol. 55, no. 6, Article no. 7201904, 2019.

[B174] X. Ding, and et al., “Efficiency improvement of overall PMSM-inverter system based on artificial bee colony algorithm under full power range,” *IEEE Transactions on Magnetics*, vol. 52, no. 7, Article no. 8106904, 2016.

[B175] W. Yeh, et al., “Approximate reliability function based on wavelet latin hypercube sampling and bee recurrent neural network,” *IEEE Transactions on Reliability*, vol. 60, no. 2, pp.404-414, 2011.

[B176] J. Liu, and L. Meng, “Integrating artificial bee colony algorithm and BP neural network for software aging prediction in IoT environment,” *IEEE Access*, vol. 7, pp.32941-32948, 2019.

[B177] D. Chen, “Research on traffic flow prediction in the big data environment based on the improved RBF neural network,” *IEEE Transactions on Industrial Informatics*, vol. 13, no. 4, pp.2000-2008, 2017.

[B178] F. Xin, S. Ni, H. Li, and X. Zhou, “General regression neural network and artificial-bee-colony based general regression neural network approaches to the number of end-of-life Vehicles in China,” *IEEE Access*, vol. 6, pp.19278-19286, 2018.

[B179] M. Dorigo, M. Birattari, and T. Stutzle, “Ant colony optimization,” *IEEE Computational Intelligence Magazine*, vol. 1, no. 4, pp.28-39, 2006.

[B180] V. Suresh, and et al., “Microgrid energy management system with embedded deep learning forecaster and combined optimizer,” *IEEE Access*, vol. 8, pp.202225-202239, 2020.

[B181] X. Liu, “A transmission scheme for wireless sensor networks using ant colony optimization with unconventional characteristics,” *IEEE Communications Letters*, vol. 18, no. 7, pp.1214-1217, 2014.

[B182] E. Tsampouris, P. Kakosimos, and A. Kladas, “Coupled computation of electric motor design and control parameters based on ant colonies speed trajectory optimization,” *IEEE Transactions on Magnetics*, vol. 49, no. 5, pp.2177-2180, 2013.

[B183] H. Jiang, K. Xie, and Y. F. Wang, “Novel design of flat gain spectrum raman fiber amplifiers based on ant colony optimization,” *IEEE Photonics Technology Letters*, vol. 23, no. 23, pp.1823-1825, 2011.

[B184] X. Yang, and X. He, “Firefly algorithm: recent advances and applications,” *International journal of swarm intelligence*, vol. 1, no. 1, pp.36-50, 2013.

[B185] Y. Huang, M. Huang, and C. Ye, “A fusion firefly algorithm with simplified propagation for photovoltaic MPPT under partial shading conditions,” I*EEE Transactions on Sustainable Energy*, vol. 11, no. 4, pp.2641-2652, 2020.

[B186] H. Huang, and S. Lin, “A hybrid metaheuristic embedded system for intelligent vehicles using hypermutated firefly algorithm optimized radial basis function neural network,” *IEEE Transactions on Industrial Informatics*, vol. 15, no. 2, pp.1062-1069, 2019.

[B187] A. Wagan, M. Shaikh, and R. Abro, “Wind turbine micrositing by using the firefly algorithm,” *Applied Soft Computing*, vol. 27, pp.450-456, 2015.

[B188] S. Sanajaoba, “Optimal sizing of off-grid hybrid energy system based on minimum cost of energy and reliability criteria using firefly algorithm,” *Solar Energy*, vol. 188, pp.655-666, 2019.

[B189] S. Abd-Elazim, and E. Ali, “Load frequency controller design of a two-area system composing of PV grid and thermal generator via firefly algorithm,” *Neural Computing and Applications*, vol. 30, no. 2, pp.607-616, 2018.

[B190] H. Su, B. Yong, and Q. Du, “Hyperspectral band selection using improved firefly algorithm,” *IEEE Geoscience and Remote Sensing Letters*, vol. 13, no. 1, pp.68-72, 2016.

[B191] S. Maslovski, S. Tretyakov, and P. Alitalo, “`Near-field enhancement and imaging in double planar polariton-resonant structures,'” *J. Appl. Phys.*, vol. 96, no. 3, pp. 1293-1300, 2004.

[B192] V. Veselago, “Electrodynamics of substances with simultaneously negative μ and ε ,” *Usp. Fiz. Nauk,* vol. 92, pp.517, 1967.

[B193] W. Lee and Y. Yoon, “Wireless power transfer systems using metamaterials: a review,” *IEEE Access*, vol. 8, pp.147930-147947, 2020.

[B194] B.Wang, and et al., “Experiments on wireless power transfer with metamaterials,” *Appl. Phys. Lett.*, vol. 98, no. 25, Article. no. 254101, 2011.

[B195] T. Duong and J. Lee, “Experimental results of high-efficiency resonant coupling wireless power transfer using a variable coupling method,” IEEE Microw. Wireless Compon. Lett., vol. 21, no. 8, pp.442-444, 2011.

[B196] R. Hamam, A. Karalis, J. Joannopoulos, and M. Solja£i¢, “Efficient weakly-radiative wireless energy transfer: An EIT-like approach,” *Ann. Phys.*, vol. 324, no. 8, pp.1783-1795, 2009.

[B197] Y. Zhang, and et al., “Selective wireless power transfer to multiple loads using receivers of different resonant frequencies,” *IEEE Trans. Power Electron.*, vol. 30, no. 11, pp.6001-6005, 2015.

[B198] B. Wang, T. Nishino, and K. Teo, “Wireless power transmission efficiency enhancement with metamaterials,” in *Proc. IEEE Int. Conf. Wireless Inf. Technol. Syst.*, Honolulu, HI, USA, pp.1-4, 2010.

[B199] A. Bhattacharya, T. Shaw, and D. Mitra, “Performance enhancement of wireless power transfer system by controlling transmission and rejection properties of metamaterials,” in *Proc. IEEE MTT-S Int. Microw. RF Conf. (IMaRC)*, Kolkata, India, pp.1-4, 2018.

[B200] T. Shaw, A. Roy, and D. Mitra, “Efficiency enhancement of wireless power transfer system using MNZ metamaterials,” *Prog. Electromagn. Res. C*, vol. 68, pp.11-19, 2016.

[B201] X. Wang, and et al. “Analysis of wireless power transfer using superconducting metamaterials,” *IEEE Transactions on Applied Superconductivity*, vol. 29, no. 2, Article no. 5500605, 2019.

[B202] J. Chen, and et al., “Metamaterial-based high-efficiency wireless power transfer system at 13.56 MHz for low power applications,” *Progress In Electromagnetics Research*, vol. 72, pp.17-30, 2017.

[B203] J. Chen and H. Tan, “Metamaterial for wireless power transfer system at 13.56MHz with coil misalignment,” *2017 7th IEEE International Symposium on Microwave, Antenna, Propagation, and EMC Technologies (MAPE)*, Xi'an, pp.313-317, 2017.

[B204] W. Xin, et al. “Investigation of negative permeability metamaterials for wireless power transfer,” *AIP Advances*, vol. 7, no. 11, Article no. 115316, 2017.

[B205] W. Li, and et al. “Experimental investigation of 1D, 2-D, and 3-D metamaterials for efficiency enhancement in a 6.78 MHz wireless power transfer system,” In *2016 IEEE Wireless Power Transfer Conference (WPTC)*, pp.1-4, 2016.

[B206] A. Ranaweera, C. Moscoso, and J. Lee, “Anisotropic metamaterial for efficiency enhancement of mid-range wireless power transfer under coil misalignment,” *Journal of Physics D: Applied Physics*, vol. 48, no. 45, Article no. 455104, 2015.

[B207] C. Rong, et al., “Analysis and optimized design of metamaterials for mid-range wireless power transfer using a class-E RF power amplifier,” *Applied Sciences*, vol. 9, no. 1, pp. 26, 2018.

[B208] C. Lu, and et al., “Investigation of negative and near-zero permeability metamaterials for increased efficiency and reduced electromagnetic field leakage in a wireless power transfer system,” *IEEE Transactions on Electromagnetic Compatibility*, vol. 61, no. 5, pp.1438-1446, 2018.

[B209] H. Kim, and C. Seo, “Highly efficient wireless power transfer using metamaterial slab with zero refractive property,” *Electronics letters*, vol. 50, no. 16, pp.1158-1160, 2014.

[B210] Y. Cho, and et al., “Thin hybrid metamaterial slab with negative and zero permeability for high efficiency and low electromagnetic field in wireless power transfer systems,” *IEEE Transactions on Electromagnetic Compatibility*, vol. 60, no. 4, pp.1001-1009, 2018.

[B211] J. Wu, B. Wang, W. Yerazunis, and K. Teo, “Wireless power transfer with artificial magnetic conductors,” *2013 IEEE Wireless Power Transfer (WPT)*, Perugia, pp.155-158, 2013.

[B212] S. Zhu, and et al., “Enhancement of wireless power transmission based on side-positioned metamaterials,” *2018 IEEE PES Asia-Pacific Power and Energy Engineering Conference (APPEEC)*, Kota Kinabalu, pp. 241-245, 2018.

[B213] J. Chen, and H. Tan, “Investigation of wireless power transfer with 3-D metamaterial for efficiency enhancement,” *2017 7th IEEE International Symposium on Microwave, Antenna, Propagation, and EMC Technologies (MAPE), Xi'an*, pp.309-312, 2017.

[B214] E. Rodríguez, A. RamRakhyani, D. Schurig, and G. Lazzi, “Compact low-frequency metamaterial design for wireless power transfer efficiency enhancement,” *IEEE Transactions on Microwave Theory and Techniques*, vol. 64, no. 5, pp.1644-1654, 2016.

[B215] A. Ranaweera, T. Duong, B. Lee, and J. Lee, “Experimental investigation of 3-D metamaterial for mid-range wireless power transfer,” *2014 IEEE Wireless Power Transfer Conference*, Jeju, pp.92-95, 2014.

[B216] G. Lipworth, and et al., “Magnetic metamaterial superlens for increased range wireless power transfer,” *Scientific reports*, vol. 4, pp. 3642, 2015.

[B217] R. Das, A. Basir, and H. Yoo, “A metamaterial-coupled wireless power transfer system based on cubic high-dielectric resonators,” *IEEE Transactions on Industrial Electronics*, vol. 66, no. 9, pp.7397-7406, 2018.

[B218] S. Arslanagić, and et al., “A review of the scattering-parameter extraction method with clarification of ambiguity issues in relation to metamaterial homogenization,” *IEEE Antennas and Propagation Magazine*, vol. 55, no. 2, pp.91-106, 2013.

Chapter 3 Robust Optimization of 2-D and 3-D electromagnetic problems

The performance optimization of electromagnetic devices often involves the optimization of a device topology with respect to a single and important objective function. However, when the complexity of the problem is high, a single objective optimization problem could be time consuming and requires specially calibrated algorithms as well. Moreover, when there are uncertainties presented in the modeling and the fabrication process, the performance and the robustness of the device need to be considered simultaneously, which makes the topology optimization problem more complicated. In this chapter, numerical methodologies and algorithms dealing with complex 3-D electromagnetic optimization problem and 2-D electromagnetic robust optimization problem are presented.

3.1 Introduction to Robust Optimization

In the fabrication and manufacturing processes of a topology optimized electromagnetic device, fabrication errors and uncertainties are often inevitable, and the accuracy of the production is highly limited by the state-of-art of the current manufacturing technology. Hence, if the optimized solution is very sensitive to small variations in the decision parameters, it is possible that a slight perturbation in the decision parameters could lead to either a serious performance degradation or an infeasible solution. The feasibly optimal design is thus not the traditionally defined optimal solution in terms of only the quality performance parameter (objective function) but should be defined as the one/ones that has/have high performances in both quality and robustness performances. In this point of view, increasing efforts have been devoted to the developments of robust optimization techniques in the design optimization of electromagnetic devices under uncertainties. Consequently, a wealth of robust oriented optimization techniques have been developed and applied

successfully to solve different engineering design problems with uncertainties[C1-C3].

Robustness measures the degree of insensitivity of the system or device to small perturbations in either the design or environmental variables, and in this thesis, robustness is defined as the stability of a potential design when there are errors or uncertainties in the design parameters. To quantify the uncertainty, there are two different approaches: the probability-based and the interval-based approaches [C4]. The probability-based approach uses some probabilistic information of the uncertainty, commonly the mean (expected fitness) and the standard deviation, of the objective function values within a certain range, as the gauges to assess the robustness of a solution. However, the distribution probability of the uncertainty is unknown before the design of a product, and often is estimated using a Gaussian distribution [C2], and also the robustness of the final solution cannot be guaranteed completely owing to the intrinsic properties of the uncertain probability distributions [C4]. The interval-based method simply uses the nominal value and the bounds of the uncertain parameters, and the worst-case scenario is sometimes used as the robust performance. Indeed, it is also hard, in some cases, to determine the bounds of interval uncertainties. However, for example, although it is usually very difficult to produce a product in exact accordance with the designed dimensional specifications due to the unknown manufacturing errors, one does know the error bounds of the manufacturing machine in advance. In other words, one only knows the bounds of uncertainties of the manufacturing errors in a special dimensional parameter. In this point of view, the interval uncertainty is a more practical way to estimate the uncertainties and errors in engineering problems, and the interval-based approach is a more practical and convenient method in an interval uncertainty quantization. An ensemble of tens or even hundreds of function-calls in a small neighborhood of a given solution is sampled and their function values are used to quantify the robustness in either the probability-based or the interval-based approaches. As a result, the computational burden for a robust optimizer is significantly higher than that for its global counterpart, especially for the complex optimization problems with longer objective function evaluation time. Under the condition that the objective function is continuously differentiable,

especially in cases that the expected fitness function is used as the robust parameter, the local optimal and boundary solutions have the potential to be a robust optimal solution [C5]. In this regard, the original objective function should be selected as the biasing force of a robust optimizer to stimulate enough competitive pressure to evolve to the robust optimal solution. To avoid these disadvantages in existing robust optimization techniques, an efficient direct search methodology is proposed.

3.2 A Direct Search Methodology for Robust Optimizations

3.2.1 New Formulation of a Robust Design Optimization

Generally, the constrained minimization problem with an interval uncertainty can be formulated as [C3]:

$$\begin{aligned} &\min f(x+\delta) \\ &s.t.\ \ \mathrm{g}_i(x+\delta) \le 0 \quad (i=1,2,...,k) \\ &\qquad \delta_N - \delta_0 \le \delta \le \ \delta_N + \delta_0 \end{aligned} \tag{3.1}$$

where x is the vector of design (decision) parameters (variables), δ is the vector of uncertainty variables, δ_N is the vector of the nominal value of δ, δ_0 is the vector of the half range of the interval uncertainty. In there, the standard deviation and the worst-case metric are used as the robust performance parameters, respectively, for the objective and hard constraint functions [C3]:

$$\begin{aligned} &\sigma[f(x+\delta)] = \sqrt{\sum_{1}^{N_S}\left\{ f(x_i+\delta_N) - \overline{f}(x_i+\delta_N)\right\}^2 / N_S} \\ &(g_i)_w(x) = \max_{\delta_N-\delta_0 \le \delta \le \ \delta_N+\delta_0} \left[g_i(x+\delta) \right] \end{aligned} \tag{3.2}$$

where N_S is the number of total sampling points generated in a small neighborhood of the specific point in the design space, x. In most of the existing robust optimization methodologies, the robust counterparts of the original design problem formulated by equation 3.1, as defined in equation 3.2, are either simply solved in lieu of the original optimal design problem or combined with the original quality performance parameter

to transfer the original design to a multi-objective optimization problem to seek the robust optimal solution. In other words, the robust performance is used as a predominant parameter in determining the searching direction of a robust optimizer in the optimization process. However, as explained previously, under certain condition the objective function is continuously differentiable, especially in cases that the expected fitness function is used as the robust parameter, the local optimal and boundary solutions have the potential to be a robust optimal solution. In this regard, the original objective function should be selected as the biasing force to stimulate enough competitive pressure to evolve to the robust optimal solution. Consequently, the proposed robust optimization formulation is directly formulated as:

$$\begin{aligned} &\min\ f(x+\delta_N) \\ &s.t.\ \ g_i(x+\delta_N) \le 0 \quad (i=1,2,3,...,k) \end{aligned} \tag{3.3}$$

Together with:

$$\begin{cases} \sigma[f(x+\delta)] \le \Delta_{tolerence} \\ (g_i)_w(x+\delta) - g_i(x+\delta_N) \le (\Delta g_i)_{tolerence} \\ \delta_N - \delta_0 \le \delta \le \ \delta_N + \delta_0 \end{cases} \tag{3.4}$$

where $\Delta_{tolerence}$ is the acceptable tolerance of $\sigma[f(x+\delta)]$, $(\Delta g_i)_{tolerence}$ is the acceptable tolerance of constraint function $g_i(x+\delta)$. An improper tolerance may slow down the convergence rate, especially when the tolerance is too small, it may result in infeasible solutions. In this regard, it is suggested that one uses a trial-and-error approach to determine the approximate tolerances before the optimizations.

3.2.2 A Robust Oriented Quantum-Inspired Evolutionary Algorithm

Despite the fact that any evolutionary algorithm can be used to find the robust optimal solution of the problem formulated in equation 3.3 and equation 3.4, the quantum-inspired evolutionary algorithm (QEA) [C6] is extended to a robust oriented optimizer due to its inherent characteristics in developing an efficient robust optimizer. QEA is a stochastic searching algorithm developed by applying quantum physics and quantum computing principles to classical evolutionary algorithms [C6-C8]. In

conventional EA, each induvial or possible solution is represented by an array of binary bit. Since instead of binary bits, the quantum bits, or *Q*-bits, are used in QEA to represent the input parameters, the method can obtain a good balance between global explorations and local exploitations during its searching process, and also is more appropriate for continuous problems. Moreover, it is demonstrated that EAs with a *Q*-bit probabilistic representation do have better characteristics in terms of population diversities [C7].

(1) Automatic Updating of the Increment Angle

To use the global statistical information extracted from the previous searches to build the probability distribution model of promising solutions, a rotation gate is used in QEA. Normally, a constant increment angle, $\Delta\theta$ is used in the rotation operation. It can be observed, however, that a large $\Delta\theta$ may result in a premature convergence, while a small $\Delta\theta$ will slow down the convergence speed [C9]. Moreover, in the optimization process of an ideal evolutionary algorithm, the standard deviation of the population will be reduced continuously. In these points of view, the standard deviation of the population is used to design an automatic updating mechanism for $\Delta\theta$ in the proposed robust oriented QEA:

$$\Delta\theta = \frac{e}{1+e}\left[1+e^{-\frac{\sigma(i)}{\sigma(1)}}\right]\Delta\theta_{\min} \tag{3.5}$$

where, $\sigma(i)$ is the standard deviation of the objective values of all individuals in the ith generation, $\Delta\theta_{\min}$ is the smallest increment angle. At the early stage of the searching process, the proposed robust oriented QEA uses a relatively small $\Delta\theta$ to modify the *Q*-bit individuals to guarantee the diversity of the generated population. However, the algorithm will focus its exploiting searches around the so far searched robust optimal solutions to enhance convergence performances in the final stage of the searches using a relatively large $\Delta\theta$.

(2) Robust Constraints Checking

Under certain conditions or in certain problems, the objective function is

continuously differentiable, for instance, in a problem where the expected fitness function is used as the robust parameter. The local/global optimum of the objective function or a solution distributed on the boundaries of the feasible parameter space has the potential to be the robust optimal solution of a constrained optimal design problem. In this point of view, it is unnecessary to check the robust performance constraints in equation 3.4 for every intermediate individual which is generated by observing the *Q*-bit individual. However, it is not easy to identify if an intermediate solution is a potential robust one in the optimization process. Nevertheless, from the iterative procedures of the proposed QEA, it is obvious that only the best and boundary solutions ever searched in current iteration have the potential to be a global or local optimum. This salient feature leads to the fact that the proposed algorithm is ideal for developing an efficient and simple robust optimizer since one needs only to check the robust performance constraints of those potential optimal solutions. In this point of view, a simple strategy to activate the robust performance checking procedure is proposed. More specially, in the iterative process, the robust performance feasibility checking of equation 3.4 is activated only when a new best solution/a boundary solution, x^*, is searched/generated and if $\left\|\nabla f(x^*)\right\|_2$ is smaller than a predefined value. Hence, the robust performance feasibility checking of the mere potential solutions rather than the total intermediate ones will reduce a huge amount of computation costs. For some complex objective functions and extreme cases such as minimizing the robust performance of the worst-case scenario of the original objective functions, the robust solution may be any point close to a local minimum. In this situation, the proposed robust constraints checking methodology should be modified to suit the special applications.

(3) Application of Stochastic Approximation

To determine the partial gradients, $\left\|\nabla f(x^*)\right\|_2$, the finite-difference approach is readily applicable. Since such approach will compute only one partial derivative in one direction in one computation, it is computationally expensive or even prohibitive for problems with large decision parameters. To overcome this disadvantage of

computing only one partial derivative, the stochastic approximation (SA) method [C10] is proposed here.

In the SA method, an *n*-dimensional random vector (*n* is the number of the decision parameters), $\left[\Delta_1^{-1}, \Delta_2^{-1}, ...\Delta_n^{-1}\right]^T$ consisting of independent and symmetrically distributed entries with finite inverse moment expectations, is firstly generated using the symmetric Bernoulli (±1) distributions; and the partial gradient information of $f(x)$ for all *n*-dimensions is approximated at one computation using:

$$\nabla f(x_k) = \frac{f(x_k + c\Delta) - f(x_k - c\Delta)}{2c}\left[\Delta_1^{-1}, \Delta_2^{-1}, ..., \Delta_n^{-1}\right]^T \tag{3.6}$$

The proposed stochastic approximation method realizes computational savings of *n* times, when compared to that of the finite difference approximation in determining the gradient information by using a vector representation.

3.2.3 Validation and Applications of the Proposed Robust Search Methodology

To validate the proposed direct search methodology for robust optimizations, it is used to solve different case studies and compared with other existing robust optimal approaches. Due to space limitations, only two case studies are reported.

(1) Benchmark Test

To validate the proposed methodology, the well-designed and well-posed benchmark function [C11] is optimized to check if the proposed algorithm can correctly locate the optima of the function with high efficiency:

$$\begin{aligned} f(x) = {} & 0.7e^{-\frac{(x_1-1)^2+(x_2-1)^2}{0.18}} + 0.75e^{-\frac{(x_1-1)^2+(x_2-3)^2}{0.32}} \\ & + e^{-\frac{(x_1-3)^2+(x_2-1)^2}{2}} + 1.2e^{-\frac{(x_1-3)^2+(x_2-4)^2}{0.32}} + e^{-\frac{(x_1-5)^2+(x_2-2)^2}{0.72}} \end{aligned} \tag{3.7}$$

where x_1, x_2 are the input vectors. This benchmark function has five maximum values at points (x_1,x_2) = (1,1), (1,3), (3,1), (3,4), and (5,2). Moreover, for the maximization of this benchmark function, its global and robust solutions lie, respectively, in point (3,4) and point (3,1).

To compare performances with existing robust optimizers, this benchmark problem is solved by the proposed and the Max-Min surrogate-assisted genetic algorithms with robust solution searching schemes (GAs/RS^3) with the multiple-evaluation model (MEM) [C11]. Table 3.1 tabulates the averaged performance comparisons of the aforementioned two robust optimizers for 20 independent runs on this benchmark problem. It can be concluded that:

(1). The success rates to find the exact robust optimal solutions for both algorithms are 100%, indicating its ability to escape from local optima.

(2). The function calls for the proposed algorithm is less 20% of that of GAs/RS^3 with MEM.

Table 3.1 Performance of different algorithms on the benchmark function

Algorithm	Average number of iterations	Convergence to robust optimal
Proposed	4965	20/20
Gas/RS^3 with MEM	30960	20/20

(2) Engineering Problem Application

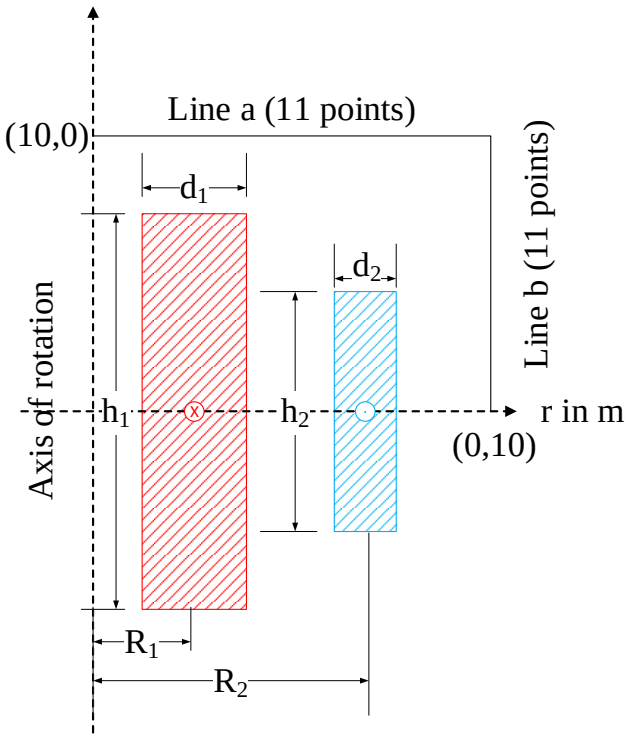

Fig. 3.1. The TEAM workshop 22 SMES configuration

The robust optimal counterpart of the TEAM Workshop problem 22 of a superconducting magnetic energy storage (SMES) configuration with three free parameters [C12-C13] is then solved, the SMES configuration is given in Figure. 3.1. The SMES system consists of two concentric coils which are the inner main solenoid and the outer shielding solenoid for reducing the stray field. The details for this case study are referred to [C12-C13]. The SMES design is to obtain a desired stored energy of 180 MJ with minimal stray fields. The reason of choosing such a problem as prototypical problem is that the TEAM workshop problems are commonly accepted problem for algorithm demonstrations.

In the three parameters problem, the inner solenoid is fixed. The dimensional parameters of the outer solenoid are optimized. Moreover, the current densities for the two coils are set to be 22.5A/mm^2. Simplifying the constraints of the problem [C12], this optimal design problem is formalized as:

$$\begin{aligned} &\min f = \frac{B_{stray}^2}{B_{norm}^2} + \frac{\left|Energy - E_{ref}\right|}{E_{ref}} \\ &s.t.\ \left|B_{\max}\right| \le 4.92T \end{aligned} \tag{3.8}$$

where *Energy* is the stored energy in the SMES device, $E_{ref} = 180\text{MJ}$, $B_{norm} = 2\times10^{-4}\text{T}$, B_{stray}^2 is a measure of the stray fields evaluated along 22 equidistant points using [C12]:

$$B_{stray}^2 = \frac{\sum_{i=1}^{22}\left(B_{stray}\right)_i^2}{22} \tag{3.9}$$

The electromagnetic field and performance parameters in equation 3.8 and equation 3.9 are computed using the 2-D finite element method (FEM). For performance comparisons, this case study is solved, respectively, by using the proposed direct QEA search methodology for robust optimizations with and without the improvements for robustness considerations formulated in equation 3.1 and 3.2, GAs/RS^3 with MEM [C11] mentioned in the previous part of this section, and the combined Polynomial Chaos and Evolutionary Algorithm (PCEA) [C12]. As explained in [C12], the combined PCEA method is proposed for efficiently solving a

robust optimization under uncertainties of some specific random process. In the numerical implementation of the combined PCEA method, a Gaussian random process is assumed for the uncertainties in the design variables. Moreover, to facilitate the numerical implementations of the polynomial chaos, the distance (radial) variable in the feasible space is used as the only uncertain variable. For a fair comparison, the final-optimized robust solution obtained by using the combined PCEA is used as a reference.

In the numerical study, the interval uncertainty is set to be $\pm 1\%$ of the limits of the intervals of the corresponding decision variables. The final solutions searched by using the proposed with and without robustness consideration, and GAs/RS^3 with MEM as well as the PCEA method are nearly identical, while the iterative numbers for the proposed with and without, GAs/RS^3 with MEM, and the PCEA method in a typical run are, respectively, 2685, 3365, 3579, and 3018. Also, the global optimal solutions searched by the proposed methodology in the same run are nearly identical to those searched so far by fellow co-researchers from IGTE [C13]. More specially, for the robust optimal solution, the stray field is 7.549×10^{-7} T, the stored energy is 179.2140 MJ; while these are, respectively, to 7.75×10^{-7} T, 179.9956 MJ for the global optimal solution which is obtained by IGTE.

Moreover, to evaluate the robustness of the global and robust optimal solutions against small variations, some post-processing numerical experiments are conducted. In a more detail description, 10 random perturbations with $\pm 1\%$ limits of the bounds of the interval uncertainty are applied to the two sets of the optimized decision variables. The numerical results revealed that the averaged performance degradations of the global optimal solution for the 10 perturbations are that the stray field changing is 0.82 and the averaged deviation of the stored energy is 0.02, both in relative values; while that the averaged performance degradations of the robust optimal solution obtained using the two robust optimizers for the 10 perturbations are that the stray field changing is 0.33, less than the given tolerance of 35%, and the averaged deviation of the stored energy is 0.0015, nearly identical to the given tolerance of 0.15%, both in relative values.

From the numerical experiments, the following could be concluded:

(1) In view of the computational efficiency, the proposed direct search methodology for robust optimizations is faster than the combined polynomial chaos and EA method since the number of the total function calls used by the former is less 90% than that by the later; and is much faster than its ancestor without the proposed improvements as well as the well-developed GAs/RS^3 with MEM;

(2) The final solutions searched by the four robust optimizers, which are the proposed direct search methodology for robust optimization with and without, the GAs/RS^3 with MEM, and the combined polynomial chaos and EA approach, are nearly the same;

(3) The objective value found by conventional algorithm is better than that found by the proposed algorithm;

(4) However, the robustness of the robust optimal solution is much stronger than that of the global optimal solution. Since the driving force of the proposed direct search methodology for robust optimizations is still the performance parameter, the objective function, it has found a global optimal solution besides the robust one in a single run.

3.3 Robust Design Optimization of Metamaterials in Wireless Power Transmission Applications

3.3.1 Introduction

As explained in previous section, metamaterial (MM) is an artificial periodic material with unique material properties that cannot be found in a naturally occurring materials when working at its resonance frequencies. MM structure often consists of unit cells that evenly repeat themselves in 3-D space. Because the footprint of the unit cell in MM structure is much smaller than the wavelength of the resonance frequency, the MM structure therefore can be regarded as a block of a homogenous, isotropic material with designed electromagnetic properties, such as a negative permeability and or permittivity, at the resonance frequency [C14]. The unit cell of a MM consists of two parts, a dielectric substrate that offers a mechanical support for the entire

macroscopic structure, and a metallic pattern deposit on the substrate, where the inductance and capacitance of the unit cell come from. Hence, the metallic pattern of the unit cell determines the resonance nature of the MM by defining the intrinsic inductance and capacitance of the unit cell and plays the most important role in the MM design and optimization [C15].

Because of the possibility of adjustments range from positive to negative effective properties, MM has shown great potential in various engineering applications; for instance, in miniaturized antenna systems and resonance coupled mid-range wireless power transmission (R-WPT) systems; and has been studied extensively in the past decade [C16-C17]. An R-WPT system utilizes the near magnetic field as the medium for energy transmissions and works based on the resonance between the receiving and transmitting coils. The resonance of the receiving and transmitting coils significantly increases the transmission range of a R-WPT system from 40 to 200 mm [C18]. The purpose of adding MMs in between the receiving and transmitting coils in R-WPT systems is to enhance the power transfer efficiency (PTE) of the systems via the resonance coupling between transmission coils and the MM slabs or blocks [C19-C20]. By tuning the resonance frequency of the MM blocks, the transmission can be enhanced, reduced, or even blocked accordingly.

The metallic pattern in the MM unit cell can be regarded as a series *RLC* circuit, and the resonance frequency of a series *RLC* circuit is inversely proportional to the product of the inductance (L) and the capacitance (C) of the circuit, and hence to have a relatively low working frequency (below 30 MHz), a large inductance and capacitance are necessary, leading to a large device footprint. On the other hand, in order to maintain the homogeneity and isotropy of the electromagnetic properties throughout the MMs, the dimensions of the metallic pattern in MM unit cell have to be strictly constrained. One way to overcome this contradiction is the series addition of on-chip circuit components, such as lumped capacitors, to increase the capacitance. However, for an *RLC* circuit having a high capacitance, its Q-factor, describing its frequency selectivity, would be relatively low. Due to these reasons, the design and optimization processes of a MM unit cell, especially the metallic structure to obtain an

appropriate *RLC* combination, are crucial for the performance and efficiency enhancements. In [C21], the effects of different *Q*-factors to the performances of MM slabs in high frequency (GHz range) applications have been analysed. However, there is a lack of a similar analysis and optimization methodology for MM structures in the low frequency applications, where both the footprint of the MM unit cell and the energy loss in the lumped element are non-negligible. Moreover, since the band of the working frequency of the MMs is relatively narrow, the robustness of the MM performance against uncertainties in both the manufacturing and operating tolerances should be carefully considered and hence the design and optimization of MM unit cell are indeed robust optimization problems. In this regard, the influence of the *L*/*C* ratios and *Q*-factor of metamaterials on the efficiency and robustness of the R-WPT systems are numerically investigated, and a new methodology to design and optimize a MM unit cell and the R-WPT system based on the surrogate-model-based robust optimization methodology is developed.

3.3.2 Formulations of the MM Optimization Problem

The MM unit cell can be regarded as a miniaturized *RLC* circuit. The circulating current conduction path, which is formed by the metallic pattern of the unit cell, creates the inductance in the circuit. Moreover, when both sides of the substrate are deposited with the metallic strips, this sandwich structure creates a capacitance in the circuit. It should be pointed out that the parasitic capacitances between layers of the spiral metallic strips are often very small as compared to the capacitance created by the sandwich structure. In other occasions where the metallic pattern is only deposited on one side of the substrate, the only capacitor available is the parasitic capacitor which is relatively small, and hence a lumped capacitance is added to the MM unit cell to reduce the resonance frequency. However, such approach will incur an additional device footprint and an energy cost. Generally, two types of MM unit cells are commonly used in electromagnetic applications, namely the split ring resonator and the spiral resonator. The spiral resonator contains a plain helix metallic pattern that is similar to that of a planer helix coil and has a larger inductance and resistance

with a compact unit cell size, which makes it more appropriate for low frequency applications. In the application proposed in this specific section, the spiral resonator is chosen as the topology for the MM unit cell. Moreover, one of the main advantages of WPT system is the removal of the transmission medium of energy transmissions and hence can be moved freely. However, if too large MM structures are added in between the coils, this advantage will be forfeited. Hence, in here, the MM unit cells repeat themselves in *x* and *y* directions and form a MM slab with only one layer of MM unit cells in the energy transmission direction of the R-WPT system.

To control the inductance and the capacitance of the MM unit cell, the number of the turns for the spiral pattern is selected as the design parameter. The equivalent inductance of the unit cell is calculated from [C21]:

$$L = \frac{\mu_0}{2\pi}\left\{4l - \left[2(N+1) - \frac{3}{N}\right](g+w)\right\}\left[\ln\left(\frac{\left\{4l - \left[2(N+1) - \frac{3}{N}\right](g+w)\right\}}{2w}\right) + \frac{1}{2}\right] \quad (3.10)$$

Where l, g, and w, are, respectively, the maximum side length, the air gap width, and the strip width of the spiral pattern; N is the number of turns of the spiral, and μ_0 is the free space permeability. Since the metallic pattern is only deposited on one side of the substrate, the only capacitance of the metallic pattern is the parasitic capacitance between the adjacent metal strips. It can be calculated from [C21]:

$$C = \frac{l}{4(g+w)}\frac{N^2}{N^2+1}\left[l(N-1) - \frac{N^2-1}{2}(g+w)\right]\varepsilon_0\varepsilon_r\frac{K\left(\sqrt{1-k^2}\right)}{K(k)} \quad (3.11)$$

where $\varepsilon_0, \varepsilon_r$ are, respectively, the permittivity of the air and the relative permittivity of the substrate; k is a constant, K is the complete elliptical integral of the first kind and is given as [C21]:

$$k = g/(2w+g).$$
$$K(x) = \int_0^{2\pi} d\theta \Big/ \sqrt{1 - x^2\sin^2\theta}. \quad (3.12)$$

Lastly, the resistance of the metallic pattern is estimated using [C21]:

$$R = \frac{\rho}{wt}l \quad (3.13)$$

In a R-WPT system, the working frequency is often relatively low, i.e., in tens of

MHz range, and hence to reach a resonance frequency as low as this value limit, a large inductance and a large capacitance are required. However, the intrinsic inductance and capacitance of the MM unit cell are not able to reach such high values, and an external lumped capacitance is thus connected to the two ends of the metallic pattern, and hence in parallel with the parasitic capacitance of the MM unit cell. The equivalent circuit model for the MM unit cell is thus given in Figure 3.2.

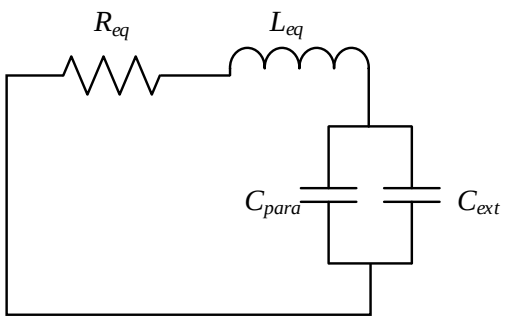

Fig. 3.2 The equivalent circuit of a MM unit cell.

It can be seen that the MM unit cell is a microscale resonance circuit and hence the resonance circuit analyzing methods can be applied to the MM unit cell as well. The *Q*-factor of an *RLC* circuit is defined as [C22]:

$$Q = \frac{\omega L}{R} = \frac{1}{\omega RC} \tag{3.14}$$

The *Q*-factor of a resonance circuit describes its selectivity performance with respect to the working frequency. A circuit of a high *Q*-factor would have only prominent circuit features, such as negative permeability in the case of the MM structure, at a frequency very close to the resonance frequency, while a circuit of a low *Q*-factor however will have a relatively large working frequency band. Conventionally, a high *Q*-factor resonance circuit is preferable, so sharp variation performances can be achieved only at the designed and targeted frequency. However, as explained previously, because there is a high probability of having manufacturing errors in the fabrication process of the miniaturized metallic pattern, the dimensions of the MM unit cell and its resonance frequency are no longer deterministic, and hence the robustness of the MM structures is also important in WPT applications. Generally, the design and optimization of MM structures in WPTs can be formulated as:

$$\begin{aligned} &\max PTE(L,C) = |S_{21}|^2 \times 100\% \\ &\text{s.t. } f = f_{working} \end{aligned} \tag{3.15}$$

where S_{21} is the transmission coefficient of the WPT system, $f_{working}$ is the working frequency. As the capacitance value is controlled by the lumped capacitor and is fixed, the main sources for the uncertainty are the inductance of the MM unit cell. Moreover, the robustness counterpart of the original optimization problem (3.15), using the weighted mean value of the objective function over a design region, is used in the present work, and formulated as:

$$\begin{aligned} &\max Mean(PTE(L,C,f)) = \frac{1}{n}\sum_{n} w_i \times PTE(L+\Delta L_i, C, f) \\ &\text{s.t. } f = f_{working} \end{aligned} \tag{3.16}$$

where w_i is the weighting factor for the ith candidate. Total n number of candidates are evenly sampled from the neighbour of a design, and the average value of all these points is used for the robustness performance calculation.

3.3.3 A Surrogate-model-based Robust Optimization Methodology

To calculate the objective values of equation (3.16), the scattering transmission coefficient, S_{21}, is evaluated using a 3-D FEM analysis. It is clear that the robustness performance calculation requires an excessive number of FEM evaluations, leading to a slow optimization speed. Response surface model, being one of the most effective surrogate models, has been widely employed in electromagnetic inverse problems. In this regard, an improved response surface model (RSM) is developed to construct the surrogate model of the system, and to replace the FEM simulation and hence increase the optimization speed.

Moreover, in the R-WPT application, the MM slab as detailed in the next chapter, generally consists of a number of unit cells (to see Figure 3.3b), is used. Our primary study has revealed that the MM unit cells structure with the same resonant frequency, but different inductance-capacitance combinations outperform the one with an

identical inductance-capacitance combination in view of performance enhancements. In this point of view, a MM slab consisting of unit cells of the same resonance frequency, but different L/C combinations is proposed. However, this will lead to a very complex design optimization process of the MM slab. To address this issue, the whole optimal procedure of the MM slab design is divided into two phases.

The objectives of the first design phase are the computation of the performance and robustness parameters of different unit cells, and the classification of the unit cell. In this stage, using the FEM simulation results of a homogeneous MM slab, where all the unit cells have identical structures and hence *LC* combinations, a third order interpolation is constructed using:

$$y_j = C_0 + \sum_{i=1}^{3} C_i x_j^i + e. \tag{3.17}$$

where y_j is the objective value of the jth sample; C_0, C_1 are two weighting coefficients in the interpolation, and *e* is an error compensation term. The robustness of each unit cell design is thus calculated using this interpolation model, y_j. According to the objective values and the robustness performances, the unit cell designs are classified into two types, namely the objective dominated design with high objective value and low robustness, and the robustness dominated design with high robustness and low objective values. Moreover, to simplify the optimal design, the unit cells of the MM slab are further divided into two groups: one centre cell and eight side cells, as depicted in Figure 3.3b.

In the second phase of the optimization process, the inductances of the centre cell and side cells are set to be different to allow a hybrid MM slabs design. Because the unit cells no longer share the same design, the interpolation model constructed in the first stage is no longer valid, and hence a multi-start RSM is proposed and employed. The proposed method has two control parameters: the inductance of the centre cell and the inductance of the side cells, and the initial design space is divided into four different sub spaces based on the objective values and robustness of the centre cell and side cell obtained at the first stage, namely the objective dominated-objective dominated, the objective dominated-robustness dominated, the robustness dominated-

objective dominated, and the robustness dominated-robustness dominated subspaces. In each sub-space, 3×3 total nine samples are simulated using 3-D FEM and the corresponding local second order RSM is constructed using:

$$y=\beta_0+\sum_{i=1}^{k}\beta_i x_i+\sum_{j=1}^{k}\sum_{i=1,i<=j}^{k}\beta_{i,j}x_i x_j+e \tag{3.18}$$

where β_0 , β_i and β_{ij} are weighting coefficients; k is the number of the total coefficients. Based on the RSM of each sub-space, the performances of all possible designs in each subspace are then evaluated and the global optimal solution can be eventually identified using an exhaustive method. Since the RSM significantly reduces the computational time, an exhaustive exploration of the entire design space in details will not incur too heavy computation cost to the optimization problem and hence is feasible in the proposed methodology.

3.3.4 Numerical Results and Experimental Validations of the Proposed Methodology in MM Design Optimization

The MM unit cell used in the numerical application is made by a piece of substrate and a piece of metal strip deposited on one side of the substrate. The substrate, which is made from FR-4, has a constant thickness of 4 mm, a constant side width of 37.2 mm, and a dielectric constant of 4.4. The reason of choosing such a material is because it is the most common material in the PCB fabrication process with the lowest cost. Because the substrate only serves as a physical support for the MM structure, any plastic material that does not exhibit electromagnetic intervention could be used. The metallic pattern is made by copper strips of 0.0035 mm thickness, a common standard for PCB fabrication, deposited on one side of the substrate, and a width, *w*, of 0.5 mm and a spacing between adjacent strip, *g*, of 0.5 mm. The largest round of the metallic pattern has a side width of 36.2 mm, 1 mm smaller than that of the substrate, and the number of turns of the spiral varies from 2 to 15 and are set to be integer values to reduce the design space. The overall MM slab consists of $3\times3=9$ unit cells. The MM structure with all the annotations is depicted in details in Figure 3.3.

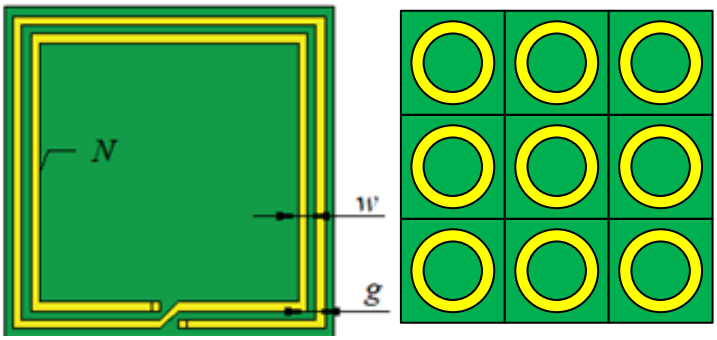

(a) (b)

Fig. 3.3. (a) MM unit cell and (b) the MM slab structure

Table 3.2 The physical parameters of the metamaterial structure

Parameter	Value
Slab width	37.2 mm
Metal width	0.5 mm
Metal thickness	0.0035mm
Metal spacing	0.5 mm
Largest metal length	36.2 mm

The MM slabs are placed right at the middle of a conventional four-coil R-WPT systems. In the four-coil system, a transmission coil and a receiving coil are added in between the source and the load coils to focus the magnetic field and hence increase the transmission distance [C24]. The source and load coils are copper rings with a diameter of 60 mm, and placed 200 mm apart, and the transmission and receiving coils are identical copper helix coils with a diameter of 120 mm, an axial length of 30 mm and a cross-sectional area of 1 mm^2, placed 140 mm apart. A 50 Ω load is used for load matching and hence the maximum PTE. Figure 3.4 depicts the schematic diagram of the studied 13.56 MHz four coil WPT system and the MM slabs with 9-unit cell of metamaterials for PTE enhancements.

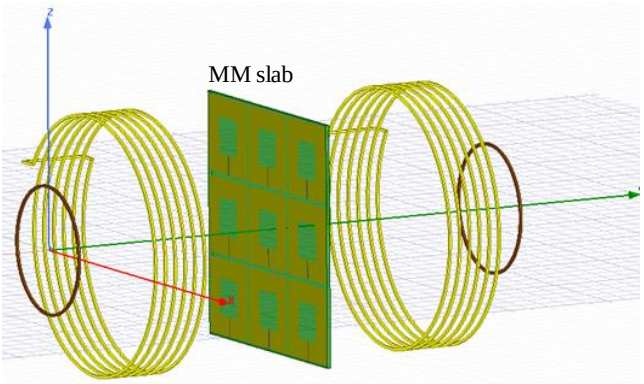

Fig. 3.4. Four coil WPT system with a metamaterial slab in the numerical application

The proposed optimal design methodology is applied to find the optimal inductance-capacitance combinations of the 9-unit cells of the MM slab to obtain the best performance and robustness of the prototype R-WPT system. In the first phase of the optimization process, to model the uncertainty, the upper and lower limits of the inductance for each unit cell are set to be 10% of its nominal value, and their robustness values are evaluated using the aforementioned average method. The RSM is generated using 14 potential designs, and the numerical results of typical runs indicate that the error between the predicted results of the proposed RSM and the computed PTEs of the WPT system using FEM is less than 3%. Under such implementation conditions, the PTE, and the corresponding robust performance of the proposed prototype WPT system with the identical turn unit cell MM slabs are computed and tabulated in Table 3.2. The CPU time used by the proposed RSM to compute once robust performance of a design is 10 seconds while that for a FEM is 30-40 minutes, and hence a huge amount of computation resource can be saved via using the proposed RSM assisted simulation method. From the numerical results of Table 3.2, the unit cells with turn numbers of 2-8 are classified into objective-dominated designs, while those with turn numbers of 9-15 are grouped as robustness-dominated designs, and four RSMs are constructed. The optimization procedure continues to phase two.

Table 3.3 PTE and its degradation under different turn unit cell MM slabs

Number of turns	Inductance (H)	PTE (out of 1)	PTE(robust)	Performance degradation (%)
2	0.000143589	0.247742206	0.205285481	17.13746119
3	0.000140607	0.241794507	0.198114255	18.06503095
4	0.000137931	0.170512353	0.18572433	-8.921333975
5	0.000135381	0.145181665	0.170976641	-17.76737808
6	0.000132897	0.130704472	0.155421737	-18.91080289
7	0.000130452	0.127094254	0.140047108	-10.19153369
8	0.000128036	0.124926212	0.12921911	-3.436347462
9	0.000125639	0.122928538	0.1243486	-1.15519327
10	0.000123259	0.120821324	0.121739	-0.75953099
11	0.000120892	0.118708268	0.120177852	-1.237979686
12	0.000118538	0.11815806	0.118858428	-0.592738474
13	0.000116194	0.117339153	0.117653319	-0.267742259
14	0.000113859	0.116723016	0.116563745	0.136451741
15	0.000111535	0.115917788	0.11560561	0.269309749

In the second stage of the optimization process, a multi-start RSM is constructed and employed; and an exhaustive method is used to find the global optimal solution in the whole design space. More specially, it is found that when the side cells have two turns and the centre cell has six turns, the PTE of the system reaches a maximum value of over 25%, while the robustness of this solution remains strong, i.e., the PTE degradation is relatively low (<10%). Obviously, a significant higher quality design is obtained in terms of both performance and robustness parameters, which are not achievable by a homogeneous slab. Compare with the case where these is no MM slab presented in the WPT system, the PTE of the system increases significantly from 3.16% to over 25%, indicating the necessity of the addition of MM slabs in the WPT systems.

3.4 Summary

To efficiently find the robust optimal solutions of an electromagnetic device design problem under interval uncertainties in a topology optimization, a direct search methodology is proposed in this chapter. The numerical results on two case studies have demonstrated that the proposed direct search methodology can use relatively few iterations to find the same quality final solutions compared to an efficient combined polynomial chaos and EA method and its ancestor as well as the GAs/RS^3 with MEM. Also, a promising byproduct of the proposed robust search methodology is that it can find the global optimal solution of a design problem under interval uncertainties in a single run.

Moreover, this chapter strives to explain the influence of different LC ratios and *Q*-factors of a MM unit cell on the performance, especially the robustness of the PTE, of a MM assisted low frequency R-WPT system; and proposes a two-phase methodology to optimize the R-WPT application-oriented MM slab based on RSM surrogate model. The numerical results of a 13.56 MHz four-coil WPT system indicate that:

1) The *LC* combinations do play a crucial role in affecting the robustness of the overall WPT system. Although the working frequencies are the same, different *LC* combinations can offer different working bandwidth, and hence different ability to withstand uncertainties and errors in the devices, thus changing the *LC* ratio is a good way for designing and optimizing the MM structure.

2) The proposed methodology is able to search for the robust solutions within a short period of time and a relatively low number of FEM simulations. The results show that by optimizing the hybrid MM slabs, where the unit cell structures are not identical, in WPT system, the system power transfer efficiency and its robustness can be significantly enhanced.

3.5 References-Part C

[C1] Jan K. Sykulski, “State of the art and new challenges in design optimisation of electromagnetic devices,” *Lecture of ICEF2016*, September 18-20, 2016.

[C2] G. L. Soares, R. L. S. Adriano, C. A. Maia, L. Jaulin, and J. A. Vascon-celos, "Robust multi-objective TEAM 22 problem: a case study for un-certainties in design optimization," *IEEE Trans. Magn.*, vol. 45, pp. 1028-1031, 2009.

[C3] Nam-Kyung Kim, Dong-Hun Kim, Dong-Wook Kim, Heung-Geun Kim, Lowther D.A., Sykulski J.K.; "Robust optimization utilizing the second-order design sensitivity information," *IEEE Trans. Magn*., vol. 46, pp. 3117 - 3120, 2010.

[C4] Jianhua Zhou, Shuo Cheng, and Mian Li, "Sequential quadratic programming for robust optimization with interval uncertainty," *J. Mech. Des.*, vol. 134, 100913-5, doi:10.1115/1.4007392, 2012.

[C5] Ho S.L., Shiyou Yang, Guangzheng Ni, Cheng K.W.E, "An efficient tabu search algorithm for robust solutions of electromagnetic design problems," *IEEE Trans. Magn*., vol. 44, pp.1042 – 1045,2008.

[C6] S. L. Ho, Shiyou Yang, Peihong Ni , and Jin Huang, “A Quantum-inspired evolutionary algorithm for multi-objective design,” *IEEE Trans. Magn.*, vol. 49, pp. 1069-1612, 2013.

[C7] Han, K. H., and Kim, J. H., "Quantum-inspired evolutionary algorithm for a class of combinatorial optimization," *IEEE Trans. Evol. Comput.*, vol. 6, No. 6, Dec. 2002, pp. 580-593.

[C8] Platel, M. D., Schliebs, S., and Kasabov, N., "Quantum-inspired evolutionary algorithm: a multimodel EDA," *IEEE Trans. Evol. Comput*., vol. 13, No. 6, Dec. 2009, pp. 1218-1232.

[C9] H. Talbi , A. Draa, and M. Batouche, "A new quantum-inspired genetic algorithm for solving the traveling salesman problem", *Proc. IEEE Int. Conf. Ind. Technol.*, pp.1192-1197 , Dec. 2004.

[C10]Lianlin Li, Behnam Jafarpour, M. Reza Mohammad-Khaninezhad, "A simultaneous perturbation stochastic approximation algorithm for coupled well placement and control optimization under geologic uncertainty," *Comput Geosci*, vol. 17, pp. 167–188, 2013.

[C11]Y. S. Ong, P. B. Nair, and K. Y. Lum, “Max-Min surrogate-assisted evolutionary algorithm for robust design," *IEEE Transactions on Evolutionary Computation*, vol. 10, pp. 392-404, 2006.

[C12]S. L. Ho, and S. Yang," A fast robust optimization methodology based on polynomial chaos and evolutionary algorithm for inverse problems," *IEEE Trans. Magn.*, vol. 48, pp. 259-262, 2012.

[C13]http://www.compumag.org/jsite/images/stories/TEAM/problem22.pdf.umerical Results

[C14]B. Wang, W. Yerazunis, and K. H. Teo, Wireless Power Transfer Based on Metamaterials, *Wireless Power Transfer Algorithms, Technologies and Applications in Ad Hoc Communication Networks*, pp. 31-53, 2016.

[C15]H. Guan, L. Liu, S. Yang, and X. Chen, Efficiency enhancement of wireless power transfer system by using resonant coil and negative permeability metamaterial, *International Journal of Applied Electromagnetics and Mechanics*, pp. 1-9. 2018.

[C16]E. J. Rothwell and R. O. Ouedraogo, Antenna miniaturization: definitions, concepts, and a review with emphasis on metamaterials, *Journal of Electromagnetic Waves and Applications*, vol. 28, pp. 2089-2123, 2014.

[C17]B. Wang, W. Yerazunis, and K. H. Teo, Wireless power transfer: metamaterials and array of coupled resonators, *Proceedings of the IEEE*, vol. 101, pp. 1359-1368, 2014.

[C18]Z. Zhen and P. Hongliang, Wireless power transfer -an overview, *IEEE Transactions on Industrial Electronics*, vol. 66, pp. 1044-1058, 2019.

[C19]K. Sun, R. Fan, X. Zhang, Z. Zhang, Z. Shi, and N. Wang, An overview of metamaterials and their achievements in wireless power transfer, *Journal of Materials Chem.* C, vol. 6, pp.2925-2943, 2018.

[C20]T. S. Pham, A. K. Ranaweera, V. D. Lam, and J.-W. Lee, Experiments on localized wireless power transmission using a magneto-inductive wave two-dimensional metamaterial cavity, *Applied Physics Express*, vol. 9, Art No. 044101, 2016.

[C21]F. Bilotti, A. Toscano, L. Vegni, K. Aydin, K. B. Alici, and E. Ozbay, Equivalent-circuit models for the design of metamaterials based on artificial magnetic inclusions, *IEEE Transactions on Microwave Theory and Techniques*, vol. 55, pp.2865-2873, 2007.

[C22]T. Oh and B. Lee, Analysis of wireless power transfer using metamaterial slabs made of ring resonators at 13.56MHz, *Journal of electromagnetic engineering and science*, vol. 13, pp.259-262, 2013.

[C23]S. L. Ho, and S. Yang, A fast robust optimization methodology based on polynomial chaos and evolutionary algorithm for inverse problems, *IEEE Trans. Magn.*, vol. 48, pp.259-262, 2012.

[C24]Y. Zhang, S.L. Ho, and W. Fu, A dynamic multi-level optimal design method with embedded finite-element modelling for power transformers, *AIP Advances*, vol. 8, Art No. 056610, 2018.

Chapter 4 Numerical Methods and Algorithms for Wireless Power Transmission and Multi-Objective Topology Optimization

Surrogate model is a numerical technique to represent complex 3-D models with relatively simple mathematical functions or models and has been widely applied in the design and optimization of 3-D engineering problems, as explained in the aforementioned section. Hence it is believed that by employing surrogate model in the design and topology optimization of electromagnetic device, a great amount of computational resource can be saved. Based on the existing studies, a surrogate model-based optimization algorithm is proposed and applied to the design and optimization of MMs in WPT applications and hands-on experiments are conducted to validate the efficiency and correctness of the proposed algorithm. Moreover, in certain actual applications of topology optimizations, the multi-objective functions cannot be independently optimized, and hence in this chapter a vector wind driven optimization algorithm is also developed to solve the multi-objective topology optimization.

4.1 A DOE Assisted Surrogate Model for an Improved TABU Search Based Refinement Optimal Method in MM Slab optimizations

4.1.1 Metamaterial Slabs in Wireless Power Transmission Applications

As explained previously, wireless power transmission (WPT) has experienced a tremendous progress in the past two decades. Generally, for the applications with wireless transmission distances up to 40-200 mm [D1], the resonance coupling technique has surpassed the conventional inductive coupling one due to a relatively

higher transmission efficiency in the former. The resonance WPT (R-WPT) technique is developed based on the resonant coupling between two coils, the transmitter, and the receiver, that have an identical resonance frequency in the system [D2]. Nevertheless, the power transfer efficiency (PTE) of a R-WPT system is still lower than that of a wired power transfer system. To increase both the power transfer efficiency and the transmission distance of a R-WPT system, metamaterial (MM) slabs are inserted between the transmitter and receiver, something like relay coils serving as an intermediate station for power transmission [D3-D4]. However, the proposed metamaterial slab, when compared to a relay coil, is much smaller in the device footprint, and hence is more appropriate in applications that have space constraints [D5]. Moreover, the performance enhancement by using an optimized metamaterial slab is generally stronger than that by using a relay coil. In a R-WPT application, a left-handed MM with both negative permeability and negative permittivity is often used to manipulate the propagating electromagnetic waves and fields to increase the PTE of the system [D6]. However, in the frequency band of a R-WPT system, the dimension of the system or device is extremely small compared to the wavelength of the dominating working frequency. The corresponding electromagnetic field can thus be viewed as quasi-static fields [D7], and the electric and magnetic fields are virtually decoupled. One can thus manipulate this near-magnetic field using a single negative permeability metamaterial [D2].

A metamaterial usually consists of a large number of microscale units or unit cells. Originally, all unit cells of a MM slab in WPT applications are set to be identical to form a periodic structure and a resultant uniform physical property, and hence the MM structure is often regarded as a homogeneous material in macroscale. However, it is proved that a small distortion will not affect the overall property of a periodic structure material, such as an MM structure [D8], and hence a cavity can be created at the centre of the MM slabs to confine the transmitting electromagnetic wave and field; and the PTE of the WPT system can be further enhanced [D9]. This type of MM slabs is termed as a hybrid MM (HMM) and the effectiveness of HMM slabs in WPT applications has

recently been validated [D10-D13]. To understand the working principle of the HMMs slabs, the rationale of MM slab is first explained.

Considering the case when a magnetic field passes through the boundary of two materials with different relative permeability, the normal component of the magnetic flux density B will be continuous:

$$B_1^{\perp} = B_2^{\perp} \tag{4.1}$$

where subscripts 1 and 2 stand for two types of materials at the boundary of refraction. On the other hand, consider a small incremental loop at the boundary of the two materials, by applying Ampere's Circuital Law, the tangential component of the magnetic field H follows:

$$H_1^{\parallel} - H_2^{\parallel} = \sum I_{\text{surface}} \tag{4.2}$$

If there is no surface current at the boundary, i.e., $I_{\text{surface}} = 0$, equation 4.2 becomes:

$$\frac{B_1^{\parallel}}{\mu_1} - \frac{B_2^{\parallel}}{\mu_2} = 0 \tag{4.3}$$

In the above equation, μ_1 and μ_2 are the relative permeability of the two materials. Combining equations 4.1 and 4.3, the magnetic boundary condition at the interface of the two materials with different permeability can be described as:

$$\frac{\tan\theta_1}{\tan\theta_2} = \frac{\mu_1}{\mu_2} \tag{4.4}$$

where, θ_1 and θ_2 are the refractive angles at the two sides of refraction, respectively.

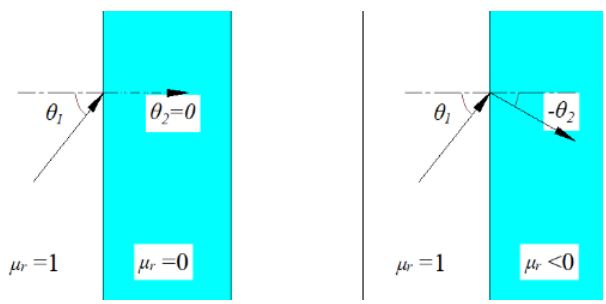

Fig. 4.1. Refractive principle of MM with zero and MM with negative μ_r.

As illustrated in Figure 4.1, negative permeability materials can be used to guide the propagation of waves and fields and focus the near field of a R-WPT system to increase the system PTE, which is represented by the solid arrow in Figure 4.1. Consequently, the design of MM has been merged with other types of periodic structures, such as photonic crystals, to form an HMM structure, in order to investigate the possibility for further electromagnetic performance enhancement [D10-D13]. The working principle of the cavity based HMM is an analogy to the bandgap structure in the photonic crystal [D14]. Due to the periodic nature in metamaterials, small defects will not affect the overall property of the structure [D8]. Thus, the cavity mode is created by inserting abnormal unit cells into the periodic structure, thereby creating a tunnel for a specific frequency near field to travel through. Moreover, because the unit cells near the cavity all work in the hybridization bandgap, the cavity can confine the near-field and hence enhance the PTE [D10]. A typical study has revealed that a more than 5% increment of PTE is obtained at a transmission distance of over 150 mm using a 6.8 MHz resonance frequency HMM slab [D11]. However, in the design of the HMM slabs for WPT applications, to evaluate the PTE of the system and investigate the spatial field distribution, a full time-domain 3-D finite-element method (FEM) simulation procedure is necessary. However, this is a typical large-scale problem with very fine mesh resolution, and consequently, the FEM simulations of the whole system often involve millions of mesh elements, and the computational cost for one simulation may take several hours. The ensuing high computational cost, which renders the design methodology inappropriate for optimizing HMM slabs in R-WPT system, is the main shortcoming of the existing field analysis approaches and stochastic population-based optimal algorithms. In most of the existing studies, the trial and error approach or a tuneable device such as a capacitor is commonly used to find the potential HMM designs [10-13]. Obviously, a major problem of such design methodology is that only a very limited portion of the design space can be explored, and hence there is no guarantee that the methodology can converge to the global optimal solution, and the design of the HMM slabs is heavily dependent on the experience of the designer. To overcome these deficiencies of the existing designing methodology and to fully

automate the design process, a design-of-experiment (DOE) assisted sequential refinement method for design optimizations of HMM slabs in R-WPT applications is developed, examined, and validated via both numerical simulations and experimental studies in this chapter. The proposed search methodology can refine the searches in the promising subspaces; and have a coarse search, or even discard the exploitations in the worst subspaces. Hence, the proposed optimization methodology requires a smaller number of samples to effectively predict a full EM simulation results when compared to a conventional surrogate model, significantly reducing the computational cost of the design optimization process. As a result, a more detailed exploration of the effects of different possible HMM designs in the WPT energy transfer efficiency can be conducted. To validate the proposed optimization methodology, it is applied to optimize the HMM slabs in a conventional four-coil R-WPT system, and the numerical comparisons between the proposed methodology, other types of surrogate models and full EM simulations have revealed that the proposed methodology is able to accelerate the solution speed without any compromise on the solution quality. Both the numerical and the experimental results of an HMM based WPT systems show that the HMM slabs designed by using the proposed methodology outperforms its homogenous counterpart with a PTE enhancement up to 12 %.

4.1.2 A DOE Assisted Surrogate Model and Improved TABU Search Based Refinement Optimal Method

In the HMM designs, the unit cells for cavity on the slabs and their surrounding unit cells are set to have different resonance frequencies [D12]. Once all the physical parameters for the WPT system are determined, the optimization goal thus becomes finding the best combinations of resonance frequencies of all unit cells in the HMM slabs, in order to obtain the highest PTE of the WPT system. This can be achieved by changing the physical designs of each unit cell, such as the sizes and dimensions, its metallic pattern, and the capacitances of the on-chip capacitors. In the optimization process, the inductances of every unit cell are fixed, so that the mutual inductances between the HMM slabs and the transmitting (Tx) or receiving (Rx) coils are fixed,

and hence the resonance frequency of the WPT system will not be distorted when the HMM design changes as the optimization processes progress, and the performance of the WPT system itself maintains at its best at its working frequency. To tune the resonance frequency and hence the permeability of all the unit cells in HMM slabs, the capacitances of the on-chip capacitors are selected as the main control parameters, and the distances between different unit cells are chosen as the secondary decision variables to adapt different geometry scale of the WPT system. Since the microscopic scale resolution of the MM unit cell is extremely high as compared to the physical dimensions of the R-WPT system, a full FEM simulation of the whole system involves millions of mesh elements. For instance, for an MM slab with 0.0035 mm thickness metal structure, the total mesh for the WPT system is more than one million elements using a relatively fine mesh, and more than 30 minutes are needed for the meshing using a 32GB memory computer. Hence, the optimization of the HMM slab is extremely time consuming. In this regard, a DOE assisted surrogate model based on Kriging method with an adaptive searching refinement methodology is proposed to deal with this specific type of problems in this chapter. The proposed method is able to handle the optimization of complicated 3-D problems without any requirement for prior information efficiently, and hence is able to search for the optimal design of the HMM assisted WPT system.

Kriging method is one of the most practiced surrogate models developed as a category in the response surface method and enjoys the merit of more accurate [D16]. It can be formulated as [D17]:

$$\hat{f}(x) = w_0 + \sum_{i=1}^{N} w_i \exp\left[-c^2 \left\| x - x_i \right\|^2\right] \tag{4.5}$$

where $\hat{f}(x)$ is the predicted value of $f(x)$ at observing or sampling point x, $w_i (i = 1, 2, 3, ..., N)$ is a weighting factor for the ith observing point, c is a correlation parameter, and N is the number of sampling points. The accuracy of the reconstructed function $\hat{f}(x)$ depends highly on the values of the weighting factors and the correlation, as well as the way that the observing points to be sampled. To ensure a

relatively full exploration of the entire design space with relatively small sampling points, a Latin-Hypercube sampling-based design-of-experiment (DOE) method is employed to determine the positions of the observing points. In the DOE method, the number of samples required to reconstruct the response is related to the number of design parameters [D19]:

$$N = c \cdot p^{s} \tag{4.6}$$

where p is the number of the portions that each design parameter is divided into; c is an adjusting coefficient in the iteration process, and s is the number of the design parameters in the optimization problem.

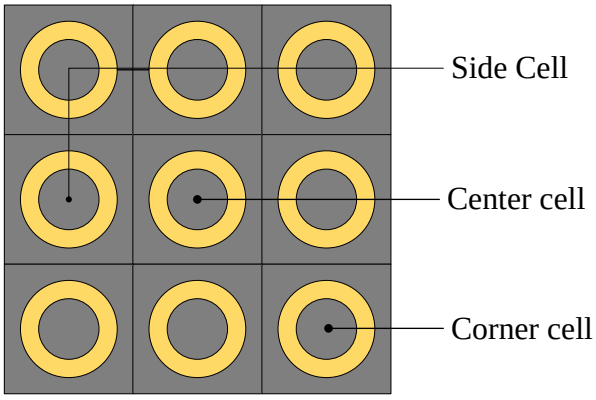

Fig. 4.2. Identification of the classification of different types of unit cells.

In this study, a 3×3 unit cell HMM slab is used just as a prototype of the optimization study, and the proposed methodology, just as other optimal algorithms, can be extended to HMM slabs with arbitrary numbers of the unit cells without any limitation on the number of decision parameters. To maintain the symmetrical geometry of the HMM slabs, the unit cells are classified into three different groups, namely the centre cell, the corner cells, and the side cells (Figure 4.2). The centre cell has a fixed on-chip capacitance and a fixed resonance frequency which is equal to the working frequency to ensure a maximum near-field transmission at the middle of the HMM slabs. The two main control parameters, the capacitances of four side cells and four corner cells, together with the secondary variables, the distance between different cells, will be optimized to form a cavity at the centre of the slab.

As explained in the early part of this section, the DOE assisted surrogate models have been widely applied to solve complex 3-D EM problems [D18-D22]. To reduce the number of sampling points required in a DOE, the proposed methodology introduces a multi-start refinement strategy. For example, for the convenience of intuitive explanations, the two-capacitor design is taken as an example, and the initial design space in this case study for the two capacitors is a two-dimensional (2-D) space formed by the two control parameters, the capacitances of the on-chip capacitors of the side cell and the corner cell and the associated resonance frequencies, are depicted in Figure 4.3. The proposed multi-start strategy divides this design space into four subspaces based on the values of the relative permeability of the corner cells and the side cells at the selected working frequency. The design domain is hence divided into four quadrants. Based on their corresponding relative permeability, the four quadrants are named as the positive-positive, the positive-negative, the negative-positive, and lastly the negative-negative quadrants, as illustrated in Figure 4.3. For each possible design in the design domain, the capacitance values of its corner cells and side cells will determine the resonance frequencies of these two types of cells, and hence the subdomain the design will fall into. By dividing the design domain into sub-domain, it is possible to apply multi-start algorithm that can parallelly evaluate, interpolate, and construct the surrogate models required for the optimization process.

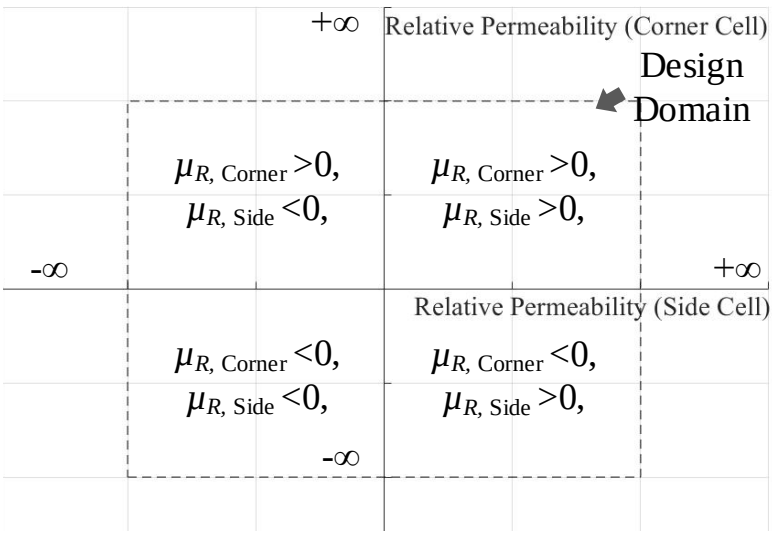

Fig. 4.3. Design domain and four subdomains of the two capacitors.

In each sub space at the kth iteration, the Latin-Hypercube Sampling (LHS) method is used to generate N_i^k sampling points for the Kriging method to construct the local surrogate model of the R-WPT system based on the 3-D FEM evaluations. The initially starting point in each subspace for the first iterative cycle is selected randomly. In the kth iteration, the starting points of the decision parameters in each subspace are selected to be equivalent to the optimal solutions of the last iteration in that subspace, and the neighbourhood of the starting points is sampled using the LHS method to generate certain number of new sampling points, and the objective values of these new sampling points will be evaluated using three-dimensional (3-D) FEM. Lastly, the Kriging surrogate model is constructed using all available sampling points from the 1st iteration cycle to the kth iteration cycle, and an improved tabu search method is implemented in each subspace to find the global optimum of the kth iteration and will be iteratively used as the starting point of the next iteration. Compared with the existing refinement searching procedures, the salient feature of the proposed one is its bi-directional characteristics. More specially, the proposed refinement searching methodology refines the searches in the promising sub spaces by intensifying sampling points and gradually pinpoints the exact global optimal solution by using some adaptive upper and lower limits of the decision parameters; coarse searches are used or exploitations are even discarded in the worst sub spaces. The upper and lower bounds of any decision parameter, h, of two consecutive iterations, k and $k+1$, decreases exponentially using the predefined adaptive parameters α_1 as:

$$h_{kriging}^{k+1} = h_{kriging}^{k} \times \alpha_1, 0 < \alpha_1 < 1 \qquad (4.7a)$$

Similarly, the reduction of the number of sample points in the subspace with relatively lower rank, $N_{\text{worst objective}}$, of two consecutive iterations, k and $k+1$, is updated using a predefined shrinking ratio, α_2, using the following round function:

$$N_{\text{worst objective}}^{k+1} = \text{round}(N_{\text{worst objective}}^{k} \times \alpha_2) \qquad (4.7b)$$

Once the local surrogate model for each sub space is constructed, any optimal algorithm can be used readily to solve the corresponding optimization problem.

However, an improved tabu search method is introduced and used due to its simplicity and fast convergence speed. The major improvement in the proposed tabu search algorithm when compared to the existing one in [D15] is the generating mechanism for the neighbourhood solutions. The search space for the improved tabu search method in each iteration cycle is the same as the sampling space for the surrogate model, rather than the whole one; and the step size for each parameter in the tabu search is $\frac{1}{100}^{\text{th}}$ of the search space, so that the entire space will be extensively explored. The reason that one selects the step size of $\frac{1}{100}^{\text{th}}$ of the search space is that the change in the capacitance values will not significantly affect the objective value if the step size is smaller than this limit, other thing being equal. It is noted that too small a step size will lead to wastage in the computational resources. Because the computation of the objective function values using a Kriging model is much faster than that using an FEM simulation, the tabu search process for each iteration cycle can be completed within a very short time. Moreover, in the proposed improved tabu search method, the so far searched best solution in each sub region of the feasible space is recorded and used to guide the generation of new neighbourhood solutions. A weighted aggregation of the best objective functions from all subspaces is used to guide the search of the tabu method, and the updating of both step size and the searching position are given by:

$$\begin{aligned} h_{tabu}^{k+1} &= h_{kriging}^{k+1} \times 0.01 \\ x_i^{n+1} &= x_i^n + r\Delta x_i^{n+1} + (1-r)\sum_{j=1}^{M} w_j x_j^{best} \end{aligned} \tag{4.8}$$

where n is the number of iterations in the tabu process, j is the jth subspace, r is a random parameter which is uniformly distributed in $[0,1]$. To consider the closeness of an optimal point, for example x_j^{best}, in different subspaces, the weighed parameter w_j is inversely proportional to the distance of the point, x_i^n, in relation to x_j^{best}.

After the optimization of each subspace in each cycle using the improved tabu search method, the subspaces will then be sorted based on the performance parameter

values, and the numbers of sample points of the sub spaces with the best and worst performances in that iteration will be automatically intensified and reduced, respectively, in the next iteration.

This iterative procedure of the proposed optimization methodology will continue until the differences or errors in the searched best objective function values for each subspace in the two consecutive iterative cycles are smaller than a predefined tolerance. To facilitate the implementation of the proposed optimization methodology, its flow diagram is given in Figure 4.4.

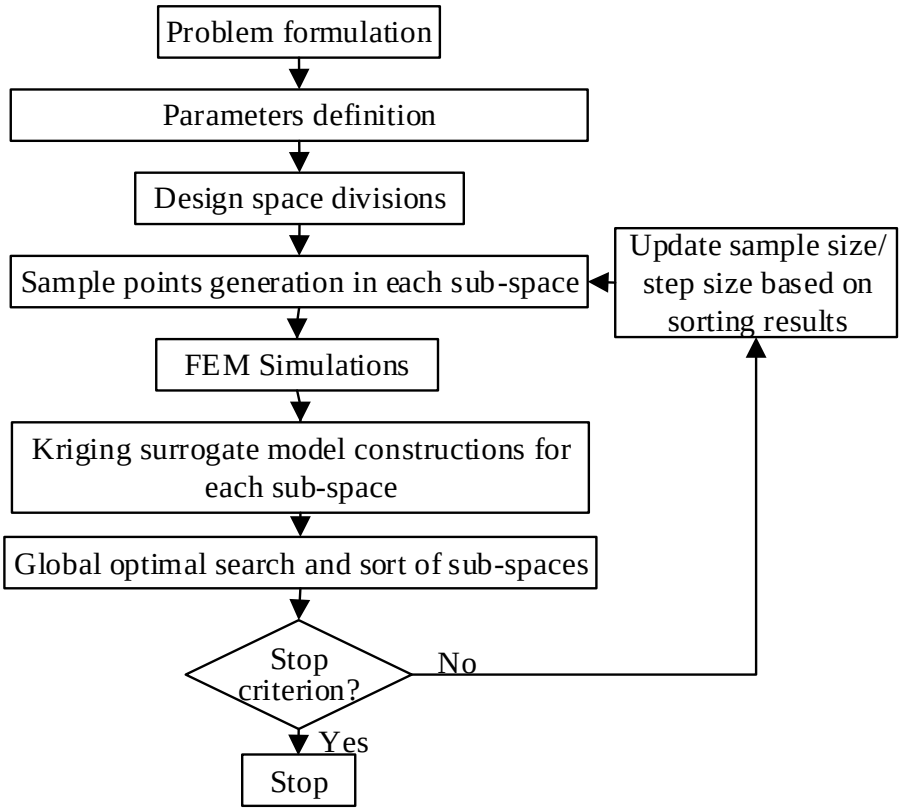

Fig. 4.4. Flow chart of the proposed methodology.

4.1.3 Numerical Results and Experimental Validation of the Proposed Method in HMM Design

(1) Numerical Experiments

The proposed methodology is applied to optimize the HMM slabs of a four-coil 13.88 MHz R-WPT system. 13.88 MHz is chosen as the working frequency because in the experimental setup it is found that 13.88 MHz is the frequency that is only

obtainable (the closest one to 13.56 MHz, one of the frequency centre in ISM band) by using integer incremental values of capacitances. However, to facilitate a fair comparison between the simulated results and the experimental ones, the working frequency is slightly varied. Moreover, instead of the topology of the unit cell, the design parameters of the unit cell are optimized to make the optimization more efficient and less time consuming. The arrangement of the prototype is shown in Fig. 4.5. The distance between Tx and Rx coils is 150 mm, and the two coils are identical copper coils with a 60 mm radius and a 30 mm spiral length. The copper coils are set as 1 mm width square helix for a faster simulation. One 23.2 pF capacitor is connected to the ends of the Tx/Rx coils to tune the resonance frequency of the coils to 13.88 MHz, and an HMM slab is placed right at the centre of the system. In the unit cell of the HMM slab, a 15-turn copper coil with 0.0035 mm thickness (0.0035 mm is one of the standard thickness in PCB printing technology), 0.5 mm width and 0.5 mm spacing is deposited on one side of the surface of the 1.6 mm thick, 37.2 mm wide FR-4 substrate, and an on-chip capacitor is connected at the ends of the metallic pattern for resonance frequency calibration. Table 4.1 summarizes all circuit parameters used in the numerical experiments and the actual experimental studies. In the experimental study, it is hard to keep the copper wire loosely as that is done in the simulation cases, and hence the copper wire is tightly wounded on the plastic tubes. Consequently, the inductances of the coils in the experimental study are much higher than those of the numerical simulation computations. Nevertheless, the resonance frequency, as well as the distance between the source and load coils, are kept as the same for both cases to ensure a fair comparison.

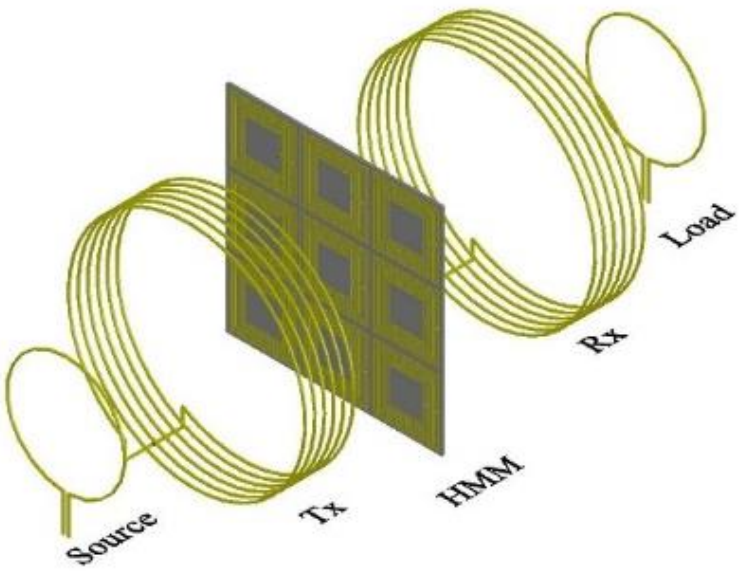

Fig. 4.5. The prototype R-WPT system under optimization.

Table 4.1 Circuit parameters of two experiments

	Numerical	Actual
Inductance (MM)	9.9 μH	NIL
Inductance (Source)	81 nH	160 nH
Inductance (Tx/Rx)	5.9 μH	23.3 μH
Capacitance (Tx/Rx)	23.2 pF	6 pF

The goal of the design optimization is to maximize the PTE, measured using the transmitting coefficient S_{21} [D12] between the two ports defined at the source and the load coils with an impedance of 50 Ω, of the system, from:

$$\begin{aligned} &\max PTE(x_i) = |S_{21}|^2 \\ &s.t. \quad x_i \subseteq [x_i^{\min}, x_i^{\max}], (i = 1 \text{ or } 2) \end{aligned} \tag{4.9}$$

The 3-D FEM simulation is used to compute the system performance at the sampling points and one simulation costs about one hour for more than 1 million mesh elements on a desktop with Intel® i5-6600 3.30GHz CPU and 32GB DDR4 RAM, and the mesh size is 0.0035 mm at the surface of the HMM slab, and gradually increases

to 1 mm for the rest of the 3-D model. To determine the range of the on-chip capacitance, unit cell FEM simulations are conducted to examine its permeability with different capacitance values at the working frequency using an effective homogeneous medium method [D5]. It is observed that when the capacitance value is not within the range of 12 pF to 16 pF, the permeability of the unit cell remains constant, and variations will no longer influence the system PTE. Hence, the two main or primary design parameters, the on-chip capacitances of the corner and side unit cells, are set in the range of 12 pF to 16 pF for sampling, in order to reduce the design space. The starting points of four sub spaces of the capacitances are hence located at: 13 pF-13 pF, 13 pF-15 pF, 15 pF-13 pF and 15 pF-15 pF, and the initial number of samples of LHS is 16 , with an initial step size of 1 pF and adaptive parameters, α_1 and α_2, in (4.7), of 0.5 and 0.6, respectively, selected by using a trial and error approach. In the iterative process of the proposed methodology, from the second iterations onward, only three sub-spaces for the capacitors are active, and one subspace (the 15 pF-15 pF subspace) is discarded due to its extremely poor performances of all candidates in that specific subspace. Moreover, the additional sampling points for the worst subspace eventually become only 12% of all additional sampling points of all subspace when the optimization procedure terminates at the fifth iteration. By using the aforementioned method, the computational resource required to accurate sample and reconstruct the entire design domain can be significantly reduced.

Table 4.2 Comparison of different surrogate models

	Optimal solution (Capacitances)	PTE (and relative error)	No. of FEM runs
Proposed	(11.1pF,14.9pF)	15.4% (4%)	188
SKE	(14.3pF,9.9pF)	3.2% (80%)	188
LI	(11.0pF,11.0pF)	5.6% (65%)	220
Full FEM	(11.1pF,14.9pF)	16% (0%)	400

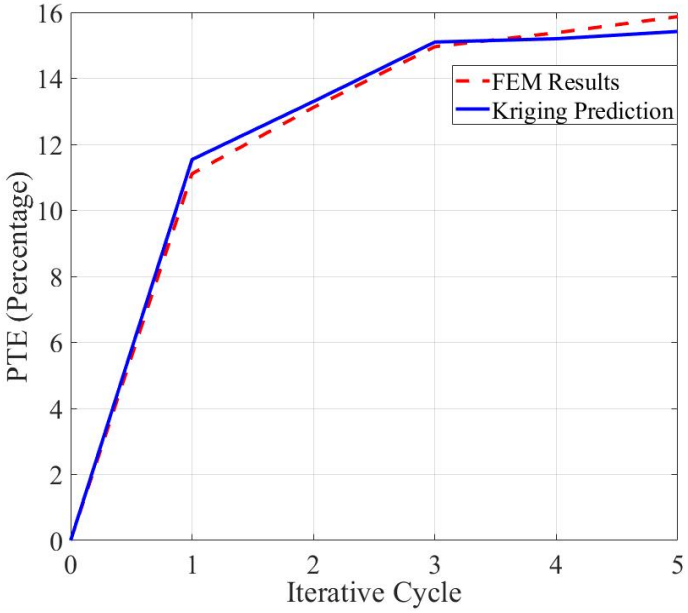

Fig. 4.6. Comparison of a full FEM simulation and the proposed Kriging model on the objective function values of the best candidates in the five iterative cycles.

To showcase the accuracy of the proposed refinement methodology, a comparative study, using the proposed method; a sequential Kriging based method excluding the proposed refinement procedure (SKE), other things being equal; and a linear interpolation (LI) is conducted. The numerical results have shown that both the SEK and the LI methods have faced premature convergence to non-optima due to the significantly large errors of the models, while the proposed method is able to gradually pinpoint the exact optimum. The detailed results are compared in Table 4.2. Since it is infeasible to optimize this case study by using a full EM simulation directly, a roughly accurate surrogate model is reconstructed to represent the entire design space by using a more sampling points model, that is a 400-sample points DOE model. Using this computationally heavy DOE model, the final optimized PTE is 15.97%, very close to the optimal solution of the proposed methodology; and however, the time taken for the optimization using this heavy DOE model is more than two times of the proposed methodology, not to mention the time for a full EM simulation without any help from a surrogate model. Moreover, due to the independence of each subspace, in the proposed method, a parallel computing technique can be employed to further increase

the solution speed. Figure 4.6 compares the objective function values of the best candidates in the five iterative cycles using a full FEM simulation and the corresponding Kriging models. The two results agree very well, and the error is within 5%, indicating the proposed method can accurately reconstruct the design space, especially at the function optima.

To show the magnetic field enhancement effects of different HMM structures, Figure 4.7 gives the log scale plot of the magnetic field distribution of the HMM assisted WPT system. From this colour map plot, it can be clearly seen that there is a very narrow tunnel created at the centre of the HMM slab, which in turn manipulates the propagation of the magnetic field as well as the transmission of the electric energy. Moreover, the field at the receiving coil Rx is comparable in magnitude to the field at the transmitting coil Tx, indicating a high PTE due to the application of the HMM slab.

To further investigate the performance as well as the advantage of the proposed HMM slab as compared to other geometrical MM slabs in existing WPT applications, Figure 4.8 (a)~(c) give intuitively the magnetic field distributions on one side of a HMM slab at the vertical (*x*-*o*-*y*) plane perpendicular to the transmission direction for the proposed HMM slab, the HMM slab with only one defect unit cell at the centre, and the homogeneous MM slab with all identical unit cells, respectively. The excitation sources for all three cases are identical. From these numerical results depicted in Figure 4.7 and Figure 4.8, it can be concluded that:

(1) The MM structures serve as intermediate station for the energy transmission. It can be clearly seen that the magnetic field is stronger near the MM structure, and the strength of the field is comparable to the source field at Tx and Rx coils.

(2) The magnetic near field is confined in the cavity created by the HMM slab in both case 1 and case 2. The confined field is much stronger when compared with the field enhancement in a homogeneous slab, which can be seen by comparing the color legend.

(3) Moreover, a stronger B-field is observed in the optimized HMM slab as compared to the HMM slab of case 2, and hence a higher PTE is expected.

(4) The PTEs for the three cases are sequentially 15.38%, 11.5% and 3.8%, which are also in good agreements with the *H*-field distributions.

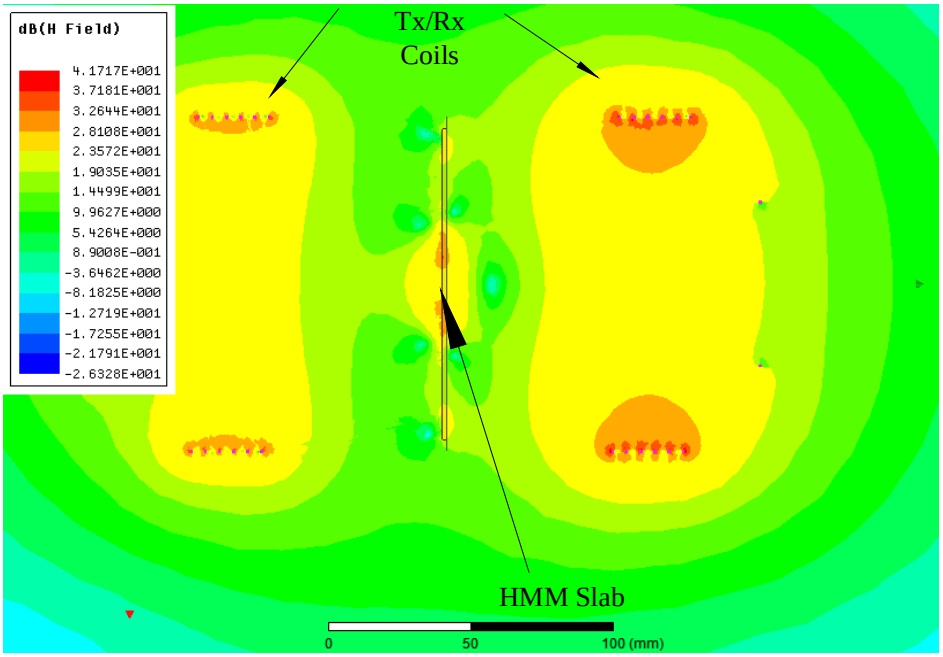

Fig. 4.7. Propagation of *B* field in HMM assisted WPT system.

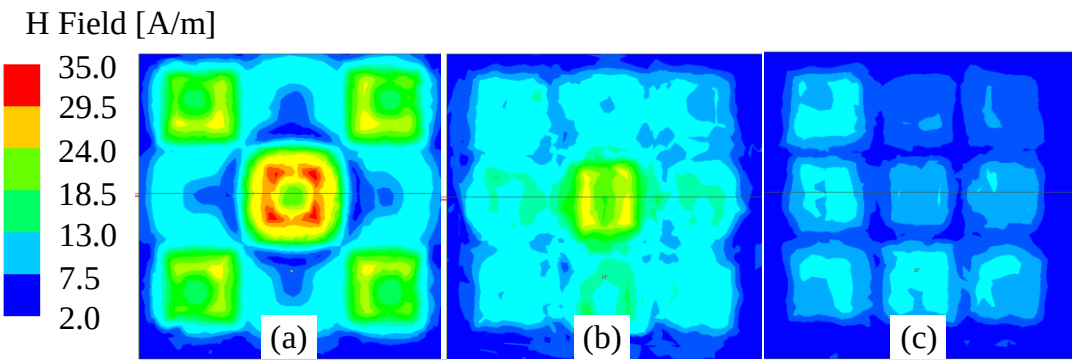

Fig. 4.8. *B*-field distributions for (a) proposed HMM slab, (b) HMM slab with only one defect at centre, and (c) Homogenous slab.

(2) Experimental Verification

To experimentally validate the feasibility and the performance of the proposed optimized HMM slab, a series of R-WPT experimental studies are conducted. The experimental setup follows the FEM simulation exactly, and the prototype is given in Figure 4.9. As explained in the previous session, in the system both Tx and Rx coils have an inductance of 23.3 μH, measured using a high-frequency LCR meter, and are connected to a 6-pF capacitor to fine tune the resonance frequencies. Moreover, it is

found that the currents in the coils have no phase difference to the applied voltages at 13.88 MHz when measured using a current probe connected with a high-performance oscilloscope, and hence 13.88 MHz is the resonance frequency. A 1 V peak-to-peak AC voltage and a 5 V peak-to-peak AC voltage are, respectively, applied to the source coil and the induced voltage (*IV*) at the load coil is measured in three cases:

1) Without any MM slab;

2) With a homogeneous slab that has all unit cells working in resonance at 13.9 MHz at the middle of the Tx and Rx coils;

3) The proposed HMM slab with three different types of unit cells at the middle of the Tx and Rx coils.

Because the load condition does not change for all three cases, the enhancement in PTE due to the addition of the MM slab is determined using the ratio between the measured voltages at the Rx end when there is MM slab, $V_{\text{with MM}}$, to that of where these is no MM slab, $V_{\text{w/o MM}}$:

$$\Delta PTE = \left(\frac{V_{\text{with MM}}}{V_{\text{w/o MM}}} \right)^2 \tag{4.10}$$

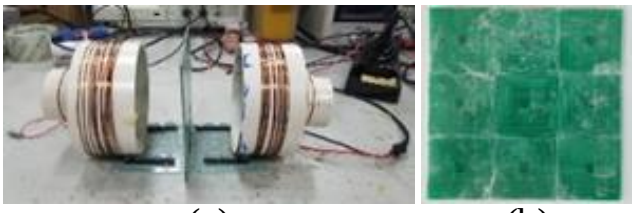

(a) (b)

Fig. 4.9. (a) Experimental setup (side view). (b) Actual HMM slab.

The experimental results are given in Table 4.3. It can be seen that there is an increment of 120% PTE enhancement when the proposed HMM slab is used, which is about twice larger than that when a uniform MM slab is used; and in both the high and low voltage excitations cases, the results are almost consistent. These results quantitatively illustrate the success of the proposed method in the optimization of an HMM slab.

Table 4.3 Experiment results

	Source P-to-P 1V			Source P-to-P 5V		
	Case 1	Case 2	Case 3	Case 1	Case 2	Case 3
IV	68.4mV	85.6mV	103mV	0.82V	1.07V	1.25V
ΔPTE	/	56.6%	126.8%	/	70.3%	132.4%

4.1.4 Further Step: Derivation of the Analytical Model for the MM Structure in WPT System

Because of the loss of uniformity in all directions of the MM in low frequency regime, the effective parameter extraction methods that work in the high frequency regime no longer valid in the low frequency counterpart, as explained in section 2.3. Hence, based on the fundamental Maxwell's equation, the numerical model of MM structure in magnetic field is derived to help the fellow researchers in the analysis and design of low frequency metamaterials. The aim of this study is thus to develop appropriate analytical equation for parameter extraction of the metamaterial in relatively low working frequency. A simple electromagnet as shown in Figure. 4.10 is used as an example for investigations. The main body of the electromagnet is a *C*-shape iron core. It has an airgap in the left side of the iron core and has a copper coil with an ac current source in the right side. An MM structure is placed inside the airgap. Its unit structure is a multi-turn copper planar spiral and is wounded on an air box. The planar spiral is connected to a small chip capacitor, and hence a circuit resonance can be taken place at a selected frequency.

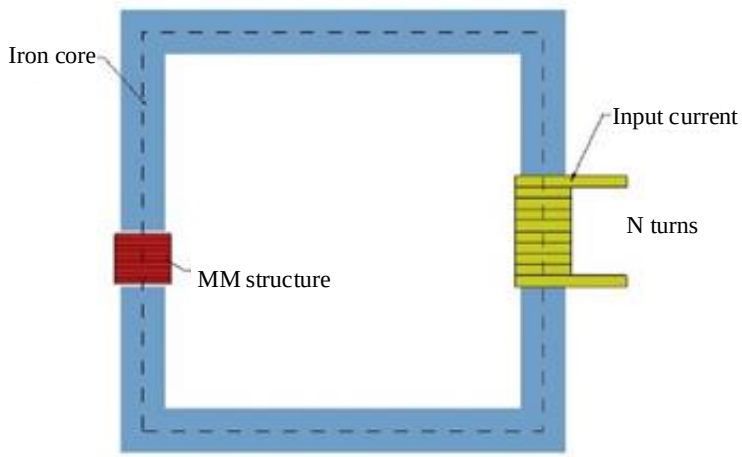

Fig. 4.10. C-shape electromagnet with an MM structure.

To simplify the modelling problem, it is assumed the magnetic field is evenly distributed throughout the cross-sectional area of the iron core, and its leakage flux is negligible. For the close path drawn in Figure. 4.10 formed by the center line of the electromagnet, two coils, one being the excitation source on the right, and another being the short-circuited coil with a capacitor connected in series on the left, are enclosed by the close path. Based on the balance equation of magneto motive force (m.m.f.) in the close path and the Kirchhoff's voltage law in the MM structure, the governing equations of this special system can be written as:

$$\dot{H}_{Fe} l_{Fe} + \dot{H}_g l_g + \dot{H}_m l_m = N_s \dot{I}_s + N_m \dot{I}_m \tag{4.11}$$

$$j\omega M_{s-m} \dot{I}_s + j\omega L_m \dot{I}_m + \frac{1}{j\omega C_m} \dot{I}_m + R_m \dot{I}_m = 0 \tag{4.12}$$

In equations 4.11 and 4.12, subscripts Fe, g, m, and s stand for iron core, airgap, metamaterial structure, and the source coil, respectively; $\dot{H}$ represents the complex magnetic field strength; l represents the average length of magnetic flux path; N represents the number of turns; $\dot{I}$ represents the complex current flowing in coils; M_{s-m} represents the mutual inductance between the source coil and the MM structure; ω is the angular frequency of the input current; and L_m, C_m, and R_m are the self-inductance, the overall capacitance, and the resistance of the MM circuit, respectively. To simplify the problem, assume the parasitic capacitance is much smaller than the

lump capacitance, and hence C_m is equal to the capacitance of the lump capacitor. The excitation source, $\dot{I}_s$, generates a time-varying magnetic field. This field interacts with the NEMR structure, and a time-varying current, $\dot{I}_m$, will be then generated in the NEMR structure. To derive the relationship between the two currents, simplifying the equation 4.12 one has:

$$\frac{\dot{I}_m}{\dot{I}_s} = -\frac{j\omega M_{s-m}}{j(\omega L_m - \frac{1}{\omega C_m}) + R_m} \tag{4.13}$$

Based on Faraday's Law of induction, the induced EMF by a time-varying magnetic field is always trying to weaken the magnetic field strength, and this relationship is described by the negative sign at the right-hand side of the equation 4.13. Moreover, in an ideal case where the copper wire has no resistance, i.e. R_m equals zero, or the frequency is large enough so that R_m is not comparable to $\left(\omega L_m - \frac{1}{\omega C_m}\right)$, the equation 4.13 is simplified into:

$$\frac{\dot{I}_{m(ideal)}}{\dot{I}_s} = -\frac{j\omega M_{s-m}}{j(\omega L_m - \frac{1}{\omega C_m})} = -\frac{\omega M_{s-m}}{\omega L_m - \frac{1}{\omega C_m}} \tag{4.13a}$$

From equation 4.13a, if all circuit component, i.e. L_m, C_m and M_{s-m}, are fixed, and the angular frequency of the current source, ω, is left as a variable, and set:

$$\omega_m = \frac{1}{\sqrt{L_m C_m}} \tag{4.14}$$

It can be found when $\left(\omega L_m - \frac{1}{\omega C_m}\right) \to 0^-$, or $\omega \to \omega_m^-$, a very large magnitude, the same phase $\dot{I}_m$ can be produced by the same $\dot{I}_s$, and the resultant magnetic field strength of the two currents will be significantly larger than the magnetic field strength produced solely by the excitation source, or in another word, the case where the NEMR structure is not presented.

For the convenience of computations, equation 4.13 is transformed to a phasor representation:

$$\frac{\dot{I}_m}{\dot{I}_s} = -\frac{j\omega M_{s-m}}{j(\omega L_m - \frac{1}{\omega C_m}) + R_m} = -\frac{\omega M \measuredangle \frac{\pi}{2}}{A \measuredangle \theta} = -\frac{\omega M}{A} \measuredangle \left(\frac{\pi}{2} - \theta \right) \tag{4.15}$$

where:

$$A = \sqrt{R_m^2 + \left(\omega L_m - \frac{1}{\omega C_m} \right)^2} \quad \text{and} \quad \theta = \tan^{-1} \left(\frac{\omega L_m - \frac{1}{\omega C_m}}{R_m} \right) \tag{4.15a}$$

If the values of the circuit components are set as in Table 4.4, the ratio of the induced current over the input current, $\frac{\dot{I}_m}{\dot{I}_s}$, is shown in Figure 4.11:

Table 4.4 The trial values of the parameters in equation 4.15

Component	Value
R_m	$1\,\Omega$
L_m	$100\,\mu H$
C_m	$10\,\text{n}F$
M_{s-m}	$300\,\mu H$
$f_m(\omega_m / 2\pi)$	159 KHz

In Figure 4.11(a), the maximum value of the real part of the ratio between the induced current in the NEMR structure and the excitation source, $\frac{\dot{I}_m}{\dot{I}_s}$, locates at 158365 Hz, which is slightly smaller than the resonance frequency, and at this frequency, the imaginary part of $\frac{\dot{I}_m}{\dot{I}_s}$ equals to -150. However, due to the reason that R_m has a value, it can be seen that the two currents are not in the same phase, despite the fact that the current in the MM has a very large amplitude. To further investigate the resultant

magnetic field produced by the NEMR structure and the excitation source, substitute equation 4.15 back into equation 4.11, and assume all materials are linear and unsaturated, the cross-sectional area along the magnetic flux path is the same and a uniform magnitude of the magnetic flux density $\dot{B}$ in the magnetic circuit:

$$\begin{aligned}&\frac{\dot{B}l_{\mathrm{Fe}}}{\mu_0\mu_{\mathrm{Fe}}}+\frac{\dot{B}l_g}{\mu_0}+\frac{\dot{B}l_m}{\mu_0}=N_s\dot{I}_s+N_m\dot{I}_m\\&=\dot{I}_s\left(N_s-N_m\frac{\omega M}{A}\measuredangle\left(\frac{\pi}{2}-\theta\right)\right)\end{aligned}\tag{4.16}$$

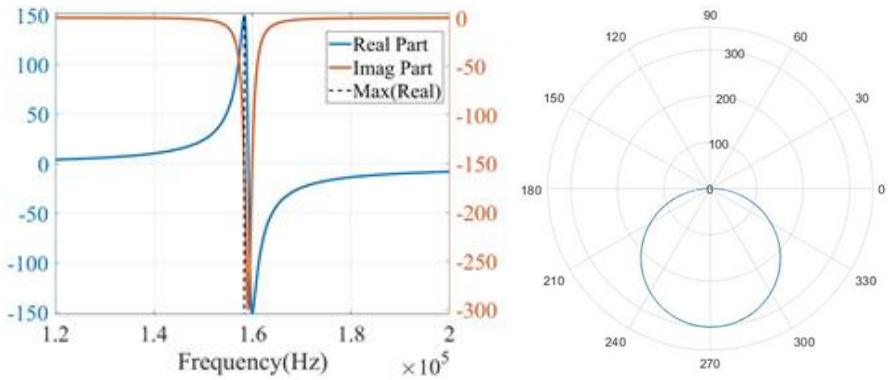

(a) (b)

Fig. 4.11. (a) Plot of real and imaginary part of $\frac{\dot{I}_m}{\dot{I}_s}$ *vs* input current frequency; (b) Polar plot of $\frac{\dot{I}_m}{\dot{I}_s}$.

Consider the case where the entire airgap is filled with the NEMR structure, and hence l_g = 0, then the equation 4.16 becomes:

$$\frac{\dot{B}l_{\mathrm{Fe}}}{\mu_0\mu_{\mathrm{Fe}}}+\frac{\dot{B}l_m}{\mu_0}=\dot{B}\left(\frac{l_{\mathrm{Fe}}}{\mu_0\mu_{\mathrm{Fe}}}+\frac{l_m}{\mu_0}\right)=\dot{I}_s\left(N_s-N_m\frac{\omega M}{A}\measuredangle\left(\frac{\pi}{2}-\theta\right)\right)\tag{4.16}$$

Solving for the magnetic flux density $\dot{B}$ in the magnetic circuit, one has:

$$\dot{B}=\frac{\dot{I}_s\left(N_s-N_m\frac{\omega M}{A}\measuredangle\left(\frac{\pi}{2}-\theta\right)\right)}{\left(\frac{l_{\mathrm{Fe}}}{\mu_0\mu_{\mathrm{Fe}}}+\frac{l_m}{\mu_0}\right)}=\frac{\dot{I}_s\mu_0\left(N_s-N_m\frac{\omega M}{A}\measuredangle\left(\frac{\pi}{2}-\theta\right)\right)}{\frac{l_{\mathrm{Fe}}}{\mu_{\mathrm{Fe}}}+l_m}\tag{4.17}$$

If the MM structure is considered as a special reluctance structure in the magnetic circuit without any source inside, its effective magnetic field strength meets the following equation:

$$\dot{H}_{\text{eff}} = \frac{\dot{H}_m l_m - N_m \dot{I}_m}{l_m} = \frac{\dot{B}}{\mu_0} + \dot{I}_s N_m \frac{\omega M}{A l_m} \measuredangle\left(\frac{\pi}{2} - \theta\right) \tag{4.18}$$

Substitute $\dot{B}$ in the equation 4.17 back into the equation 4.18, and simplify the equation 4.18, it becomes:

$$\dot{H}_{\text{eff}} = \frac{\dot{B}}{\mu_0} + \dot{I}_s N_m \frac{\omega M}{A l_m} \measuredangle\left(\frac{\pi}{2} - \theta\right) = \dot{I}_s \frac{N_s + \frac{l_{\text{Fe}}}{\mu_{\text{Fe}} l_m} N_m \frac{\omega M}{A} \measuredangle\left(\frac{\pi}{2} - \theta\right)}{\frac{l_{\text{Fe}}}{\mu_{\text{Fe}}} + l_m} \tag{4.18a}$$

Assuming the MM structure is homogeneous, the effective magnetic permeability, $\dot{\mu}_m = \frac{\dot{B}}{\dot{H}_{\text{eff}}}$, and the equivalent magnetic reluctance, $\dot{\Re}_{\text{eq}}$, for the MM structure in the magnetic circuit are:

$$\dot{\mu}_m = \frac{\dot{B}}{\dot{H}_{\text{eff}} \mu_0} = \frac{N_s - N_m \frac{\omega M}{A} \measuredangle\left(\frac{\pi}{2} - \theta\right)}{N_s + N_m \frac{l_{\text{Fe}}}{\mu_{\text{Fe}} l_m} \frac{\omega M}{A} \measuredangle\left(\frac{\pi}{2} - \theta\right)} \tag{4.19}$$

$$\dot{\Re}_{\text{eq}} = \frac{l_m}{\mu_0 \dot{\mu}_m S} = \frac{N_s l_m + N_m \frac{l_{\text{Fe}}}{\mu_{\text{Fe}}} \frac{\omega M}{A} \measuredangle\left(\frac{\pi}{2} - \theta\right)}{N_s - N_m \frac{\omega M}{A} \measuredangle\left(\frac{\pi}{2} - \theta\right)} \times \frac{1}{\mu_0 S} \tag{4.20}$$

In equation 4.20, S is the cross-sectional area of the MM in the direction perpendicular to the magnetic field. The magnetic reluctance of airgap without NEMR is:

$$\Re_{\text{m}} = \frac{l_m}{\mu_0 S} \tag{4.20a}$$

Reformulating equation 4.20 to take out $\Re_{\text{m}}$:

$$\dot{\Re}_{\text{eq}} = \frac{l_m}{\mu_0 \dot{\mu}_m S} = \frac{l_m}{\mu_0 S}\left(1 + \frac{1 - \dot{\mu}_m}{\dot{\mu}_m}\right) = \Re_m + \frac{1}{\mu_0 S} \frac{N_m \frac{\omega M}{A}\left(\frac{l_{\text{Fe}}}{\mu_{\text{Fe}}} + l_m\right) \measuredangle\left(\frac{\pi}{2} - \theta\right)}{N_s - N_m \frac{\omega M}{A} \measuredangle\left(\frac{\pi}{2} - \theta\right)} \tag{4.21}$$

The equivalent magnetic reluctance of the MM structure contains a real constant part and a complex part associated with the physical parameters of both the MM structure and the iron core and does not rely on the excitation current. The second term in (4.21) describes this complex reluctance. If this term is large enough with a negative value, the negative equivalent magnetic reluctance can be achieved. In this problem, the number of turns of the source coil, N_s, is fixed, and $l_{Fe} \gg l_m$ so that any variation in the length of the NEMR structure does not significantly affect the length of the iron core, and hence l_{Fe} can also be regarded as a constant. The mutual inductance, M and L in equation 4.21 can be rewritten as:

$$M = k\sqrt{L_{\mathrm{Fe}} L_m} \tag{4.21a}$$

$$L \cong \frac{\mu N^2 A}{l} \tag{4.21b}$$

where k is the coupling coefficient of the source coil and the MM structure. Once the length of the MM structure is fixed, the inductance of the structure will become a constant as well. Based on equations 4.21-4.21b, the graph of the frequency of excitation source versus equivalent reluctance keeping capacitance as constant, and the graph of the capacitance of the MM structure versus equivalent reluctance keeping frequency constant are plotted in Figure 4.12. Here all parameter values for all circuit components in the equation 4.19 and equation 4.20 are given in Table 4.5.

Table 4.5 The values of all parameters for numerical experiment

Component	Value
R_m	0.342 $m\Omega$
L_m	19.73 μH
C_m	128 nF
M_{s-m}	77.33 μH
$f_m(\omega_m / 2\pi)$	100 kHz
$\Re_m$	4.93 MWb
L_{Fe}	717.3 μH

l_m	10 *mm*
l_{Fe}	1430 *mm*
s	1600 mm^2

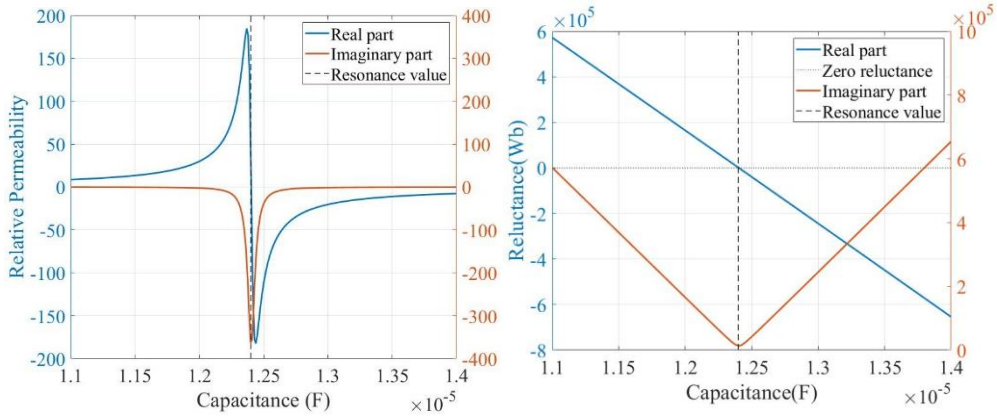

Fig. 4.12. The Plot of (a) Capacitance vs Relative permeability; and (b) Capacitance vs Reluctance; of the proposed NEMR structure.

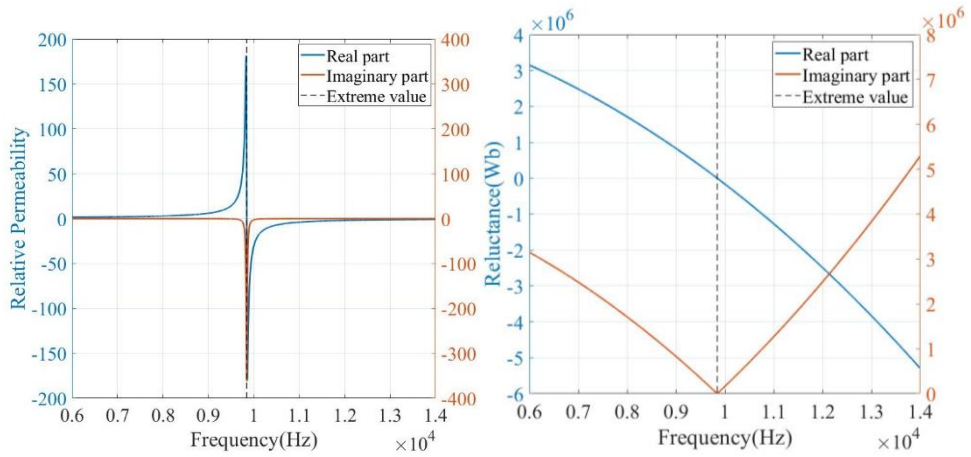

Fig. 4.13. The Plot of (a) Frequency vs Relative permeability; and (b) Frequency vs Reluctance; of the proposed NEMR structure.

From the numerical results in Figure 4.12 and Figure 4.13, at the frequency close to and lower than the resonance frequency of the structure, there is a sharp transition of effective permeability from positive values to negative values, and this observation is in good agreement with the conclusion obtained from the analytical model of the ratio between the excitation current and the induced current. Moreover, at this specific frequency, there is also a minimum of the magnitude of the effective reluctance of the

structure, the real part of the reluctance is close to zero and hence at this frequency the magnetic field induced by the excitation current in the MM structure will be strongest and has a 90 degrees phase difference with the current. Table 4.6 describes the electromagnetic properties of the proposed MM structure when its axial length and the number of turns of the coils vary when the resonance frequency of the structure remains at 100 KHz. It can be seen that when the number of turns is small, the minimum value occurs at a point further from the resonance point and *vice versa*, and the trend of increments become smaller and smaller when the number of turns increases, and it can be seen that after 14 turns, the increase in the number of turns of the coil no longer significantly affects the frequency minimum value as well as the minimum permeability. This pattern applies to the equivalent reluctance as well.

Table 4.6. Electromagnetic properties of the proposed NEMR structure at different number of turns

Number of turns	Frequency at min real permeability F_{m1}	Min permeability at F_{m1}	Frequency at min $\lvert\dot{\Re}_{eq}\rvert$, F_{m2}	Min $\dot{\Re}_{eq}$ at F_{m2}
2	9327 Hz	-171.2 + 175.8i	9315	2892.99
4	9625 Hz	-176.6 + 171.2i	9612	5603.12
6	9742 Hz	-178.9 + 184.2i	9729	8308.60
8	9805 Hz	-180.0 + 187.7i	9792	11006.59
10	9845 Hz	-180.8 + 179.8i	9832	13697.34
12	9872 Hz	-181.3 + 179.2i	9859	16397.06
14	9891 Hz	-181.6 + 187.2i	9878	19083.07
16	9906 Hz	-181.9 + 185.4i	9893	21776.75
18	9918 Hz	-182.2 + 180.9i	9905	24484.78
20	9927 Hz	-182.3 + 186.6i	9914	27163.17

4.2 A Vector Wind Driven Optimization Algorithm for Multi-Objective Topology Optimizations

4.2.1 Multi-Objective Design Optimization and Wind Driven Optimization Algorithm

In engineering design problems, it is a common practice to ask the designer to reach a compromise between several seemingly conflicting criteria/objectives, for instance, the cost and the performance of a machine. Generally, the final solutions of such a problem are a set of tradeoffs, called Pareto optimal solutions, of different objectives or criteria. Consequently, an acceptable vector (multi-objective) optimizer should have the ability to find as many Pareto optimal solutions as possible, and these solutions should also be as uniformly distributed as possible. To achieve these two ultimate goals, a huge amount of efforts has been devoted to the advancement of evolutionary and meta-heuristic algorithms, because of their appropriateness in producing proper approximations of the Pareto optimal solutions, or Pareto front, in a single run of algorithm [D23-D24].

Nevertheless, the situation in regard to the searching ability, the numerical complexity, and the convergent speed of existing vector evolutionary and meta-heuristic algorithms is still unsatisfactory and requires a continuous effort. Moreover, there is no universal vector algorithm which can be applied equally and successfully to all multi-objective inverse problems [D25]. As a result, it is essential to retain and ensure there are sufficient diversity in the vector optimizers when studying multi-objective inverse and optimal problems in computational electromagnetics. In this regard, a vector wind driven optimization (WDO) algorithm is proposed due to its simpleness and easiness in numerical implementations.

Nature phenomenon is a perfect inspiration to develop evolutionary algorithms. The WDO algorithm is inspired from the modeling of the climate [D26-D27]. In the living environment wind blows from the high-pressure zone to the low-pressure zone at various speeds to equalize the imbalances in air pressure. Based on Newton’s second

law of motion, the velocity vector, v, and the position vector, x, of the vector WDO algorithm are updated using [D27]:

$$v(k+1) = (1-\alpha)v(k) - gx(k) + (RT\left|1-\frac{1}{i}\right|(x_{opt} - x(k))) + \frac{[cv^{\text{othr_dim}}(k)]}{i} \tag{4.22}$$

$$x(k+1) = x(k) + \Delta t \times v(k+1) \tag{4.23}$$

where α is a friction coefficient, g is the gravitational constant, R is the universal gas constant, T is the temperature, c is a pre-defined constant to adjust the inertia from the previous iteration, i is the ranking among all air parcels, x_{opt} is the best parcel so far searched, and Δt is the step length.

Compared with other nature-inspired optimal algorithms, WDO is relatively simple and easy to be implemented numerically. However, as a new stochastic algorithm, WDO may be prone to premature convergences when solving complex optimization problems [D27], due to the possible diversity loss of the parcels and the corresponding imbalance between exploration and exploitation searches. Moreover, lukewarm efforts have been devoted to extend this new stochastic algorithm to multi-objective optimization problems [D28], especially in the studies of inverse and optimization problems in electromagnetics. In this regard, this chapter will further explore the potential of WDOs to solve a multi-objective design optimization or inverse problem of electromagnetic devices.

4.2.2 A Vector Wind Driven Optimization Algorithm

To ensure enough diversities in the later searching stages of a single objective (scalar) WDO and to extend the scalar WDO to a vector one, some improvements are implemented to the ordinary WDO algorithm. The second term, $-gx(k)$, in equation 4.22 represents the gravitational force, which is in fact an attractive force, that pulls the parcels towards the absolute origin of the coordinate system. Since every parcel is always attracted towards this absolute origin under the influence of this gravitational force, the diversity of the parcels is reduced. To address this problem, this term is removed from the proposed WDO method in this chapter. Moreover, to ensure a good

balance between exploration and exploitation searches, a new parameter w , is introduced in the position updating equation in equation 4.23. Hence, the original updating functions equation 4.22 and equation 4.23 becomes:

$$v(k+1) = (1-\alpha)v(k) + (RT\left|1-\frac{1}{i}\right|(x_{opt} - x(k)))) + \left(\frac{cv^{\text{othr_dim}}(k)}{i}\right) \tag{4.24}$$

$$x(k+1) = w \times x(k) + (1-w) \times \Delta t \times v(k+1) \tag{4.25}$$

The newly added parameter w serves as a control parameter and decreases linearly from a maximum value to a minimal value in the iterative process of the proposed algorithm. The last term, $\left(\frac{cv^{\text{othr_dim}}(k)}{i}\right)$ in equation 4.24, introduces certain level of perturbations to the velocity vector to retain the algorithm diversity. Obviously, it functions as a mutation operator being used in an evolutionary algorithm. However, towards the end of the searching stages of the algorithm in solving complex optimal design problems, the velocity vector might possibly converge to zero, leading to the existence of a stagnation phenomenon and the algorithm will then be trapped in a local optimum. In other word, in the early searching stage of a WDO algorithm, the diversity of the parcels is relatively high since the initial velocity vector is randomly and independently generated; and it will be continuously decreased with the evolution of the algorithm. In these points of views, the perturbed increment implemented by the mutation operation should be large when the diversity of the population is smaller and vice versa. Moreover, the standard deviation of the parcels in the current population is a proper metric to gauge the diversity of the population. In this regard, an adaptive mutation is designed, and equation 4.24 is modified to:

$$v(k+1) = (1-\alpha)v(k) + (RT\left|1-\frac{1}{i}\right|(x_{opt} - x(k)))) + (2r-1)\Delta_{\max}e^{-\sigma} \tag{4.26}$$

$$\begin{aligned} \sigma &= \sqrt{\sum_{i=1}^{N}(x_i(k)-\mu)^2} \\ \mu &= \sum_{i=1}^{N} x_i(k)/N \end{aligned} \tag{4.27}$$

where r is a random number generated in $[0,1]$, $\Delta_{\max}$ is the maximum perturbation

increment, and N is the size of the population.

Approaches oriented for multi-objective optimizations

In updating the position of a parcel in a scalar WDO algorithm, the best parcel so far searched is used to guide the search direction toward promising solutions. Nevertheless, the optimal solutions of a multi-objective design problem are not unique but a set of non-dominated solutions containing tradeoffs among different objectives. This feature will give rise to a dilemma in selecting the best parcel when updating the current parcel since the fitness values of all Pareto optimal solutions are the same. Moreover, the dominant concept is generally employed in a vector optimizer to determine the fitness value of an individual in a multi-objective optimal problem. However, such approach may only determine qualitatively the relationship of dominances and may not measure, quantitatively, the number of the improved objectives [D29]. The amount of improvements in a specified objective may not be quantified either. To address the aforementioned two issues, a metric gauging the improvements in the aforementioned two aspects is introduced. For a parcel x_m with k objective functions the proposed metric is computed by:

$$\varepsilon_{improve}(x_m) = \sum_{\substack{j=1 \\ j\neq k}}^{N} \sum_{l=1}^{k} \mathrm{sgn}\left[f_l(x_j) - f_l(x_m) \right] \left\{ \frac{1}{k} + \frac{f_l(x_j) - f_l(x_m)}{(f_l)_{\max} - (f_l)_{\min}} \right\} \tag{4.28}$$

$$\mathrm{sgn}(x) = \begin{cases} 1 & (x > 0) \\ 0 & (\text{otherwise}) \end{cases} \tag{4.29}$$

Using this accumulation factor to penalize the fitness value of all parcels in the current population, the fitness of x_m can be calculated as:

$$f_{fit}(x_m) = r f_{fit}^{nor}(x_m) + (1-r)\varepsilon_{improve}(x_m) \tag{4.30}$$

where $f_{fit}^{nor}(x_m)$ is the normally defined fitness of x_m using a dominance relationship, r is a random parameter generated randomly in $[0,1]$.

To maintain a good balance between exploration and exploitation searches, the iterative procedures of the proposed algorithm are divided into two phases: an exploration search phase and an exploiting search phase. The goal of the exploration

search phase is to guarantee the diversity of the parcels as well as the corresponding final solutions while that of the exploiting search phase is to find improved solutions efficiently and reliably. As a result, different searching strategies are used in the two searching phases. To control the direction of the searches of the proposed vector WDO algorithm in the exploiting search phase to find improved high-performance solutions, the metric parameter as defined in equation 4.28 is used as both the driving force to evaluate a parcel and the performance metric to select the best parcel in updating the velocity of a parcel while that in equation 4.30 is selected as the driving force to facilitate exploration searches of the whole feasible space. The algorithm starts from the exploration phase. Once Pareto optimal solutions of a pre-defined minimum number are located, the algorithm will then enter into the exploiting searching phase until it either successfully found an improved solution in every parcel or the number of consecutive iterations without finding any new Pareto optimal solution exceeds a predefined value. The two phases are continuously alternated until a global stop criterion is satisfied.

4.2.3 Numerical Applications of the Proposed vector WDO Algorithm

To test the proposed WDO based vector optimizer, it is numerically experimented on different case studies and its performances are compared to those of existing evolutionary algorithms.

(1) Antenna Array Optimization

In this case study, a desired field pattern of a shaped beam with a cosecant variation is reconstructed using a nonuniformly spaced antenna array. The desired pattern is defined as [D31]: the field will vary following a cosecant function in the interval $\cos\theta \in [0.1, 0.5]$ having a Maximum Side-Lobe Level (MSLL) smaller than -22 dB in the residual intervals. Mathematically, the desired pattern is expressed as [D31]:

$$F_{\text{desired}}(\cos\theta) = \begin{cases} \csc(\cos\theta) & (0.1 \le \cos\theta \le 0.5) \\ 0 & (\text{elsewhere}) \end{cases} \qquad (4.31)$$

$$MSLL_{\text{desired}} \le -22\text{dB}$$

To produce a close approximation to this desired field pattern, a completely non-uniform antenna array, as shown in Figure. 4.14, is optimized with a minimal number of elements with respect to the following objective function [D31]:

$$\min f_1 = \sqrt{\frac{\sum_{i=1}^{N}\left[f_{\text{desired}}^{\text{norm}}(\theta_i) - f_{\text{designed}}^{\text{norm}}(\theta_i)\right]^2}{\sum_{i=1}^{N}\left[f_{\text{desired}}^{\text{norm}}(\theta_i)\right]^2}} \qquad (4.32)$$

where $f_{\text{desired}}^{\text{norm}}(\theta_i)$ is the value of the normalized desired radiation pattern at sampling point θ_i, $f_{\text{designed}}^{\text{norm}}(\theta_i)$ is the value of the normalized radiation pattern produced by a designed array of *M* elements, and *N* is the number of total sampling points.

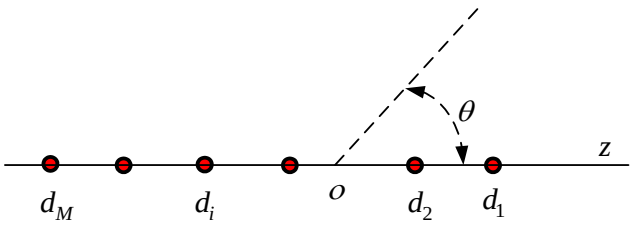

Fig. 4.14. The configuration of *M*-element linear arrays placed on the *z*-axis.

To compromise the requirement on the MSLL and the field pattern, the second objective is to minimize the MSLL. Consequently, the two-objective synthesis problem is formulated as:

$$\min \begin{cases} f_1 \\ f_2 = MSLL_{desired} \end{cases} \qquad (4.33)$$

The computation of the field pattern is reffered to [D15]. To quantitatively evaluate the performances of a vector optimal algorithm, the *convergence* metric γ is used to measure the convergence of its final solution set to a known set of the Pareto solutions, while the displacement metric is employed to gauge its uniformity or diversity performance of the attained solutions over the non-dominated front [D29]. If the set consisting of the uniformly spaced true Pareto solutions, which are obtained

using an exhaustive approach in this case study, is P^*; and the set of the final solution of the vector optimizer is Q, the aforementioned two metrics become:

$$\gamma = \sum_{i=1}^{|Q|} \left(\frac{\min_{j \in [1,|P^*|]} (d(i,j))}{|Q|} \right) \tag{4.34}$$

$$displacement = \sum_{i=1}^{|P^*|} \left(\min_{j \in [1,|Q|]} (d(i,j)) \right) \Big/ |P^*| \tag{4.35}$$

where $d(\bullet,\bullet)$ is the Euclidean distance of the two set solutions. In this case study, a 19-element nonuniform antenna array is optimized to find the Pareto optimal solutions of the two conflicting objectives of equation 4.33. For performance comparisons, this case study is solved by the proposed algorithm and the improved vector tabu search algorithm [D30]. Moreover, to evaluate the average performance of an algorithm, each algorithm is run randomly and independently 10 times. The averaged performances of the 10 runs for the two algorithms are summarized as:

(1) The numbers of iterations for the proposed algorithm and the vector tabu search algorithm are, respectively, 26794 and 29465.

(2) The parameters γ and $displacement$ of the final solution for the proposed algorithm are, respectively, 0.000016 and 0.00028; while the metric γ and $displacement$ of the final solution for the vector tabu search method are, respectively, 1.8×10^{-5} and 2.9×10^{-4}, and hence can be concluded that the proposed vector WDO algorithm has advantages in solving multi-objective optimal design problems.

(2) Design Optimizations of a Multi-Sectional Pole Arcs of a Large Hydro-Generator

The design optimization of the multi-sectional pole arcs of a large hydro-generator [D31] is then solved. The problem is mathematically formulated as:

$$\begin{aligned} &\max B_{f_1}(X) \\ &\min e_v \\ &\text{s.t.} \quad SCR - SCR_0 \ge 0 \\ &\qquad X'_d - X'_{d0} \le 0 \\ &\qquad THF - THF_0 \le 0 \end{aligned} \tag{4.36}$$

where B_{f_1} is the amplitude of the fundamental component of the flux density in the air gap, e_v is the distortion factor of a sinusoidal voltage of the machine under no-load condition, THF is the abbreviation of the Telephone Harmonic Factor, X'_d is the direct axis transient reactance of the generator, SCR is the abbreviation of the Short Circuit Ratio, and SCR_0 , X'_{d0} and THF_0 are the limit values of the corresponding performance parameter, SCR, X'_d and THF .

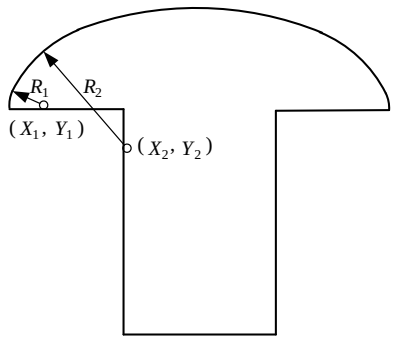

Fig. 4.15. The design variables of the multi-sectional pole shoes.

The geometrical parameters, the center positions, and radii of the multi-sectional arcs of the pole shoe, as shown in Figure 4.15, are optimized to obtain a series of trade-off solutions of this case study. For performance comparisons, the multi-sectional pole arcs of a 300 MW, 20-pole hydro-generator are optimized by using the proposed vector WDO and the improved vector tabu search optimizers [D30]. In the numerical implementations, the magnetic fields of the hydro-generator at no-load conditions are computed using a finite element method, and the performance parameters as required in equation 4.36 are then determined based on these finite element solutions. To give a fair comparison, the number of the non-dominated Pareto solutions is fixed for the two algorithms. Moreover, to give the average performances of the two algorithms, they are independently and randomly run 10 times. Since the true Pareto solutions, P^*, of this case study are unavailable, they are approximated by using the bested ones searched by the two vector optimizers in the 20 runs. The average parameters γ and $displacement$ of the final solutions for different algorithms are given in Table 4.7 in

details. Moreover, the corresponding number of iterations used by the two algorithms are presented in Table 4.7 as well. From the averaged performances of the three performance parameters, it is concluded that:

(1) The quality of the final solutions of the proposed WDO algorithm is better than that of the improved vector tabu search algorithm, because the averaged value of the convergence metric of the final solutions for the proposed algorithm is smaller than that for the improved tabu search method.

(2) The diversity of the final solutions of the proposed WDO algorithm is identical to that of the improved vector tabu search method, and this is because the average values of the $displacement$ metric of the final solutions for the two algorithms are almost the same.

(3) The proposed WDO based vector algorithm is a little faster than the improved vector tabu search method.

Table 4.7 Performance Comparison of Different Algorithms on Case Study Two

Algorithm	γ	*Displacement*	*No.* Iterations
The proposed WDO algorithm	0.000026	0.00045	1235
The improved Tabu search method	0.000028	0.00045	1248

4.3 Summary

In this chapter, numerical methodologies aiming to solve complex topology optimization problems, including large-scale 3-D design problems and multi-objective problems, are developed, and explained in detail, both involving large number computation burden. First, a DOE assisted surrogate and improved tabu search based sequential refinement method for design optimization of MM structures in R-WPT systems is proposed. By utilizing the surrogate method to replace the time-consuming

3-D FEM simulations, the solution time required to find the best objective values is significantly reduced, and hence an automated optimization can be performed. The numerical results indicate that, compared to the conventional surrogate method, the proposed one is able to reconstruct a sufficiently accurate surrogate model; and compared to a full DOE approach, the computational burden of the proposed methodology is very low. Moreover, the experimental verification results indicate the HMM slab obtained by using the proposed method is indeed better than an HMM slab without any optimization. Also, as explained in section 2, the effective parameter extraction methods developed for MM structure works only for the high frequency application, and however in low frequency regime, where the WPT applications fall in, there is no appropriate method to explain the field distribution of MM structure in low frequency condition. Hence, in this chapter an appropriate numerical method of MM structure in low frequency regime is developed. Lastly, this chapter developed a WDO based vector optimizer for multi-objective inverse and optimization problems. The numerical results on two case studies being reported have demonstrated that: (1) compared with an improved vector tabu search algorithm, the proposed algorithm can use relatively fewer iterations to find relatively higher quality final solutions; (2) the proposed WDO based vector optimizer can easily keep a good balance between minimizing the distance from the found solutions to the true Pareto front and maximizing the diversity among the found Pareto solutions. Comparing the two algorithms developed in this chapter, it can be seen that the first one is specially developed for complex problems and hence the algorithms itself is much more complex than the second one. Moreover, to ensure an effective optimizaiton process, the DOE-surrogate model-based need to be carefully calibrated, which takes a relatively long time. However, for the second algorithm, it is much simpler with a smaller number of algorithm parameters, and hence is only suitable for simpler issues and problems.

4.4 Reference-Part D

[D1] T. S. Pham, A. K. Ranaweera, V. D. Lam, and J.-W. Lee, "Experiments on localized wireless power transmission using a magneto-inductive wave two-dimensional metamaterial cavity," *Applied Physics Express*, vol. 9, no. 4, Art. No. 044101, 2016.

[D2] Z. Zhen and P. Hongliang, "Wireless power transfer — an overview," *IEEE Transactions on Industrial Electronics*, vol. 66, no. 2, pp. 1044–1058, 2019

[D3] F. Lu, H. Zhang, and C. Mi, "A review on the recent development of capacitive wireless power transfer technology," *Energies*, vol. 10, no. 11, p. 1752-1781, 2017.

[D4] H. Guan, L. Liu, S. Yang, and X. Chen, "Efficiency enhancement of wireless power transfer system by using resonant coil and negative permeability metamaterial," *International Journal of Applied Electromagnetics and Mechanics*, pp. 1-9, 2018.

[D5] H. Guo, Z. Sun, and C. Zhou, "Practical Design and Implementation of Metamaterial-Enhanced Magnetic Induction Communication," *IEEE Access*, vol. 5, pp. 17213-17229, 2017.

[D6] K. Sun, R. Fan, X. Zhang, Z. Zhang, Z. Shi, and N. Wang, "An overview of metamaterials and their achievements in wireless power transfer," *Journal of Materials Chem. C*, vol. 6, issue. 12, pp. 2925-2943, 2018.

[D7] H. Guan, L. Liu, S. Yang, and X. Chen, "Efficiency enhancement of wireless power transfer system by using resonant coil and negative permeability metamaterial," *International Journal of Applied Electromagnetics and Mechanics*, vol. 59, no. 2, pp. 647-655, 2019.

[D8] H. N. Bui, T. S. Pham, J.-S. Kim, and J.-W. Lee, "Field-focused reconfigurable magnetic metamaterial for wireless power transfer and propulsion of an untethered microrobot," *Journal of Magnetism and Magnetic Materials*, vol. 494, Art. No. 165778, 2020.

[D9] N. Kaina, F. Lemoult, M. Fink, and G. Lerosey, “Ultra small mode volume defect cavities in spatially ordered and disordered metamaterials,” *Applied Physics Letters*, vol. 102, no. 14, Art. No. 144104, 2013.

[D10] A. L. A. K. Ranaweera, C. A. Moscoso, and J.-W. Lee, “Anisotropic metamaterial for efficiency enhancement of mid-range wireless power transfer under coil misalignment,” *Journal of Physics D: Applied Physics*, vol. 48, no. 45, Art. No. 455104, 2015.

[D11] Y. Cho, S. Lee, D.-H. Kim, H. Kim, C. Song, S. Kong, J. Park, C. Seo, and J. Kim, “Thin hybrid metamaterial slab with negative and zero permeability for high efficiency and low electromagnetic field in wireless power transfer systems,” *IEEE Transactions on Electromagnetic Compatibility*, vol. 60, no. 4, pp. 1001–1009, 2018.

[D12] A. L. A. K. Ranaweera, T. P. Duong, and J.-W. Lee, “Experimental investigation of compact metamaterial for high efficiency mid-range wireless power transfer applications,” *Journal of Applied Physics*, vol. 116, no. 4, Art. No. 043914, 2014.

[D13] Y. Zhang, H. Tang, C. Yao, Y. Li and S. Xiao, “Experiments on adjustable magnetic metamaterials applied in megahertz wireless power transmission”, *AIP Advances*, vol. 5, no. 1, Art. No. 017142, 2015.

[D14] B. Wang, W. Yerazunis, and K. H. Teo, “Wireless power transfer based on metamaterials”, *Wireless Power Transfer Algorithms, Technologies and Applications in Ad Hoc Communication Networks*, pp. 31-53, 2016.

[D15] S. L. Ho, S. Yang, “Multi-objective synthesis of antenna arrays using a vector tabu search algorithm,” *IEEE Antennas and Wireless Propagation Letters*, vol. 8, pp.947-950, 2009.

[D16] Z. Xiaobo, “Comparison of response surface method and Kriging method for approximation modelling,” *2017 2nd International Conference on Power and Renewable Energy (ICPRE)*, Chengdu, pp. 66-70, 2017.

[D17] K. Hamza, M. Aly, and H. Hegazi, “A Kriging-interpolated level-set approach for structural topology optimization,” *Journal of Mechanical Design*, vol. 136, no. 1, Art. No. 011008, 2013.

[D18] T. Long, D. Wu, X. Chen, X. Guo, and L. Liu, “A deterministic sequential maximin Latin hypercube design method using successive local enumeration for metamodel-based optimization,” *Engineering Optimization*, vol. 48, no. 6, pp. 1019-1036, 2015.

[D19] Gang Lei, X. M. Chen, J. G. Zhu, Y. G. Guo, Wei Xu, K. R. Shao, “Multi-objective sequential optimization method for the design of industrial electromagnetic devices,” *IEEE Trans. Magn.*, vol. 48, no. 11, pp. 4538-4541, 2012.

[D20] Gang Lei, K. R. Shao, Youguang Guo, Jianguo Zhu, J. D. Lavers, “Improved sequential optimization method for high dimensional electromagnetic device optimization,” *IEEE Trans. Magn.*, vol. 45, no. 10, pp. 3993-3996, 2009.

[D21] X. Liu and W. N. Fu, “A dynamic dual-response-surface methodology for optimal design of a permanent-magnet motor using finite-element method,” *IEEE Trans. Magn*, vol. 52, no. 3, Art. No. 7204304, 2016.

[D22] Y. Zhang, S. L. Ho and W. Fu, “Applying response surface method to oil-immersed transformer cooling system for design optimization,” *IEEE Trans. Magn.*, vol. 54, no. 11, Art. No. 8401705, 2018.

[D23] L. Santos, et. al., “A multi-objective firefly approach using Beta probability distribution for electromagnetic optimization problems,” *IEEE Trans. Magn.*, vol.49, pp. 2085-2088, 2013.

[D24] P. Barba, “Multi-object ive shape design in electricity and magnetism,” Lecture *Notes in Electrical Engineering*, vol. 47, 2010.

[D25] D. Wolpert, and W. Macready, “No free lunch theorems for optimization”, *IEEE Trans. Evolutionary Computation*, vol.1, pp.67-82, 1997.

[D26] Z. Bayraktar, M. Komurcu, and D. H. Werner, "Wind Driven Optimization (WDO): A novel nature-inspired optimization algorithm and its application to electromagnetics," *Proceedings of the 2010 IEEE Antennas and Propagation Society International Symposium (APSURSI)*, Toronto, Canada, pp.1-4, 2010.

[D27] Z. Bao, and et. al., "A hybrid global optimization algorithm based on wind driven optimization and differential evolution," *Mathematical Problems in Engineering*, Article ID 389630, 2015.

[D28] H. Ayala, and E. Segundo, "Multi-objective wind driven optimization approach applied to transformer design," *Proceedings of 2016 IEEE Congress on Evolutionary Computation (CEC)*, pp.4642-4647, 2016.

[D29] S. Bandyopadhyay, S. Saha, U. Maulik, and K. Deb, "A simulated annealing-based multiobjective optimization algorithm: AMOSA," *IEEE Trans. Evol. Comput.*, vol.12, pp.269-283, 2008.

[D30] J. Yang, S. Yang, and P. Ni, "A vector Tabu search algorithm with enhanced searching ability for pareto solutions and its application to multi-objective optimizations," *IEEE Trans. Magn.*, vol.52, Art. No. 7001204, 2016.

[D31] S. Yang., and et. al., "An improved tabu-based vector optimal algorithm for design optimizations of electromagnetic devices." *IEEE Transactions on Magnetics*, vol.40, pp.1140-1143, 2004.

Chapter 5 Evolutionary Algorithms for Multi-Material Topology Optimization and Radial Function based Optimization

Topology optimization (TO) of a device involves the determination of the distribution of multiple materials to yield the best device performance. TO can create a novel topology that might not exist in the history of a product in industry. Consequently, TO together with the computationally expensive finite element method (FEM) for performance analysis has become the new paradigm to provide a quantitative design method for modern devices in almost all engineering disciplines [E1]. As discussed in chapter 2, a large number of algorithms are developed for topology optimization in various disciplines. However, these algorithms mainly tackle problems with only two materials, or relatively simple geometries. In electrical engineering, the design and optimization of devices involve complex geometries that might be highly irregularly occupied by more than two types of materials, and hence requires specially designed topology optimization algorithms. In this chapter, TO algorithms dealing with multi-material optimizations and complex geometry optimizations are developed.

5.1 A Multiscale Topology Optimization Methodology Based on Sequential Element Rejection–Admission and Boundary Element Evolvement

5.1.1 Sequential Element Rejection and Admission Method

The Evolutionary Structural Optimization (ESO) method is currently one of the most popular TO techniques due to its high efficiency, simplicity in implementation and easiness in integration with commercial FEM packages [E2]. In the ESO, the

design domain is discretized into small elements and the elements with the smallest sensitivities will be sequentially removed from the design model until an optimum is reached. As each element has its own design parameter, one major issue in the ESO is a large number of design parameters, and hence a finite but extremely excessive number of possible designs. The requirement of the gradient information to update the topology further makes this method numerically overwhelming. Also, the sole and complete removal of solid elements could result in some theoretical difficulties [E3]. Although a more efficient bi-directional scheme (BESO), allowing both material addition (admission) and removal (rejection), has then been developed, the ESO/BESO still faces the numerically overwhelming issue, checkerboard problems, and may also converge to entirely non-optimal solutions [E3].

To solve the aforementioned bottleneck problems in BESO, a hybridized Multiscale TO (MTO) methodology based on Sequential Element Rejection and Admission (SERA), a variant of BESO; and the Boundary Element Evolvement (BEE) algorithm is proposed in this chapter. The proposed MTO methodology utilizes the sensitivities of only the boundary elements calculated using finite difference method in the iterative process in order to reduce the computational time. Moreover, the proposed multi-level discretization scheme also reduces the computational burden without any compromise on the accuracy and the quality of the obtained topology. To avoid being trapped into a local optimal point, the topological derivative method is employed to generate topology variations.

5.1.2 Sequential Element Rejection and Admission in Multi-material Optimizations

The SERA method using the element sensitivity is a powerful method for structure topology optimizations [E4]. The sensitivity of an element is defined as the sensitivity of the objective function to the material property of the element. It can be derived analytically through the adjoint variable method when the system matrix is available, or numerically via various numerical derivative calculation methods (the directional derivatives, Gateaux derivatives or Frechet derivatives) [E5]. In each

SERA iteration, the sensitivity of every element is calculated and sorted. The solid elements with the lowest sensitivity are switched to a void, and the void elements with the highest sensitivity are switched to solid, and a new topology is then generated. This process is repeated until the optimum is reached. The criteria for the element removal and admission in the kth iteration, respectively, are:

$$\begin{aligned} &S_{e,void}^{k} > S_{\max,void}^{k} \rightarrow element\ admission \\ &S_{e,solid}^{k} < S_{\max,solid}^{k} \rightarrow element\ removal \end{aligned} \tag{5.1}$$

The admission ratio, C_{ar}^{k}, and the rejection ratio, C_{rr}^{k}, are the two predefined parameters that are updated in each iteration. The larger the value is, the faster the algorithm converges; but the less accurate the final results will be and *vice versa*. To balance the quality and convergence requirements, these two parameters are proposed to be adaptively updated via a penalty factor, ρ, by using:

$$\begin{aligned} C_{ar}^{k} &= C_{ar}^{k-1} \cdot \rho^{k} \\ C_{rr}^{k} &= C_{rr}^{k-1} \cdot \rho^{k} \end{aligned} \tag{5.2}$$

The major difference between the SERA method and the conventional BESO is in the sensitivity computation of the void elements. In a BESO method, the sensitivity of a void element is extrapolated from the sensitivity of its neighboring solid elements, while in SERA method it is directly calculated using FEM. This feature makes the SERA method more accurate when compared with its original counterpart [E6].

Applying SERA method to a multi-material optimization is similar to that of a binary material optimization. For *N* types of materials, firstly the materials are sorted based on the design properties, $\rho_1, \rho_2, \rho_3, ..., \rho_N$, and for each pair of two consecutive types of materials, the sensitivities of the elements are then derived; and based on this information, a similar admission and removal processes are performed and repeated $(N-1)$ times [E7].

5.1.3 Boundary Element Evolvement

The proposed BEE procedure is inspired from the level set (LS) method [E8]. The evolution of the topology boundary in a LS method is determined by the normal

component of the boundary speed V, calculated using the sensitivity information. In this method, a LS function, φ, is used as an implicit description of the material/void boundary; and it is positive in the material domain, zero at the boundary and negative in the void region. As discussed in chapter 2, the corresponding LS function is determined from the following first-order Hamilton–Jacobi equation [E2]:

$$\frac{\partial \varphi}{\partial t} + V \cdot |\nabla \varphi| = 0 \tag{5.3}$$

Using the idea of an LS method, the proposed boundary element evolvement considers only the boundary elements and uses their sensitivity as an indication of the direction of the movement. To identify the boundary elements, a level-set matrix is introduced. Because of the existence of an admission process, the boundaries of both the solid elements and the void elements are evolved synchronously, two level-set matrices are constructed, one for the admission and one for the removal.

One significant drawback of SERA method is its inability to generate new holes in the solid area, and hence the resultant topology obtained from conventional SERA method highly relies on the initial guess. To overcome this shortcoming, the topological derivative method [9] is integrated in the proposed BEE method. The topological derivative of a structure topology is defined as that of the objective to a new infinitesimal hole generated at position x in a solid domain [E2]

$$\tau_{\omega}(f(x)) = \frac{\lim_{\mu \to 0}\left[f(\omega \setminus B_{\mu}(x)) - f(\omega) \right]}{\left| B_{\mu}(x) \right|} \tag{5.4}$$

where μ is the radius of the hole, ω is the solid domain in the topology, $B_{\mu}(x)$ is the infinitesimal hole generated at position x. Moreover, the topological derivative is computed using a finite difference method. To integrate the topology derivative in the proposed method, a new void will be added into the solid area when no topological variation in certain portion occurs for many iterations. The updated topology with possible new holes will then be obtained based on the topological derivatives.

5.1.4 Multiscale Optimization Procedures

To reduce the overwhelmingly computational burden of a TO, it is proposed to divide the optimal procedures of the proposed algorithm into different scales, as shown

in Figure 5.1. To start with, a seed mesh is first generated, and all nodes and coordinates will be fixed in the whole optimization process. At the early stage of the optimization, only a small portion of the whole set of nodes will be activated to form an initial coarse mesh, and thus the number of elements inside the design domain is small, giving rise to a fewer design parameters problem with a fast convergence rate. As the optimization procedures progress, more accurate results and finer topologies are demanded; and the nodes in the initial mesh will gradually be activated to find a high-performance topology. More specially, when the objective does not improve for a given number of consecutive iterations, the resolution of the current mesh in the region in question will be doubled in each direction for the next cycle of iterations. From these iterative procedures, it is observed that the proposed multiscale optimization procedure would converge slowly. However, since the proposed procedure utilizes the sensitives of only the boundary elements which are obtained in the previous iterative step, the overall convergence speed is still faster than that of a non-adaptive meshing with considerable resolutions.

(i) (ii) (iii)

Fig. 5.1. Examples of the (i) initial mesh, (ii) intermediate mesh, (iii) final mesh.

5.1.5 The Proposed Multiscale SERA-BEE Methodology

The iterative procedures of the proposed multiscale SERA-BEE methodology are schematically depicted in Figure 5.2. In the initialization phase, the admission and rejection ratios, the decision criteria, the stop criterion and the initial mesh and the initial topology are defined. The initial mesh size determines the resolution of the final resultant topology and hence has to be set to be small enough. Since the topology derivative approach is used to add new holes during the iterative procedures to reduce the dependency of the finally optimized topology to the initial guess, a regular pattern is used as the starting topology for the convenience of comparison between various algorithms. The stop criterion is based on the variations in the objective values, as well

as the adaptive admission and rejection ratios in the consecutive iterations. When these values are small enough, the algorithm will be terminated.

Three matrices are used to mathematically describe the topology, namely the topology matrix that describes the material distribution in the design domain, the sensitivity matrix, and the level-set matrix that is used to trace the boundary and generate topological derivations. At the beginning of each iteration, the boundary elements are identified using the level-set matrix, and the sensitivity of each element is computed via FEM and is used to indicate the admission and removal of the boundary elements. The incremental unit for each admission and removal is one element. At the end of each iterative cycle, the level-set matrix is accordingly updated from the currently optimized topology for the next iteration. To remove the checkboard pattern and further eliminate the mesh dependence problem, the sensitivity of an element is filtered using a Gaussian filter with a standard deviation of unity：

$$S_f^k = conv(S_e^k, G_{\sigma=1}) \tag{5.5}$$

where S_e^k is the sensitivity matrix of the elements in the kth iteration, $conv$ represents the convolution process, and $G_{\sigma=1}$ is the two-dimensional (2-D) Gaussian matrix with a unity standard deviation. The filter is a second order one, meaning that only the 24 nearest elements in the neighborhood would be considered for the sensitivity average, resulting in a smoother sensitivity distribution when compared to that from the 1st order filter. The level-set matrix contains the distance information of a solid element to the nearest boundary, consider a point in the design space, χ, and with the closest boundary point $x_{boundary}$, the element in the level-set matrix representing this specific point can be calculated as:

$$\varphi_e = \begin{cases} \left\| x - x_{boundary} \right\|, & x \in \Omega \\ 0, & x \in \partial\Omega \\ -N, & x \in void \end{cases} \tag{5.6}$$

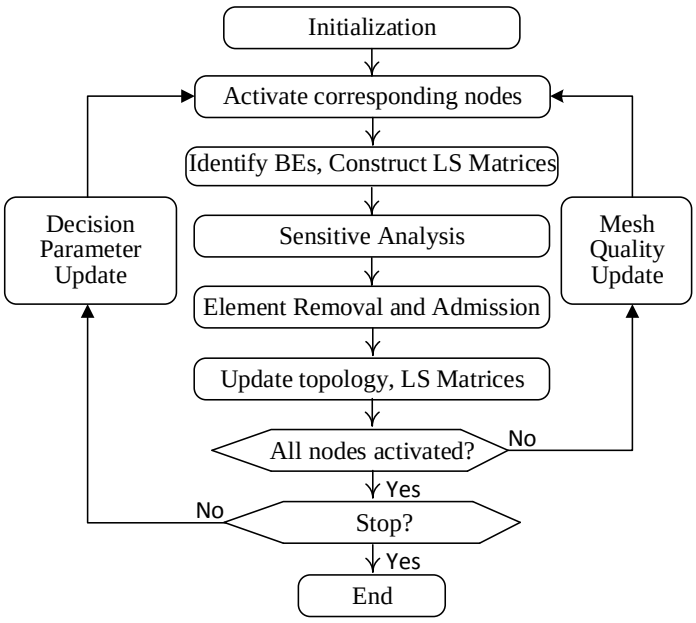

Fig. 5.2. The block diagram of the proposed methodology.

To implement the topological derivative method to avoid local optima, the proposed methodology will generate new holes in regions where the elements have the highest level-set matrix values. A large distance between such an element and the boundary indicates that the position it occupies is within the central portion of the solid structure and has remained unchanged for a number of iterations. Consequently, generating new wholes at these positions may lead to an improvement in the objective value, and hence a lower chance of the methodology converging prematurely. However, generating new holes too often will certainly increase the boundary elements number, increase the computation cost, and lower the algorithm speed. To alleviate these detrimental factors on the computational efficiency, the topological derivative approach is used as a mutation operation as a mutation operator works in an evolutionary algorithm in view of its being activated with a relative smaller probability in the proposed algorithm.

5.2 Application of the Proposed Multiscale Topology Optimization Methodology

To validate the feasibility of the proposed algorithm and examine its performance, two 2-D case studies are solved. The first one is a binary-material TO of a magnetic

actuator, and the second one is a multi-material TO of a Printed-Circuit-Board (PCB) substrate. The numerical experiments results are compared to performance of other algorithms to show their appropriateness in TO of electromagnetic problems. In both cases the objective functions are evaluated using ANSYS APDL FEM software.

5.2.1 Optimization of Iron/Air in a Magnetic Actuator

The proposed methodology is firstly used to optimize the topology of a magnetic actuator [E10], as schematically depicted in Figure 5.3. The component to be optimized is the right teeth of the *C*-core, which is discretized into $30\times9=270$ 2nd order quadrilateral elements. The current density of the coil is set to be 2 A/mm^2. The initial rejection and admission ratios are set to be 2% with a penalty factor of 0.9. The coarse mesh size is $3mm\times3mm$ and the fine mesh size is $1mm\times1mm$. Two materials, air of permeability μ_0, and linear iron of relative permeability 1000 are used. The objective function is to maximize the absolute value of the *x* directional force acting on the armature located at the right side.

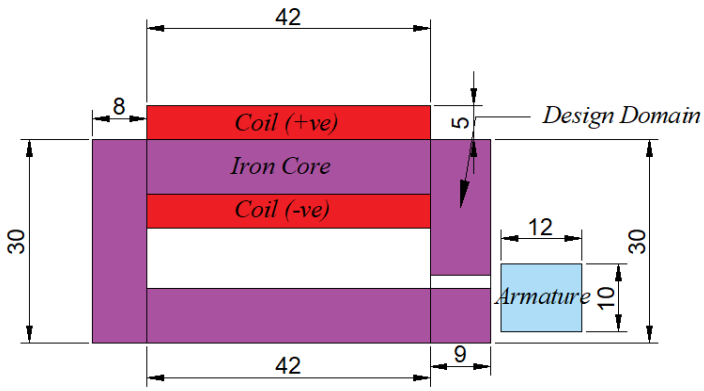

Fig. 5.3. Schematic diagram of the prototype actuator.

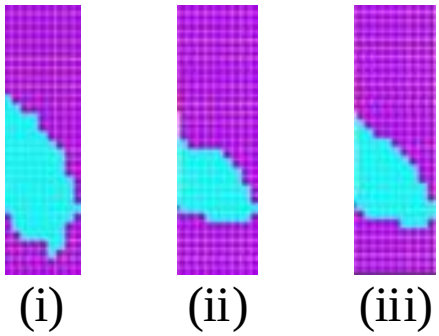

Fig. 5.4. Resultant topology of (i) ON/OFF; (ii) BESO; (iii) Proposed.

For performance comparison, three different algorithms, the ON/OFF, the BESO, and the proposed methods are used to solve this case study; and the finally optimized topologies are given in Fig. 5.4. It is obvious that the resultant topology of the proposed methodology is smoother than those of the ON/OFF and current BESO methods; and the optimized objective value for the proposed method, which is 54.97 N/m, is comparable to that of the BESO, which is 54.31 N/m; and is better than that of the conventional ON/OFF hard kill method, which is 53.12 N/m. The average time of 10 independent runs for finding an optimum by the proposed algorithm is about 5300 s, which is 40% faster than 8900 s for the BESO; and more than 60% faster than 12000s for the ON/OFF method, as detailed in Table 5.1.

Table 5.1 Performance comparison of three algorithms

	ON/OFF	BESO	Proposed
Objective function (N/m)	53.12	54.31	54.97
Average CPU time (s)	12000	8900	5300
No. of iterations	20	15	14

5.2.2 Optimization of a PCB Substrate with Three Materials

To demonstrate the feasibility of the proposed methodology for multi-material optimizations, it is then used to optimize the three-material distributions in a PCB substrate. The problem is formulated as [E11-E12]:

$$\begin{aligned} &\max\ f = \text{mean}(\phi_{q,e}) \quad e \in \Omega \\ &\text{s.t.}\ \ \sum \rho_e V_e \le 0.7\text{Mass}_{\text{initial}} \end{aligned} \tag{5.7}$$

where $\phi_{q,e}$ is the heat flux of each solid element and the objective of the optimization is to obtain a structure with evenly distributed heat flux on each solid element so that the PCB substrate is able to sustain high thermal stress [E11]. The properties of the three materials are tabulated in Table 5.2. The PCB is discretized into a total of 66×106 second order quadrilateral element meshes, and the six rows and columns at four ends of the substrate are fixed to material I and set at $0℃$ boundary condition. Four identical heat sources with a power of 0.2 W/mm^2 are applied symmetrically to the PCB substrate. The initial rejection and admission ratios are set to be 1% with a

penalty factor of 0.99. The initial topology of the PCB substrate is full of solids of material I and the mass constraint is set to be 70% of the initial mass [E12].

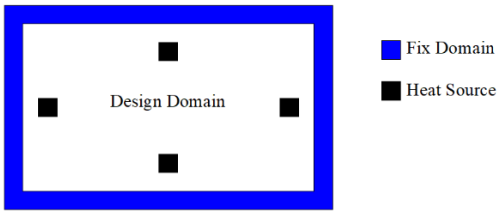

Fig. 5.5. The PCB substrate design problem.

Generally, the TO of multi-material design problems using SERA is equivalent to conducting $(N-1)$ times of binary material optimizations, and the two admission or rejection ratios, controlling the interaction between material I and material II, or material II with air; are employed to control the optimization direction synchronously. Figure 5.6 gives the optimized topologies of the proposed methodology and other algorithms as reported in [E12].

Table 5.2 Material properties of the three types of materials

	Type I	Type II	Type III
Young's Modulus (GPa)	210	210	210
Density (Kg/mm^3)	2320	1600	1100
Thermal conductivity (W/mmK)	0.045	0.0225	0.0003
Colour	Black	Grey	White

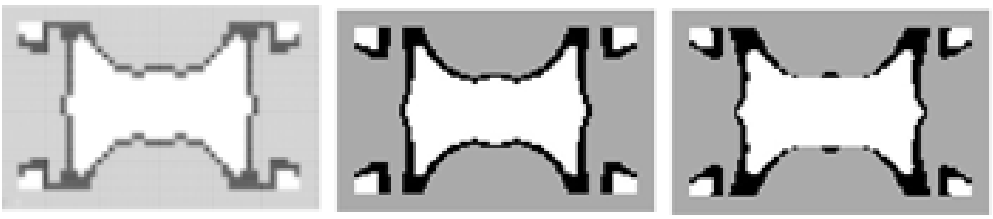

(i) (ii) (iii)

Fig. 5.6. Optimized Topology of (i) the original in [E11]; (ii) the proposed method with (iii) without, an adaptive admission/rejection ratio.

From Figure. 5.6 it can be clearly concluded that, although the optimized topology of the proposed algorithm is identical to those of the other two algorithms, the boundary of the former is smoother than those of the latter twos due to a higher resolution from 53×33 to 106×66. Moreover, since the proposed algorithm uses an adaptive parameter updating strategy, its convergent speed is faster than that of its conventional counterparts using the constant ones. More specially, the number of iterations required to find Figure 5.6 (ii) using the proposed methodology is 137, and 420 for Figure 5.6(iii) where only non-adaptive admission/rejection ratios are used, other things being equal. Consequently, a more than 50 % faster convergent speed is observed for the proposed adaptive admission/rejection ratio updating scheme.

Table 5.3 Performance comparison of the proposed method

	Proposed	BESO
Number of iterations	137	420
Number of mesh elements	6995	1749
Number of repetitions	10	10

5.3 A Modified Shuffled Frog Leaping Algorithm for Topology Optimizations of Electromagnet Devices

5.3.1 Shuffled Frog Leaping Algorithm

As explained previously, topology optimization is the process of determining the material distribution for devices that could yield the best performance under given constraints. TO has shown great potential in the device design and optimization process and has become a new paradigm to provide a quantitative design method for modern industries in multiple disciplines [E13]. To enhance the speed of the TO process, numerous modern mathematical algorithms have been proposed and developed, and proved to be efficient in solving complicated three-dimensional (3-D) problems [E14]. Based on the optimization searching methodologies, these methods can be categorized as the deterministic method, where the searching process is based on the gradient information, such as the Newton method; and the meta-heuristic

method, where the searching process is guided by the information gathered from random or designed population, such as the evolutionary algorithms, or those from the related disciplines such as the bidirectional evolution structural optimization algorithm (BESO) [E15-E16].

Evolutionary algorithms (EA) imitate the evolution process of population existing in the natural environment. The population could be species, flock of birds or fishes, or any other possible group of candidates that could share experience and intelligence. EAs have been adopted widely in optimizing the shape and size of electromagnetic devices because of their simplicity in applications and high global searching ability [E17]. For instance, genetic algorithms (GA) are applied together with the finite element method (FEM) in the design and parameter optimization of interior permanent-magnet motors in various studies [E18-E20], and have proved to be feasible and efficient in solving these problems. However, in the case of TO, due to the large degrees of freedom in the design space, the inherited complexity of the problem is much higher than those of the shape and size optimization problems, and hence the searching speed of the algorithm plays an important role affecting the optimization time. One issue with respect to the conventional EAs is the passage of genes is limited to the offspring, because the generation of children is based on the crossover of *elite* parents only, and hence the searching direction is limited, resulting in a relatively poor searching diversity and searching efficiency. To overcome this issue, local search steps are often added to the *elite* population or to the best candidate [E21]. In the local search step, the neighborhood of the feasible candidate is searched by adding randomly generated vectors to the candidate and with their performances investigated accordingly. Another type of meta-heuristic algorithms is the memetic algorithm, where the memetic evolution is used as the searching mechanism. The entire population is divided into subgroups called memeplex, and within each memeplex, the searching direction, which can also be regarded as the memes in the memeplex, is determined by the positions of the best solutions. Each individual in the memeplex learns from both the local best solution in the memeplex and from the global best solution in the entire population. Because the memes in the memetic algorithm can spread freely through the population, this type of algorithms is associated with a stronger searching efficiency with a smaller number of objective function evaluations when solving problems with higher degrees of freedom and larger number of control variables [E22-24].

The Shuffled Frog-Leaping Algorithm (SFLA), formulated in 2006, has been successfully applied to scheduling problems, network design problems, and parameter estimation of electromagnetic devices [E25-E27], and has shown great potential in handling high dimension problems. The SFLA can be viewed as an extension of the classical particle-swarm optimization (PSO) algorithm, with certain newly added features such as the usage of memeplex. In here the SFLA together with the Gaussian radial basis function (RBF) modelling method is employed to optimize the two-dimensional (2-D) design of the rotor in a conventional Interior Permanent-magnet Motor (IPM). To further improve the efficiency of the SFLA and avoid the problem of finding false optima, a local search step is added to the algorithm to add randomness to the optimization process.

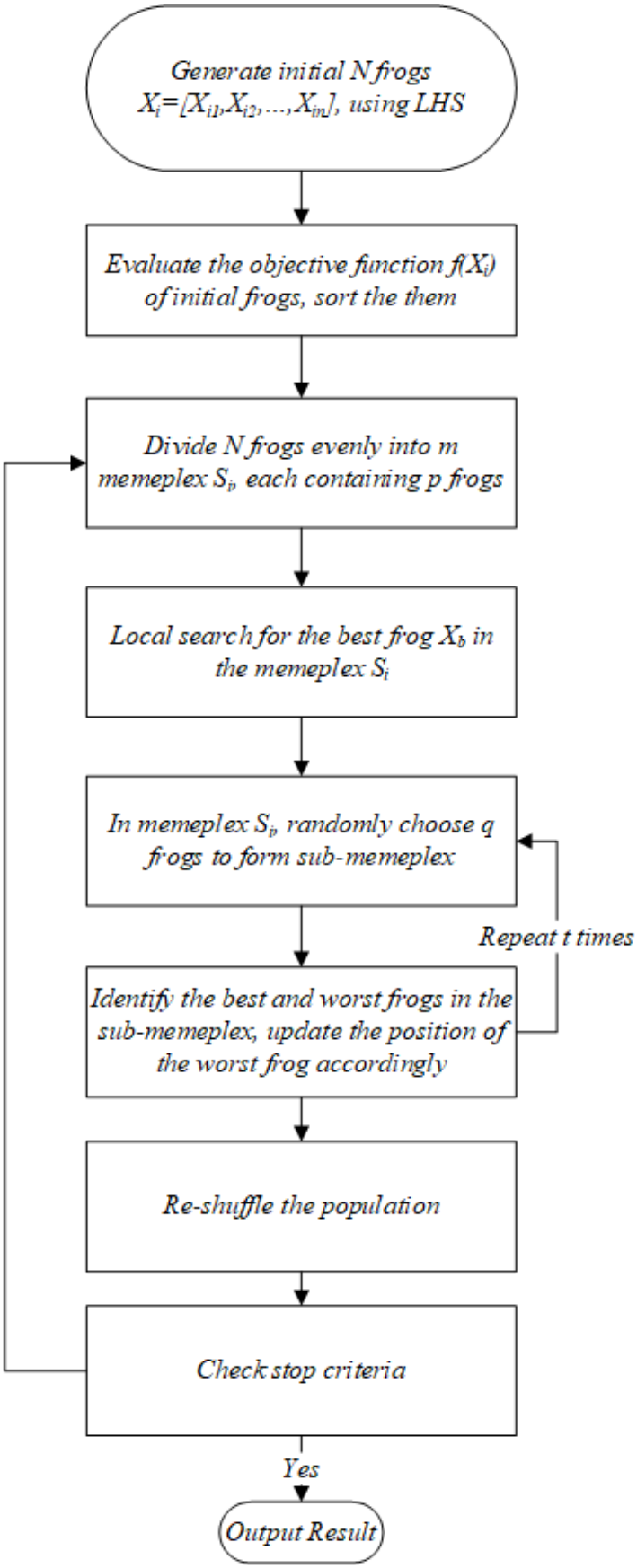

Fig. 5.7. Flowchart of the Shuffled Frog-Leaping algorithm.

The design space of the optimization problem is discretized into small elements that will be filled with either iron or air, and Gaussian RBFs are used to calculate the topology function of each element to create the topology. The Finite Element Method (FEM) is employed to evaluate the objective function of the TO problem. To showcase the prominent efficiency of the SFLA in the electromagnetic TO problems, three algorithms are employed for the same IPM TO problem, which are the Local-search GA (LS-GA), conventional SFLA and the proposed SFLA. Both the speed and accuracy of the algorithms are compared, and the results indicate that the proposed SFLA is more appropriate in the design and optimization of complicated electromagnetic devices such as IPMs.

Similar to the other algorithms in the memetic family, the evolution process in SFLA also contains both local exploitation mechanism and global exploration mechanism. An initial population is randomly generated, evaluated, and sorted. Based on the objective function values, the individuals in the initial population are partitioned into different subgroups of equal size named memeplexes. Within each memeplex, individuals will evolve via moving towards either the local best in the memeplex, or the global best. After certain iterations of local evolvement, the entire population will be re-shuffled for the spreading of the memes. These steps will be repeated until the stopping criterion are met [E28]. In the ordinary SFLA algorithm, within each iteration the best candidate, or frog in the case of SFLA, of each memeplex will not update its position. As each candidate will always remain at the same position, especially for the best frog in the entire population, it is easy for the algorithm to be trapped in some local optima found at the early stage of the optimization process and hence end prematurely to fault optima. To avoid this problem, a local search process for the best frog in each memeplex is added to the algorithm to help the algorithm to escape from false best solutions.

The flowchart of the proposed SFLA is given in Figure 5.7. For an optimization problem with *n* control parameters, each frog in the algorithm is an *n* dimension vector, $X_i = [x_{i,1}, x_{i,2}, x_{i,3}, ...x_{i,n}]$. At the beginning of the optimization, a total of *N* frogs are generated using the Latin-Hypercube Sampling method to ensure the entire design space can be well explored. Based on the objective value of each individual frog, the initial population is then sorted, and evenly partitioned into *m* memeplexes $S_1, S_2, S_3, ..., S_m$, with each memeplex containing *p* frogs, where $N = m \times p$. For instance,

if $m = p = 3$, then S_1 contains X_1, X_4, X_7, S_2 contains X_2, X_5, X_8, and S_3 contains X_3, X_6, X_9, given all X_i have been sorted. The number of frogs in each memeplex is set to be $n+1$ based on the Nelder-Mead method [E29]. Followed by the partition process, a local search is conducted in memeplexes. A random vector with $\frac{1}{10}$ th upper and lower bound is added firstly to the best frog in the memeplex, $X_{b,k}$:

$$X'_{b,k} = X_{b,k} + \frac{1}{10}\left[\text{rand}(lb, ub), ..., \text{rand}(lb, ub)\right] \tag{5.8}$$

The objective function value of the new frog is evaluated. If it is better than the original frog, then $X_{b,k}$ is replaced by $X'_{b,k}$. After the update of the best frog in the kth memeplex S_k, a small portion of frogs are selected to form a sub-memeplex. The selection probability of each frog in the memeplex is derived based on their objective value ranking in the memeplex using the triangular probability function [E23]:

$$P_{i,k} = \frac{2(p+1-i)}{p(p+1)}, \qquad i = 1, 2, 3, ..., p \tag{5.9}$$

where $P_{i,k}$ is the frog selection probability in the kth memeplex, and i is the ranking of the frog. Inside the sub-memeplex, the frog with the best objective value, $X_{b,k}$, and the frog with the worst objective value, $X_{w,k}$, are identified. To imitate the process of sharing information, the worst frog will learn from both the best frog in the sub-memeplex and from the global best in the entire population, which is a process similar to the PSO algorithm [E25]. Mathematically, the position of the worst frog will be updated by:

$$\begin{aligned} v &= S \times \left[w \times (X_{b.k} - X_{w,k}) + (1-w) \times (X_{b,\text{overall}} - X_{w,k}) \right] \\ X'_{w,k} &= X_{w,k} + v \end{aligned} \tag{5.10}$$

where S is the predefined step size, and w is the random weight between [0,1]. If the new position $X'_{w,k}$ is within the design space, its objective value is evaluated. If the result is not better than the original objective value of the same frog, the position of the worst frog will be updated again using the position of the global best frog, $X_{b,\text{overall}}$, instead of the position of the best frog in the sub-memeplex:

$$\begin{aligned} v &= S \times w \times (X_{b,\text{overall}} - X_{w,k}) \\ X'_{w,k} &= X_{w,k} + v \end{aligned} \tag{5.11}$$

If the new position $X'_{w,k}$ is within the design space, again its objective value is evaluated. If in both cases there is no improvement in the objective value, the worst frog is mutated according to:

$$X'_{w,k} = [\text{rand}(lb,ub),...,\text{rand}(lb,ub)] \tag{5.12}$$

The local search process will repeat for *t* times, and then the entire population will be shuffled and moved to the next iteration. As extra numbers of function evaluations are required, the optimization time for each iteration is longer than that in conventional SFLA. These steps will repeat until the stop criteria is met.

5.3.2 Normalized Gaussian Radial Basis Function Formulation

In the TO process for the electromagnetic devices, a commonly practiced method when constructing the topology of the model is to divide the design space into a number of small elements, and assign material to each element based on the value of its topology function controlled by the design variables of the problem. Because the position vectors of the frogs can be any arbitrary numbers in the design space, the design variables in SFLA should be continuous. Therefore, the normalized Gaussian Radial Basis Function (RBF) modelling method [E28] is employed in this study to reconstruct the topology of the electromagnetic devices. In the normalized RBF method, the value of topology function at location *x* in the design space can be described as:

$$s(x) = \frac{\sum_{i=1}^{M} w_i \times \phi(\|x - x_i\|)}{\sum_{i=1}^{M} \phi(\|x - x_i\|)}, \qquad w_i \in [0,1] \tag{5.13}$$

where *M* is the total number of RBFs in the model, $\|\bullet\|$ is the multidimensional norm, w_i is the weighting of each RBFs and is the design parameter, and the function ϕ is the predefined radial function. The value of $s(x)$ determines the material type of the element x_e located at the position x, which is either iron or air in this chapter:

$$\begin{aligned} s(x) > 0.5, \quad \text{Mat}(x_e) = \text{Iron} \\ s(x) < 0.5, \quad \text{Mat}(x_e) = \text{Air} \end{aligned} \tag{5.14}$$

where $Mat(x_e)$ defines the material type of element x_e. Because only the weight of each RBF is controlled during the optimization process, the number of control parameters as well as the complexity of the problem can be significantly reduced.

Moreover, the usage of RBFs helps to transfer the discrete topology matrix into function of continuous variables. The radial function used in here is the normalized Gaussian function with zero mean. For an RBF centered at x_e, its value at any point x in the design space will be:

$$\phi(x) = \frac{1}{2\pi\sigma} e^{-\frac{1}{2}\left(\frac{\|x-x_e\|}{\sigma}\right)^2} \tag{5.15}$$

The radius of the RBFS is determined by its variance σ. To ensure that the entire design domain can be reconstructed, the RBFs are set to be evenly distributed, and the radii of them are larger than the distance between any two consecutive RBFs. In the proposed TO process, both the position and the radius of RBFs are predefined in order to reduce the number of control variables with a less complicate reproduction process. The design parameter, which is the weight of each RBF, is set to be positive to avoid any possible conflict in the topology definition and is bounded between $[0,1]$ to reduce the design space. After the calculation of the topology function, the material type of the element is also determined and assigned in order to create a topology matrix accordingly. To further remove the checkerboard pattern in the topology, a 2-D filter is used to refine the topology matrix. The actual FEM evaluation is then conducted using the created model.

5.3.3 Problem Formulation and Numerical Application of the Proposed SFLA Method

In this section, the proposed SFLA is applied to the topology optimization of the iron part in the rotor of a benchmark Interior Permanent-magnet Motor (IPM). To reduce the time for objective value evaluation, the 2-D model of the 1/4th cross-section of the prototype machine with periodic boundary condition is used for FEM evaluation, and the stack length is set to be 120 mm. All the other parameters in the model are set to be constants. Table I lists out all the fixed parameters.

Table 5.3 PM fixed parameter values

Parameters	Value	Unit
Stator outer radius	110	mm
Stator inner radius	75	mm
Air gap length	0.45	mm
Rotor outer radius	74.55	mm
Rotor inner radius	52.5	mm
Permanent magnet length	20.4	mm
Permanent magnet width	5.5	mm
Phase current amplitude	9.69	A
Coil number of turns	30	
Motor speed	2800	rpm
Number of slots/poles	48/8	

The design space of the problem is the $\frac{1}{16}^{\text{th}}$ portion of the rotor which is then replicated with two mirror processes to re-construct the quarter model. The usage of smaller design space helps to improve the resolution of the obtained topology with the same number of elements, as well as ensuring a symmetrical rotor structure. The entire design domain is divided into 990 elements, 22 in a row and 45 in a column, with each element occupying 0.5° in width and 1 mm in length and will be filled with either iron or air. Numerical experiments are conducted to search for the best number of RBFs and Gaussian variance for the RBF modelling process. To obtain a smooth topology with relatively small number of design variables, a total of $(4\times9)=36$ RBFs are used to cover the entire design domain. Each RBF is set to be 5 elements from its neighbor RBF, in both radial direction and along the arcs, and the variance of the Gaussian function is set to 1. The control parameters, which are the weight of each RBF, are set to be bounded between $[0,1]$.

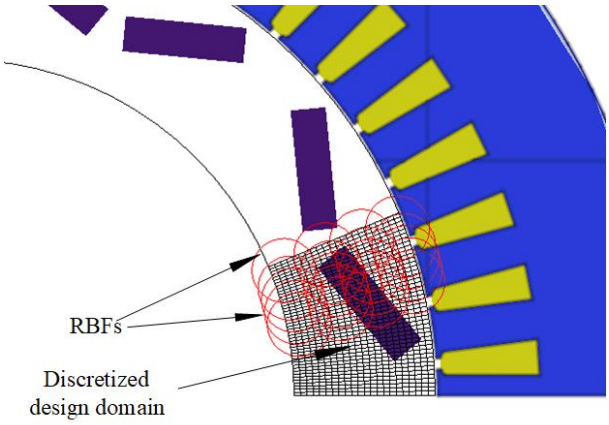

Fig. 5.8. The initial discretized design domain and RBFs used (in red).

Figure 5.8 depicts the initial design domain, and the 36 RBFs are used to construct the topology. The red circles in the design domain indicate the RBFs and their effective areas, where inside the effective area the values of RBFs are positive, and outside the effective area their values are assumed to be zero. Hence, each RBF will control only the topology of a small region in the design domain, and a large variety of topology can be generated using the RBF method. The aim of the topology optimization is to maximize the average torque and minimize the torque ripple, and hence the objective function of the TO problem is defined as the weighted sum of the normalized average torque and the torque ripple of the IPM evaluated using Ansys Maxwell, evaluated by the virtual work method employed in the software:

$$\begin{aligned} &\max f(X) = c_1 \frac{T_{avg}(X)}{T_{\text{prototype}}} - c_2 \frac{T_{\max}(X) - T_{\min}(X)}{T_{avg}(X)}, \quad X = [X_1, X_2, X_3, ..., X_{36}] \\ &s.t. \quad \text{Area}_{\text{iron}} \le \text{Area}_{\text{design}} \end{aligned} \tag{5.16}$$

where c_1 and c_2 are two predefined weight coefficients and equal to unity in this problem, $\text{Area}_{\text{iron}}$ is the area of iron part in the IPM of the design, and $\text{Area}_{\text{design}}$ is the area of the design space, which has a fixed size in the optimization problem, and hence can serve as the volume constraint of the TO problem. To ensure fair comparison, all designs are analyzed using ANSYS Maxwell FEM software.

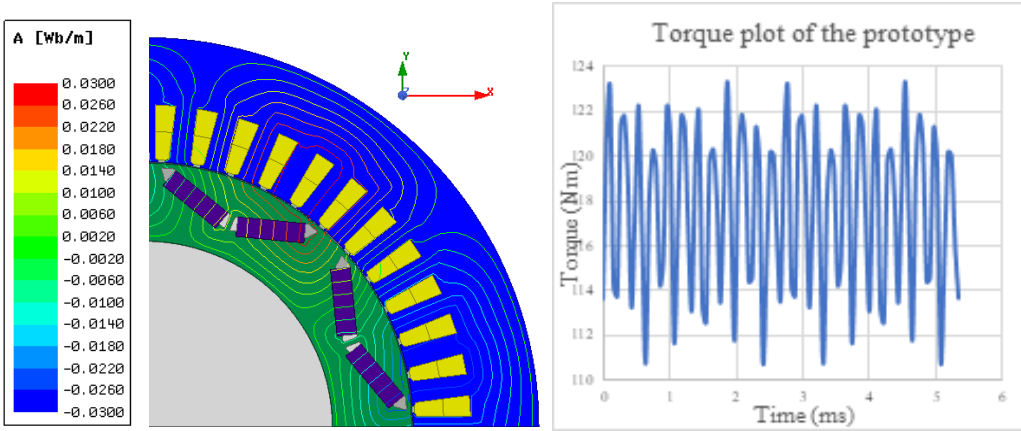

(a) (b)

Fig. 5.9. The conventional design of IPM used for comparison (a) cross-section; and (b) torque plot.

The prototype IPM design and its performance are given in Figure 5.9. The averaged torque of the prototype, $T_{\text{prototype}}$, is 117.6 Nm, and the torque ripple of the machine is 9%. The algorithm stops when the best solution stays unchanged for five consecutive iterations or the iteration number exceeds 1000. To determine the appropriate algorithm parameters including the sub-memeplex size, local search times for the worst frogs and for the best frogs in the memeplex, the SFLA is run twice, using two sets of parameters, for each single objective optimization of the prototype IPM when optimizing its averaged torque. The parameter values and the corresponding algorithm performances are listed in Table 5.6. For both cases, the size of the population, memeplex and sub-memeplex are identical. In the SFLA algorithm, the best frog local search step and the worst frog improvement step are the two core steps responsible for the exploration of the design domain. In the first run, the algorithm concentrates more on the directed search, and in each memeplex, the update of worst frog's position towards the best frog's position will be repeated thrice, while the random local search for the best frog is only conducted once. In the second run, the algorithm focuses on the random search, and hence the random local search for the best frog in each memeplex is conducted thrice, and the worst frog improvement step is only done once. The results of two runs indicate that with comparable numbers of FEM evaluations, the second run can obtain a better optimization result. This is because in the first run more computing resources are used to improve the overall objective values of the entire population, which is not necessary in the case of TO of electromagnetic devices. In the second run, the addition of randomness to the

population via the best frog in each memeplex significantly improves the algorithm's ability to escape from the local optimum, and hence the optimized result is better than that of the first run. Hence in the actual multi-objective TO problem for the IPM, the second set of parameters is chosen.

Table 5.4 Algorithm parameters used, and the results obtained for two test runs of SFLA

	First run of SFLA	**Second run of SFLA**
Population size	185	185
Memeplex size	5	5
Sub-memeplex size	3	3
Local search step size	1	2
Worst frog improvement repetition	3 times	1 time
Best frog improvement repetition	1 time	3 times
Number of FEM calls	636	901
Optimized results	106.85 Nm	134.73 Nm
No. of cycles to find the Optimum	1	6

After determining the algorithm parameters, the proposed modified SFLA is applied to the multi-objective TO problem of IPM motor formulated in the early part of this chapter. To showcase the merits of the proposed method, its performance is compared with the performance of other two EAs, namely the original SFLA and the Local-search assisted Genetic Algorithm (LS-GA). The reasons of choosing these two EAs for comparison are: 1. The conventional SFLA has been applied to other mathematical optimization problems with good performance, and the performances of SLFA in electrical engineering require more studies, and 2. The LS-GA is a well-studied hybridized EA and hence is used as a reference. Based on the famous no free lunch theorem, one cannot improve the performance of an optimization algorithm without sacrificing its performance in any other aspects [E30], and hence both the optimization time and the optimized results are compared as the indications of the algorithm efficiency and performance. The optimized topology designs and their corresponding torque plots of the three algorithms are given in Figures 5.10, 5.11 and 5.12. The details of their performances are summed up in Table 5.7. All three

algorithms are repeated three times and their performances are averaged to ensure the reliability of the results by minimizing the effects of the randomness in all three algorithms.

Table 5.5 Summary of optimization performance of all three EAs

	Conventional SFLA	**LS-GA**	**Proposed SFLA**
Average number of FEM evaluations	661 times	1800 times	905 times
Standard deviation in FEM evaluations	60	246	141
Optimized average torque	100.8 Nm	130.8 Nm	126.8 Nm
Optimized torque ripple	28.2%	20.0%	19.8%
Weighted sum objective	0.539	0.91	0.88
No. of cycles to find the Optimum	2	7	6
Weight ratio (to the entire design domain)	67.7%	60%	63.5%

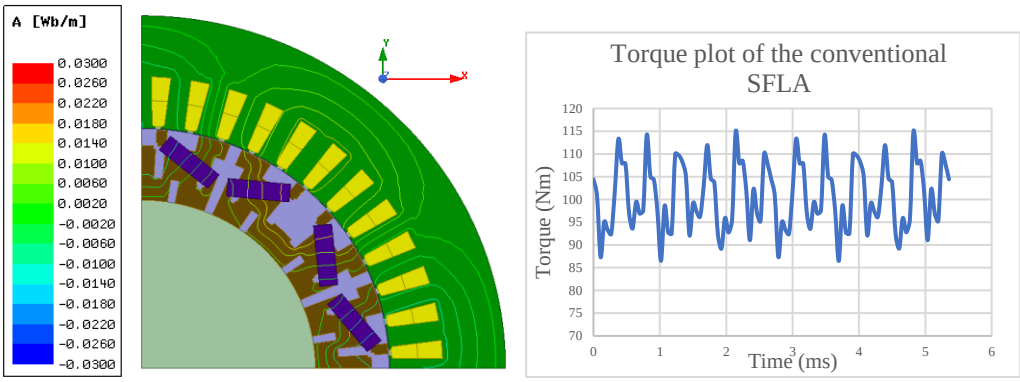

Fig. 5.10. The Optimized design of IPM obtained by the conventional SFLA (a) cross-section; and (b) torque plot.

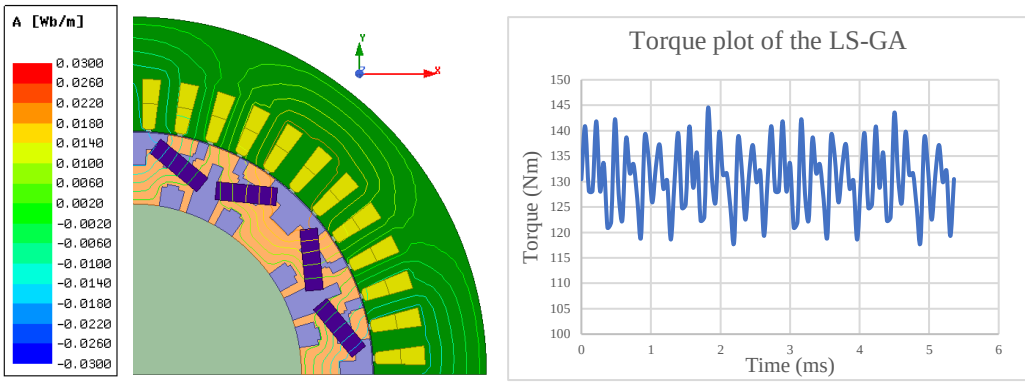

Fig. 5.11. The Optimized design of IPM obtained by the LS-GA (a) cross-section; and (b) torque plot.

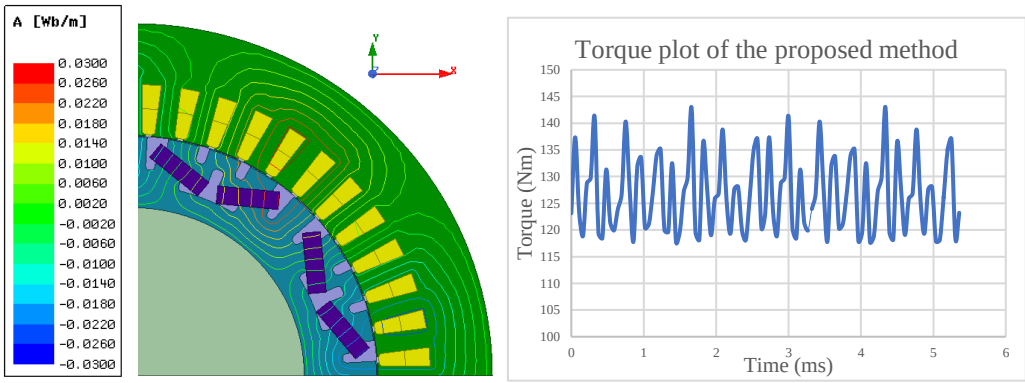

Fig. 5.12. The Optimized design of IPM obtained by the proposed algorithm (a) cross-section; and (b) torque plot.

Among all three algorithms, the conventional SFLA has the fastest optimization speed, and the overall optimization requires only 600+ FEM evaluations to locate the optimum. However, because there is a lack of an escape mechanism from local optima, the optimized result found by the SFLA has a relative low objective value, with an

averaged torque of 100.8 Nm, torque ripple of 28.2% and weighted objective value of 0.539. The population size is 185 and the number of cycles to find the optimum is two and does not go through any evolvement for the remaining optimization process, making the result of the algorithm highly dependent on the initial guess of the optimization process. On the other hand, the LS-GA algorithm has the longest optimization time, as well as the best optimization results. It can successfully locate the solution with the largest averaged torque value of 130.8 Nm, as well as the best weighted objective values of 0.91. However, the average number of FEM evaluations for LS-GA is about 1800 evaluations, which is three times of the optimization time of the conventional SFLA algorithm. The performance of the proposed algorithm falls in between the conventional SFLA algorithm and the LS-GA algorithm. The average time cost of the proposed algorithm is 950 FEM evaluations, which is 1.5 times of the conventional SFLA and almost half of the LS-GA, and the optimized result found by the proposed method is 0.88, with an averaged torque of 126.8 Nm and torque ripple of 19.8%. The tradeoff between the optimization speed and the result performance of the proposed algorithm is the most efficient among all three EAs. Compared with the LS-GA algorithm, the proposed algorithm sacrifices only a small degradation in the quality of the optimization result (96.7% objective value) in return for a shorter optimization time (50% optimization time). On the other hand, the local search step in the proposed algorithm enhances the algorithm's ability for exploration, and the number of cycles to find the optimum is 6, which is the last iteration. Because the design space is more extensively explored, the optimization time is relatively longer (1.5 times of that of the conventional SFLA), but with a much better optimization results (1.27 times the objective value of the conventional SFLA).

5.4 Summary

In this chapter, a hybridized multiscale SERA-BEE topology optimization methodology is proposed, and its performances are evaluated using two case studies. The numerical results have demonstrated that the proposed methodology outperforms both its ancestor, BESO; and an efficient topology optimization technique, the ON/OFF method, in terms of both solution quality and convergence speed. Furthermore, a modified shuffled frog-leaping algorithm that is suitable for complex

electromagnetic problem is developed as well. Compared with conventional SFLA, the proposed algorithm adds a local search step to the global best in each memeplex formed during the optimization and discards some repetitions in the worst candidate improvement process, and hence the algorithm has a better exploitation abilities with comparable time cost. To examine the performance of the proposed algorithm, it is applied to the topology optimization of an IPM prototype, and the results are then compared with the TO results of two other evolutionary algorithms, namely the conventional SFLA and the Local-search genetic algorithm. The LS-GA finds the best result with the longest optimization time, while the conventional SFLA finds the result with the least objective value using the shortest time. The optimized result found by the proposed method is 95% of the result found by LS-GA using 50% of optimization time of the latter, and hence the proposed algorithm has the most efficient tradeoff between the optimization time and the objective values, making it suitable for the optimization of an electrical machine.

5.5 Reference-Part E

[E1] S. Jung, J. Ro, and H. Jung, "A hybrid algorithm using shape and topology optimization for the design of electric machines," *IEEE Trans. Magnetics*, vol. 54, no. 3, Article no. 8102604, 2018.

[E2] S. Zargham, T. A. Ward, R. Ramli, and I. A. Badruddin, "Topology optimization: a review for structural designs under vibration problems," *Structural and Multidisciplinary Optimization*, vol. 53, no. 6, pp. 1157-1177, 2016.

[E3] M. Zhou and G. Rozvany, "On the validity of ESO type methods in topology optimization," *Struct Multidisc Optim*, vol. 21, pp. 80-83, 2001.

[E4] C. Alonso, O. Querin, and R. Ansola, "A sequential element rejection and admission (SERA) method for compliant mechanisms design," *Struct Multidisc Optim*, vol. 47, no. 6, pp. 795-807, 2012.

[E5] I. Rekanos and A. Raisanen, "Microwave imaging in the time domain of buried multiple scatterers by using an FDTD-based optimization technique," *IEEE Trans. Magn.*, vol. 39, no. 3, pp. 1381-1384, 2003

[E6] X. Li, X. Qi, X. Huang, Y. Xie, “Bi-directional evolutionary structural optimization method,” *Evolutionary Topology Optimization of Continuum Structures*, pp. 17-38, 2010.

[E7] J. Lee, S. Lee, K. Kim, and J. Lee, “Multi-material topology optimization of magnetic actuator with segmented permanent magnets,” *IEEE Trans. Magn.*, vol. 54, no. 7, pp. 1--6, 2018.

[E8] Y. Kim, J. Byun, and I. Park, “A level set method for shape optimization of electromagnetic systems,” *IEEE Trans. Magnetics*, vol. 45, no. 3, pp. 1466-1469, 2009.

[E9] P. Gangl, S. Amstutz, and U. Langer, “Topology optimization of electric motor using topological derivative for nonlinear magnetostatics,” *IEEE Trans. on Magnetics*, vol. 52, no. 3, Art No. 7201104, 2016.

[E10] J. Yoo, S. Yang, and J. S. Choi, “Optimal design of an electromagnetic coupler to maximize force to a specific direction,” *IEEE Trans. Magnetics*, vol. 44, no. 7, pp. 1737-1742, 2008.

[E11] Q. Li, G. P. Steven, O. M. Querin, and Y. Xie, “Shape and topology design for heat conduction by evolutionary structural optimization,” *International Journal of Heat and Mass Transfer*, vol. 42, no. 17, pp. 3361-3371, 1999.

[E12] M. S. Kim, S. R. Kim, S. Y. Han, and B. J. Yi, “Topology optimization of a PCB substrate considering mechanical constraints and heat conductivity,” *Journal of Mechanical Science and Technology*, vol. 21, no. 12, pp. 2041-2047, 2007.

[E13] O. Sigmund and K. Maute, “Topology optimization approaches,” *Structural and Multidisciplinary Optimization*, vol. 48, no. 6, pp. 1031-1055, 2013.

[E14] G. Rozvany, “A critical review of established methods of structural topology optimization,” *Structural and multidisciplinary optimization*, vol. 37, no. 3, pp. 217-237, 2008.

[E15] Z. Fan, and et al., “Evolutionary topology optimization of continuum structures with stress constraints,” *Struct Multidisc Optim*, vol. 59, pp. 647-658, 2019.

[E16] B. Blachowski, and et al. “Yield limited optimal topology design of elastoplastic structures,” *Struct Multidisc Optim*, vol. 61, pp.1953-1976, 2020.

[E17] B. Li, J. Li, K. Tang, and X. Yao, “Many-Objective Evolutionary Algorithms,” *ACM Computing Surveys (CSUR)*, vol. 48, no. 1, pp. 1-35, 2015.

[E18] D. Woo, I. Kim, and H. Jung, “Optimal Rotor Structure Design of Interior Permanent Magnet Synchronous Machine based on Efficient Genetic Algorithm Using Kriging Model,” *Journal of electrical engineering & technology*, vol. 7, no. 4, pp. 530-537, 2012.

[E19] S. Ho, N. Chen and W. Fu, “An Optimal Design Method for the Minimization of Cogging Torques of a Permanent Magnet Motor Using FEM and Genetic Algorithm,” *IEEE Transactions on Applied Superconductivity*, vol. 20, no. 3, pp. 861-864, 2010.

[E20] S. L. Ho, G. Xu, W. N. Fu, Q. Yang, H. Hou and W. Yan, “Optimization of Array Magnetic Coil Design for Functional Magnetic Stimulation Based on Improved Genetic Algorithm,” *IEEE Transactions on Magnetics*, vol. 45, no. 10, pp. 4849-4852, 2009.

[E21] H. Mehrdad, and et al., “Multi-objective genetic local search algorithm using Kohonen’s neural map,” *Computers & Industrial Engineering*, vol. 56, no. 4, pp. 1566-1576, 2009.

[E22] U. Boryczka and K. Szwarc, “Selected variants of a Memetic Algorithm for JSP - a comparative study,” *International Journal of Production Research*, vol. 57, no. 22, pp. 7142-7157, 2019.

[E23] F. Neri and C. Cotta, “Memetic algorithms and memetic computing optimization: A literature review,” *Swarm and evolutionary computation*, vol. 2, pp. 1-14, 2012.

[E24] B. Amiri, M. Fathian, Mohammad, and A. Maroosi, “Application of shuffled frog-leaping algorithm on clustering,” *International journal of advanced manufacturing technology*, vol. 45, no. 1–2, pp. 199-209, 2009.

[E25] M. Eusuff, K. Lansey, and F. Pasha, “Shuffled frog-leaping algorithm: a memetic meta-heuristic for discrete optimization,” *Engineering optimization*, vol. 38, no. 2, pp. 129-154, 2006.

[E26] M. Gonzalez, F. Jurado, and I. Pérez, “Shuffled frog-leaping algorithm for parameter estimation of a double-cage asynchronous machine,” *IET Electric Power Applications*, vol. 6, no. 8, pp. 484-490, 2012.

[E27] E. Elbeltagi, T. Hegazy, and D. Grierson, “Comparison among five evolutionary-based optimization algorithms,” *Advanced engineering informatics*, vol. 19, no. 1, pp. 43-53, 2005.

[E28] H. Sasaki, and H. Igarashi, “Topology Optimization Accelerated by Deep Learning.” *IEEE transactions on magnetics*, vol. 55, no. 6, Art. No. 7401305, 2019.

[E29] M. Luersen, R. Riche, and F. Guyon, “A constrained, globalized, and bounded Nelder-Mead method for engineering optimization,” *Struc. and multidisciplinary optimization*, vol. 27, no. 1-2, pp. 43-54, 2004.

[E30] Y. Ho and D. Pepyne, “Simple Explanation of the No-Free-Lunch Theorem and Its Implications,” *Journal of optimization theory and applications*, vol. 115, no. 3, pp. 549-570, 2002.

Chapter 6 Conclusion and Future Works

6.1 Conclusions

Topology optimization is the process of determining the material distribution in the design domain that can give the best device performance. Compared with the conventional parameter (seize) and shape optimizations, topology optimization has the highest degree of freedom in design, as well as the highest complexity. The development of topology optimization of electromagnetic devices thus still requires a continuous effort, as the electromagnetic inverse problems are often complicated and involves multiple types of materials, complex geometries, and complicated natures.

In hope of filling in the research gap in development of appropriate algorithms for topology optimization of electromagnetic devices, first a direct search method for robust topology optimization of electromagnetic problems is proposed. The evolutionary algorithm in the proposed method employs quantum bits or *Q*-bits instead of binary bits and is updated via an adaptive increment angle to balance the exploration and exploitation during the optimization process. The numerical experiments have proved that compared with conventional robust optimizer, the proposed algorithm can finish optimization within a shorter period of time. Followed by that a double-stage robust optimization of the *LC* ratio of metamaterial (MM) slabs employed in wireless power transmission (WPT) is presented. By using the double-stage algorithm and a multi-objective approach, the power transmission efficiency, as well as the robustness of the WPT system are synchronously optimized. The *LC* ratio that can yield a best balance between average PTE and system robustness is obtained.

When the physical model of the devices under optimization is too complex, numerical methods are often employed to simplify the objective evaluation process to reduce the optimization time, especially when multi-objective functions are involved. Hence, a Kriging model-based optimization method is developed for the optimization of hybrid MM slabs in WPT system. Compared with homogenous MM slabs, hybrid MM slabs with unidentical unit cells can create cavity at the center of the slabs, and hence can further enhance the PTE of the WPT system. The Kriging method is

employed to estimate the PTE of the WPT system for different designs of HMM slabs, which is normally evaluated using FEM method and takes more than 1 hour for one simulation. Both simulation and experiment results have shown that the HMM slab obtained by the proposed method outperform conventional MM slab, when working at the working frequency of the conventional MM slab, and the optimization is automatically done within a bearable time (few hours). Followed by the surrogate-based optimization algorithm, a vector wind driven algorithm trying to tackle multi-objective problems is proposed as well. By removing the redundant term in the updating scheme, the proposed algorithm enhances the diversity in the population of possible candidates and is much easier to be implemented. Two numerical experiments are conducted to validate the performance of the proposed algorithm.

To solve multi-material optimization problems, a multi-level sequential element removal and addition algorithm (SERA) is developed. The algorithm combines the commonly practiced SERA method with the multi-level technique to reduce the numerical complexity of the optimization process of the early stage. Moreover, similar to the level-set method, the proposed algorithm concerns only about the evolvement of the boundary, and hence the optimization time could be further reduced. The numerical experiment of bi-material optimization and tri-material optimization both have proved the efficiency of the proposed algorithm. Lastly, a radial function based shuffled frog leaping algorithm (SFLA) is developed to solve the optimization problem of the rotor in an interior permanent-magnet motor. Using a radial function-based representation of the design domain, the design parameter significantly reduced from more than 1000 to 36, and hence the optimization time is significantly reduced. Moreover, by using a multi-objective approach, the torque density and the torque ripple are optimized at the same time as well. The results obtained from the proposed algorithm do outperform the prototypical machine in terms of torque density and weightage sum of objective functions. To showcase the merit of the proposed SFLA algorithm, genetic algorithm and the ordinary SFLA have been imposed on the same problem, and the numerical results have revealed that the proposed algorithm can locate the optimal solution within a smaller number of iterations.

6.2 Future Works

Since two numerical algorithms and experiments have been conducted related to MM and WPT system, and the results indicate that MM slab can significantly enhance the transmission efficiency of WPT systems in low frequency regime, a more detailed automatic optimization could be conducted. The number of optimization parameters can be greatly increased. Other than the MM structure, the position of the MM slab, the size of the WPT coil and their corresponding related distance could all be optimized at the same time to search for the best combinations.

Based on the optimization results of the IPM motor, actual experiments could be conducted to validate the results obtain from numerical optimizations. Moreover, unlike other heuristic algorithms, such as the genetic algorithms, particle swarm optimization algorithms, SFLA is a relatively young algorithm that requires extensive researches. The effect of different algorithm parameters on the algorithm efficiency is unclear, in fact for most of the new optimization algorithms, these effects are unknown. Hence, numerical experiments could be conducted to investigate this relationship, and to further improve the efficiency of the SFLA algorithm.

Lastly, the robust algorithm, the multi-material optimization algorithm, and the multi-objective optimization algorithm could be studied deeper to test their feasibilities in more complex electromagnetic problems, for instance, the design of transformers/motors. Despite the fact these algorithms can outperform conventional optimization algorithms in certain areas, in a more complex problems they may lose their advantages and require further calibrations. Lastly, in certain optimization occasions, the simplified 2-D model is employed due to the difficulties in simulating 3-D model. Hence, surrogate-model that can represent the 3-D model could be developed.